



TECHNISCHE  
UNIVERSITÄT  
WIEN  
Vienna University of Technology

## DIPLOMA THESIS

# Tungsten and Tantalum substituted $\text{Fe}_2\text{VAI}$ systems

under the supervision of

Univ.Prof. Dipl.-Ing. Dr.techn. Ernst Bauer  
Institut für Festkörperphysik, E138  
Functional and Magnetic Materials

Technische Universität Wien  
Fakultät für Physik

by

**Christoph Schlögl**  
00926217

Wien, October 2023



# Kurzfassung / Abstract

## 1 Kurzfassung

Diese Arbeit zeigt die Untersuchungen und Ergebnisse von thermoelektrischen Effekten und Transportverhalten von  $\text{Fe}_2\text{VAI}$ , wenn V mit W und Ta durch Dotieren ersetzt wird. Die Proben wurden durch Induktionsschmelzen hergestellt und teilweise wärmebehandelt. Das Hauptaugenmerk lag auf der Löslichkeit der Dotierelemente in dieser vollständigen Heusler-Legierung. Diese wurde durch Röntgendiffraktometrie und energiedispersive Röntgenspektroskopie sicher gestellt.

## 2 Abstract

This thesis presents the research and finding of thermoelectric effects and transport behaviour of  $\text{Fe}_2\text{VAI}$  when doped with W and Ta at the V-site. The samples were synthesized by induction melting and some were annealed. The primary focus was the solubility of the dopants in this full-Heusler alloy. This was validated using X-ray diffraction and energy dispersive X-ray spectroscopy.

### 3 Variables and constants used in equations

- $A$  ... area
- $a$  ... amplitude
- $\alpha$  ... thermal diffusivity
- $\vec{B}$  ... magnetic field
- $c$  ... number of successes
- $c_p$  ... specific heat at fixed pressure
- $c_V$  ... specific heat at fixed volume
- $D$  ... density of states
- $d$  ... derivative
- $d$  ... crystal lattice parameter
- $\delta$  ... partial derivative
- $E$  ... energy
- $\vec{E}$  ... electrical field
- $e$  ... Euler's Number  $\sum_{n=0}^{\infty} \frac{1}{n!}$
- $e$  ... elementary charge  
 $1.602176634 \cdot 10^{-19} \text{C}$
- $\vec{F}$  ... force
- $f$  ... distribution function
- $G$  ... transport function
- $h$  ... Planck constant  
 $6.62607015 \cdot 10^{-34} \text{J s}$
- $\hbar$  ... reduced Planck constant  $\frac{h}{2\pi}$
- $I$  ... electric current
- $\vec{J}$  ... current density
- $k$  ... point in reciprocal space
- $\vec{k}$  ... vector to point in reciprocal space
- $k_B$  ... Boltzmann constant  
 $1.380649 \cdot 10^{-23} \text{J K}^{-1}$
- $\kappa$  ... thermal conductivity
- $L$  ... Lorenz number  $\frac{\pi^2}{3} \left(\frac{k_B}{e}\right)^2$
- $\mathfrak{L}$  ... Avogadro constant  
 $6.02214076 \cdot 10^{23} \text{mol}^{-1}$
- $l$  ... length
- $\ell$  ... mean free path
- $\lambda$  ... wavelength
- $\mathfrak{M}$  ... parallel transport channels
- $m$  ... mass
- $\mu$  ... chemical potential
- $N$  ... sample size
- $n$  ... number of particles
- $\Omega$  ... binomial coefficient
- $\omega$  ... angular frequency
- $PF$  ... power factor
- $Q$  ... heat
- $q$  ... charge
- $R$  ... electrical resistance
- $\vec{r}$  ... vector to point in space
- $\rho$  ... specific electrical resistance
- $\rho_d$  ... density
- $S$  ... Seebeck coefficient
- $\mathfrak{S}$  ... entropy
- $\sigma$  ... specific electrical conductivity
- $T$  ... temperature
- $\mathfrak{T}$  ... transport probability
- $t$  ... time
- $\theta$  ... beam angle
- $\tau$  ... relaxation time
- $U$  ... voltage
- $V$  ... volume
- $v$  ... speed
- $x$  ... point space

# Contents

<b>Kurzfassung / Abstract</b>	<b>iii</b>
1 Kurzfassung . . . . .	iii
2 Abstract . . . . .	iii
3 Variables and constants used in equations . . . . .	iv
<b>1 Introduction</b>	<b>1</b>
1.1 The thermoelectric effect in everyday life . . . . .	1
1.2 Commonly used materials . . . . .	2
1.2.1 Telluride based thermoelectric materials . . . . .	2
1.2.2 Zintl phases . . . . .	4
1.2.3 Copper selenide . . . . .	6
1.2.4 Silicon-germanium . . . . .	6
1.2.5 Oxide based thermoelectric materials . . . . .	6
1.2.6 Heusler compounds . . . . .	7
<b>2 Theory</b>	<b>9</b>
2.1 Transport phenomena . . . . .	9
2.1.1 Semi-classic model . . . . .	10
2.1.2 Boltzmann theory . . . . .	11
2.1.3 Landauer theory . . . . .	11
2.2 Electrical resistivity . . . . .	13
2.2.1 Simple model for electrical resistivity . . . . .	13
2.2.2 Electrical resistivity using the Landauer theory . . . . .	14
2.2.3 Electrical resistivity summary . . . . .	14
2.3 Thermal conductivity . . . . .	15
2.3.1 Simple model for thermal conductivity . . . . .	15
2.3.2 Thermal conductivity using the Landauer theory . . . . .	16
2.3.3 Thermal conductivity summary . . . . .	17
2.4 Seebeck coefficient . . . . .	18
2.4.1 Simple model for Seebeck coefficient . . . . .	18
2.4.2 Seebeck coefficient using the Landauer theory . . . . .	18
2.4.3 Seebeck coefficient summary . . . . .	19
2.5 Thermoelectric effect, Power factor and Figure of Merit . . . . .	19
2.6 Electronic band structure manipulation . . . . .	20
<b>3 Experimental methods</b>	<b>21</b>
3.1 Synthesis . . . . .	21
3.1.1 Sample preparation . . . . .	21
3.1.2 Melting process . . . . .	22
3.1.3 Annealing . . . . .	23
3.1.4 Cutting . . . . .	24
3.2 X-ray diffractometry . . . . .	25
3.3 High-temperature resistivity and Seebeck measurements . . . . .	26
3.4 Low-temperature electrical resistivity . . . . .	27
3.5 Low-temperature Seebeck coefficient . . . . .	28
3.6 Low-temperature thermal conductivity . . . . .	30

3.7	High-temperature thermal conductivity . . . . .	31
3.7.1	Specific heat . . . . .	31
3.7.2	Density . . . . .	32
3.7.3	Thermal diffusivity . . . . .	33
3.8	Scanning electron microscopy . . . . .	34
<b>4</b>	<b>Problem formulation and motivation</b>	<b>35</b>
4.1	Effect of Ta-W co-substitution . . . . .	35
4.2	Problem of Solubility . . . . .	36
<b>5</b>	<b>Results</b>	<b>37</b>
5.1	XRD analysis . . . . .	37
5.1.1	Lattice parameter . . . . .	38
5.2	Microstructure . . . . .	39
5.2.1	First batch . . . . .	39
5.2.2	Second batch . . . . .	41
5.3	Electrical resistivity . . . . .	47
5.4	Seebeck coefficient . . . . .	50
5.5	Thermal conductivity . . . . .	55
5.6	Power factor . . . . .	58
5.7	Figure of Merit . . . . .	59
<b>6</b>	<b>Conclusion</b>	<b>61</b>
6.1	Discussion . . . . .	61
6.2	Outlook into the future . . . . .	61

# 1 Introduction

In developed and developing countries the main type of power source used by households, industries and services is electricity. We take for granted that our appliances run when or after plugging them into the socket. With earths growing population, the demand for power will rise in the foreseeable future. Although metals are excellent conductors for electric current, we also need switches, regulators, modulators and other parts to control and use that energy. Semiconductors are at the base of almost every electronic device we use and they are also the foundation for this thesis. Thermoelectricity combines thermal and electrical energy. It can be observed in two distinct effects: One speaks of the Seebeck effect, named after its discoverer in 1821 [1], when a temperature gradient in a conductive material creates an electric field, a measurable voltage across the sample can be observed. The reverse effect -proably even more fascinating- is using electric current to generate a a temperature gradient. This we call the Peltier effect, named after the discoverer. [1]

## 1.1 The thermoelectric effect in everyday life

Peltier coolers are used to directly cool integrated circuits, photonic sensors, ranging from X-ray to infrared or laser diodes, where there is not enough space to fit heatsinks or compressors. Peltier elements might not create the highest temperature gradient. It is usually up to 30 K over a few millimetres distance, but they are thin and quiet. This means, they are tiny enough to be used in portable dehumidifiers, air conditioners or refrigerators. More specialized applications [2] range from solar cell-driven cooling to cryoconcentration cells to obtain higher concentrated orange juice. As early as 1998, a multi-stage cascade was conceived for a possible superconductor application. Since one Peltier element can only generate a limited temperature difference, a stack of five elements with the warm side attached to a 282 K water cooling system got as low as 149 K [2]. This was not enough to observe high temperature superconductivity. But with more efficient and mechanically stable materials, it would be possible to reach temperature below 130 K. Some devices use the Seebeck effect to convert waste heat from lamps or burners of commercial products into useable electrical energy. Another unique application example is the atomic battery, which converts the heat generated by fission of a nuclear isotope to generate electricity in space probes. The Seebeck effect can also be utilized in thermocouples to measure temperatures [1], especially useful in fire detection systems and in thousand others.

## 1.2 Commonly used materials

Facing the current economy and climate problems, having efficient cooling/heating devices as well as the ability to recover “lost” heat, would be a step forward into a better future. That is why we are looking for new, better and less toxic materials.

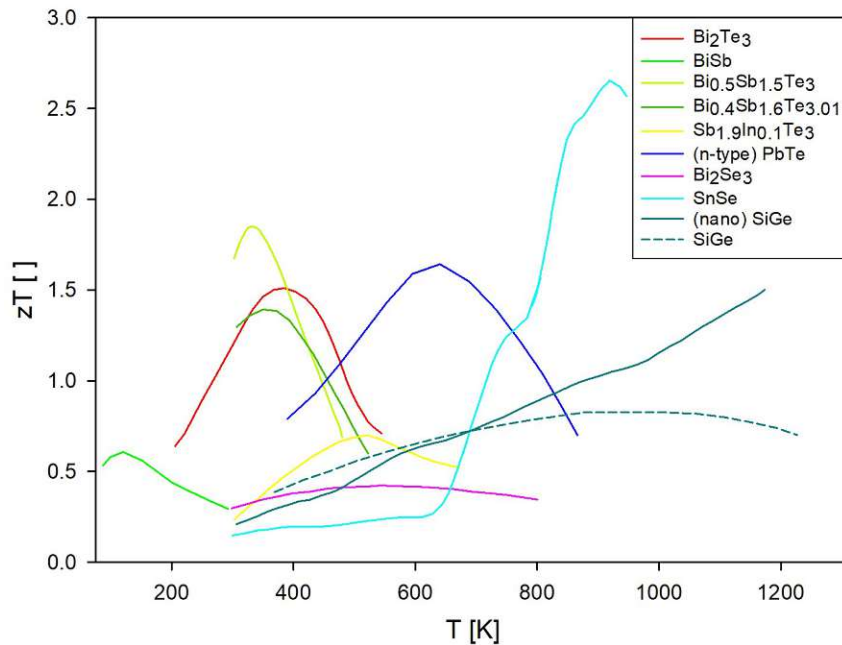


Figure 1.1: Temperature dependent figure of merit for commonly used thermoelectric materials.  $\text{Bi}_2\text{Te}_3$  (red), (n-type)  $\text{PbTe}$  (dark blue),  $\text{SiGe}$  (dashed teal) [3];  $\text{BiSb}$  (bright green), (nano)  $\text{SiGe}$  (teal) [4];  $\text{Bi}_{0.5}\text{Sb}_{1.5}\text{Te}_3$  (green-yellow),  $\text{chSnSe}$  (cyan) [5];  $\text{Bi}_{0.4}\text{Sb}_{1.6}\text{Te}_{3.01}$  (dark green),  $\text{Sb}_{1.9}\text{In}_{0.1}\text{Te}_3$  (yellow) [6];  $\text{Bi}_2\text{Se}_3$  (magenta) [7]

### 1.2.1 Telluride based thermoelectric materials

Considering the high thermoelectric performance, measured by the quantity  $zT$  (figure of merit, see section 2.5) around room temperature and ease of application, tellurides lead the charts. Especially  $\text{Bi}_2\text{Te}_3$  or  $\text{Sb}_2\text{Te}_3$  are known for their  $zT$  of up to 1.5 [5].

#### Bismuth tellurides - $\text{Bi}_2\text{Te}_3$

Bismuth is a typical Group V Chalcogenide. Interestingly enough, bismuth on its own is less toxic than other heavy metals and more abundant than gold. [8]  $\text{Bi}_2\text{Te}_3$  is a classical semiconductor with an energy gap at of the order of 160 meV and crystallizes in a rhombohedral structure with a large c-axis. Thin samples can be mechanically exfoliated due to the large c-axis, but epitaxial growth has higher yields. [9] One can grow a single crystal using the Czochralski process for even better  $zT$  values. Since  $\text{Bi}_2\text{Te}_3$  based thermoelectric materials became popular in the 1950s, the majority of thermoelectric generators have been built using those.  $\text{Bi}_2\text{Te}_3$  is a reliable base material with excellent thermoelectric properties, which can be enhanced with substitution by other elements, or specific manufacturing, like melt-spinning and spark plasma sintering, doping and even integrating conductive nanoparticles into the lattice structure via zone melting. [10] With state of the art tools, p- or n-type doped materials with similar chemical and mechanical properties can be produced. There are two major limitations: (1) The ideal temperature is in the range of 400 K to 450 K.

The efficiency and conversion from heat to electricity is governed by the Carnot factor and thereby dependent on the gradient between the heat reservoirs. Even materials with superior thermoelectric characteristics yield low conversion rates, if the temperature difference between the hot and the cold end of the samples is small. (2) Tellurium's rarity is comparable to that of platinum at around  $1 \text{ mg t}^{-1}$  in the earth's crust, about 7 times more rare than gold. It is won along with gold, copper and nickel ore. The main producer of Te is China, covering half of the mass mined a year. The other countries mining Te are Japan, Sweden, Russia, Canada, Bulgaria, Uzbekistan and the United States of America. Global consumption estimates of tellurium by the end use are thin-film solar cells, 40%; thermoelectrics, 30%; metallurgy, 15%; rubber application, 5%; and other uses, 10%. [11] The first two applications are experiencing a rapid increase due to the worldwide tendency of reducing dependence on fossil fuels. [11] Due to poor solubility in water and endogenous acids, pure tellurium and tellurium compounds are considered mildly toxic.

### Lead tellurides - PbTe

PbTe crystalizes in an face-centered cubic structure, like NaCl. [12] Its chemical bond is part ionic, part covalent. It is a semiconductor with a narrow band gap of 220 meV. [12] Thanks to intensive study, this material's mechanical properties could be enhanced greatly and the  $zT$  value of PbTe was increased from 0.8 in the year 2006 to 2.5 of p-type PbTe in 2016. [13] Even though it exhibits outstanding thermoelectric qualities, there are two major downsides. First is same as  $\text{Bi}_2\text{Te}_3$ , the problem of finite telluride. Second, and more significant: Lead and lead compounds are classified as extremely hazardous to humans, especially children, and the environment, with the suspicion of being carcinogenic. Therefore it is forbidden in the EU in many applications.

### TAGS

The abbreviation stands for  $\text{Ag}_x\text{Sb}_x\text{Ge}_{50-2x}\text{Te}_{50}$ . It is based on the chalcogen compound GeTe, only germanium is partly substituted by silver and antimony. This p-type semiconductor was developed in the 1970s. Its crystal structure is rhombohedral at room temperature and starts transitioning to a cubic rock-salt phase at about 480 K. [14] Despite this structural instability it is mechanically and chemically stable enough at an operating temperature range between 500 K and 800 K. GeTe compounds exhibit a complex fishbone like domain structure at a 100 nm scale. This increases phonon scattering and therefore decrease thermal conductivity. (section 2.3) Materials with the structure  $(\text{GeTe})_x(\text{AgSbTe}_2)_{100-x}$  are commonly referred as TAGS-x. Their composition is usually in the range of  $75 < x < 90$ . The power factor  $PF$  (section 2.5) is similar to GeTe, while thermal conductivity is greatly decreased. TAGS-80 has the higher  $zT$  values up to 1.75 at 800 K, but TAGS-85 has stronger mechanical stability with a  $zT$  of 1.4. Doping TAGS-85 with Ce and Dy can increase the  $zT$  value to 1.6. [15, 16]

### 1.2.2 Zintl phases

Zintl phases are ideal candidates for concepts like electron-crystals and phonon-glasses. Ideal thermoelectric materials should behave like an electron-crystal, a semiconductor with a high charge carrier mobility, while also behaving like phonon-glass, low thermal conductivity by scattering phonons. Incorporating foreign elements into the crystal structure to impede phonon transport, while not hindering electron transport are preferred. A Zintl phase is an intermetallic compound, consisting of an alkali or alkaline earth metal (group 1 or 2) and a metal from group 11 to 16 with low to moderate electronegativity. [17] Ionic bonds are a crucial feature of Zintl phases. Those lead to a heteropolar structure and usually a high electrical resistivity. Therefore most Zintl phases are diamagnetic semiconductors.

Zintl phases based on antimony feature high  $zT$  values at medium to high temperatures. Prominent examples are  $\beta$ - $\text{Zn}_4\text{Sb}_3$ ,  $\text{Yb}_{14}\text{Mn}_{1-x}\text{Al}_x\text{Sb}_{11}$ ,  $\text{Al}_y\text{Mo}_3\text{Sb}_{7-x}\text{Te}_x$  and others compounds with  $\text{AB}_2\text{Sb}_2$  stoichiometry. ( $A = \text{Ca, Yb, Eu, Sr}$ ;  $B = \text{Zn, Mn, Cd, Mg}$ )  $\text{YbZn}_{0.4}\text{Cd}_{1.6}\text{Sb}_2$  has a  $zT$  of 1.2 at 700 K.  $\text{Eu}_2\text{ZnSb}_2$  has a  $zT$  of 0.6 at 700 K and  $\text{Eu}_2\text{Zn}_{0.96}\text{Sb}_2$  has a  $zT$  of 0.9 at 700 K. [18] Doping and substitution can enhance the electronic structure and therefore the power factor (section 2.5).

### Skutterudites

Skutterudite is a rare mineral with the ideal formula  $\text{CoAs}_3$ . Usually it contains also nickel and iron, since those occur as a coupled substitution with cobalt in solid solution. It forms a cubic crystal structure and belongs to the same space group as Indium(III)-hydroxid. [19] Compounds with the same structure are called skutterudites.  $\text{CoSb}_3$ , as such an example, is a non-magnetic semiconductor with great thermoelectric potential, when dopants or substitution elements are introduced. [20] One can easily manufacture n- or p-type materials, by manipulating the number of electrons, due to the gap in its electronic band structure. Its peculiar crystal structure presents a large free space, where foreign elements can be introduced. [20] When those cages are filled, then one speaks of filled skutterudites with the formula:  $\text{MFe}_4\text{Sb}_{12}$ . Those foreign elements M can be alkali, alkaline earth or rare-earth metals, which are weakly bound. This leads to the so called “rattling” mode. It dramatically reduces the thermal conductivity, therefore increasing the  $zT$  value. In 2021,  $(\text{Sm, Mm})_{0.15}\text{Co}_4\text{Sb}_{12}$  achieved the highest  $zT$  value of 2.1 at 850 K. [21] This makes skutterudites one of the most promising and now second most researched thermoelectric material, next to bismuth tellurides.

### Clathrate compounds

A clathrate is a chemical substance consisting of a lattice that traps or contains molecules. [22] There are two types of clathrates: Clathrate hydrates and inorganic clathrates. Most clathrate hydrates are 85 mol % water. Clathrate hydrates are derived from organic hydrogen-bonded frameworks. Unlike hydrates, inorganic clathrates have a covalently bonded framework of inorganic atoms with guests typically consisting of alkali or alkaline earth metals. Due to the stronger covalent bonding, the cages are often smaller than hydrates. [23] In contrast to skutterudites, clathrates have 2 different crystallographic cages, that can be filled. Like skutterudites, clathrate exhibit a “rattling” mode, which decreases thermal conductivity. Inorganic clathrates generally follow the Zintl concept and are semiconductors by nature. Their electronic structure can be optimized via doping or substitution. Typical examples are  $\text{Sr}_8\text{Ga}_{16}\text{Ge}_{30}$ ,  $\text{Ba}_8\text{Ga}_{16}\text{Sn}_{30}$ ,  $\text{K}_8\text{In}_8\text{Sn}_{38}$  and  $\text{Si}_{30}\text{P}_{16}\text{Te}_8$ .  $zT$  values of 1.35 at 900 K were found for single crystals of  $\text{Ba}_8\text{Ga}_{16}\text{Ge}_{30}$ , which were manufactured using the Czochralski

method. [24] Widespread application is unrealistic due to 2 major factors: (1) Gallium is a by-product of bauxite, sulfidic zinc ores and coal. Most of it is already used in commercial products like LEDs. [25] (2) Germanium is also a by-product. It is recovered from sphalerite zinc ores, especially zinc-lead-copper deposits. [26] Like gallium, most of it is used in commercial products already such as fibre-optics, infrared optics as well as electronic and solar electric applications [27], while it is also used as catalyst for polymerisation of polyethylene terephthalate (PET). [28] Ongoing research is looking into replacing gallium and germanium.

### Magnesium silicide

Magnesium and silicon are abundant in the earth's crust and non-toxic. This would make  $\text{Mg}_2\text{Si}$  a prime candidate for future applications. The downside, manufacturing is expensive, due to magnesium's high vapor pressure and the explosive nature of the chemical reaction producing magnesium silicide. [29]  $\text{Mg}_2\text{Si}$  and  $\text{Mg}_2\text{Sn}$  crystallize in an antifluorite face-centered cubic structure. It has a band gap of 0.77 eV compared to the 1.12 eV of pure Si. It is an n-type semiconductor with a high mobility of charge carriers, which results in a high power factor. Doping with antimony and bismuth,  $\text{Mg}_2\text{Si}_{1-y}\text{D}_y$  ( $\text{D} = \text{Sb}$  or  $\text{Bi}$ ) raises the power factor to values over  $3 \text{ mW m}^{-1} \text{ K}^2$  with a  $zT$  between 0.56 and 0.86 at around 800 K.

### Magnesium antimonide

$\text{Mg}_3\text{Sb}_2$  is a Zintl phase material related to  $\text{CaAl}_2\text{Si}_2$ -type materials. Interest in this material class has grown over the past two decades due to its low and intermediate-temperature thermoelectric application. According to an article from 2019 [30] n-type Te-doped  $\text{Mg}_3\text{Sb}_2$ -based materials can keep up with commercial  $\text{Bi}_2\text{Te}_3$  or  $\text{PbTe}$  materials in terms of thermoelectric properties. Especially the low density of about  $4 \text{ g cm}^{-3}$  helps to achieve a low thermal conductivity for nanostructured samples between  $1 \text{ W m}^{-1} \text{ K}$  and  $1.5 \text{ W m}^{-1} \text{ K}$  at room temperature. [30]

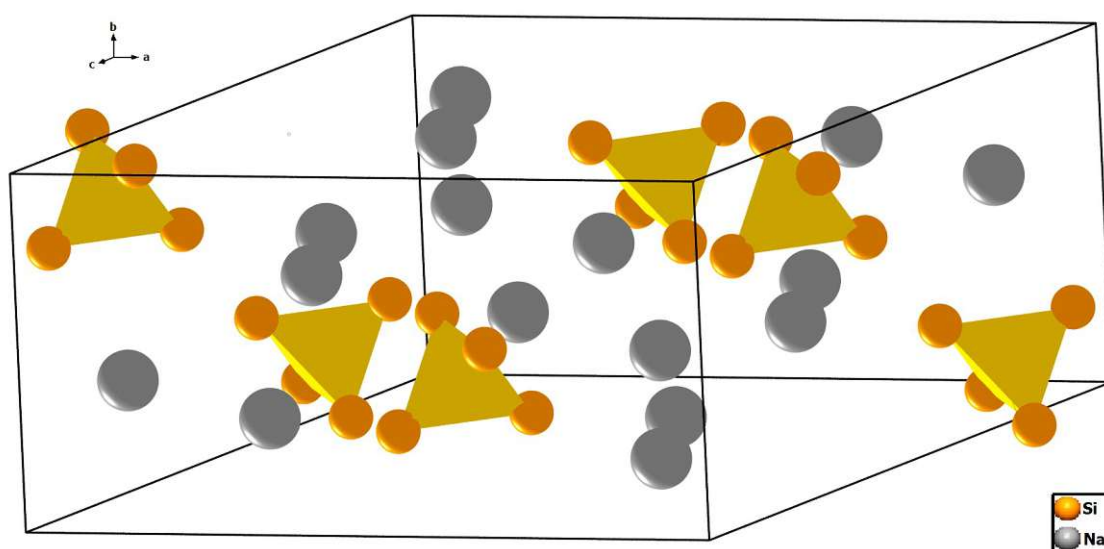


Figure 1.2: Schematic crystal structure of NaSi as an example for a Zintl structure [22]

### 1.2.3 Copper selenide

$\text{Cu}_2\text{Se}$  is a zero gap material with metal-like behavior [31], while copper-deficient  $\text{Cu}_{2-x}\text{Se}$  is a p-type semiconductor. [32] Copper selenide is an ionic conductor, an external field moves copper ions via diffusion. It also exhibits a reversible structural phase change at about 400 K. The low-temperature  $\alpha\text{-Cu}_2\text{Se}$  crystallizes in a base monoclinic structure, while the high-temperature  $\beta\text{-Cu}_2\text{Se}$  is of face-centered cubic structure. Carbon fibre and carbon nanotube doped  $\text{Cu}_2\text{Se}$  can reach  $zT$  values of 2.4 at temperatures of 850 K and 1000 K respectively, while phosphor-doped  $\text{Cu}_2\text{Se}$  exhibits a  $zT$  of 1.85 at 900 K. [33] While the ionic conduction impedes thermal conductivity, enhancing the  $zT$ , the phase transition and the ionic transport weaken the materials structure, when in use. Selenium and selenium compounds are toxic in doses higher than 400  $\mu\text{g}$ . It also damages skin and mucous lining upon contact. When inhaled, it leads to chronic lung problems.

### 1.2.4 Silicon-germanium

$\text{Si}_{1-x}\text{Ge}_x$  is a semiconductor alloy with any molar ratio of silicon and germanium. The primary application is as strained silicon for transistors for chip manufacturing [34], was also used in high temperature radioisotope thermoelectric generators for spacecrafts in the past. A research team at Eindhoven University of Technology believes, they can use silicon-germanium based materials to produce a direct band gap to emit light. Using a laser on a chip would increase data transfer speeds and reduce energy consumption. [35] Bulk silicon has a  $zT$  value of 0.01 at room temperature [36], while heterostructures can reach values of up to 1 at temperatures above 700 K. The high price of Ge isn't furthering the industrial-scale or commercial use.

### 1.2.5 Oxide based thermoelectric materials

The production of oxide based thermoelectric materials is cheap and environmentally friendly, compared to the other examples, mentioned above, on top of superb chemical and mechanical stability at high temperatures. The downside is the comparatively low  $zT$  value due to high electrical resistivity and high thermal conductivity. A common p-type material is  $\text{Ca}_3\text{Co}_4\text{O}_9$  and common n-types are  $\text{ZnO}$ ,  $\text{MnO}_2$ ,  $\text{NbO}_2$ ,  $\text{SrTiO}_3$ ,  $\text{NaCo}_2\text{O}_4$  or  $\text{CaMnO}_3$ . Single crystalline p-type oxides only reach  $zT$  values of up to 1. [37, 38] The more commercially viable polycrystalline materials show insufficient thermoelectric values. As for n-types, a thin film of  $\text{SrTiO}_3$  exhibited a  $zT$  value of up to 2.4. The bulk material has a  $zT$  of 0.7 at 1400 K. [39]

## 1.2.6 Heusler compounds

Heusler compounds consist mostly of two transition metals and a metal from the p-block arranged in a face-centered cubic structure. [40] If the stoichiometry is 1:1:1, the material is considered a "Half-Heusler", while a 2:1:1 is a "Full-Heusler" material. All of them exhibit properties which cannot be accounted for with just a classical understanding. The first known Heusler alloy  $\text{Cu}_2\text{MnAl}$  consists of non-ferromagnetic elements, while the compound itself is ferromagnetic. The reason for those interesting material properties is the electronic structure near the Fermi energy, emerging from the atomic order.

### Half-Heusler

Half-Heusler alloys have a typical composition of XYZ, where X is an early transition metal (group 3, 4 or 5), Y is a late transition metal (group 8, 9 or 10) and Z is a heavy main group metal (typically Sn or Sb, occasionally Ge, Pb or Bi). [41] Hafnium was used as a substitution element to increase  $zT$  values to 1.5 between 500 K and 700 K. Sadly, Hf is extraordinarily expensive, and not very suitable for commercial application. In recent years, two German companies claimed to be able to produce half-Heusler materials with a  $zT$  value close to 1 at industrial scale. Due to the latest technological advances, one can routinely produce half-Heusler compounds with  $zT > 1$ . [41] This makes them competitive with optimized skutterudites powders, while possessing higher mechanical and thermal stability. A large  $zT$  is not the only metric. Half-Heusler alloys naturally have a high power factor, when -for example- compared to chalcogenides, which achieve their highest  $zT$  by having a very low thermal conductivity.

### Full-Heusler

Whether  $\text{Fe}_2\text{VAI}$  is a semimetal with semi-conductor properties or a semiconductor with a small band gap of about 0.03 eV seems to be an ongoing debate. Evidence for both electronic structures have been reported. [42] The electronic structure, steep and flat bands, promotes a high power factor. Substitution or doping is crucial for enhancing its thermoelectric properties.  $zT$  for  $\text{Fe}_2(\text{V,W})\text{Al}$  is far below 0.1 at room temperature with slightly higher values for off-stoichiometric samples. [43, 44] The high thermal conductivity is a major barrier, that must be overcome.

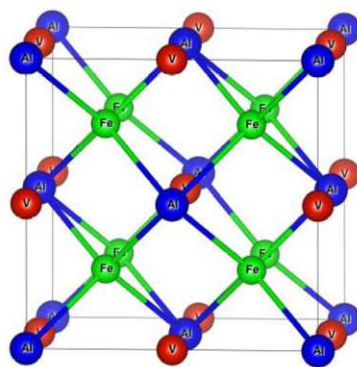


Figure 1.3: The crystalline unit cell of  $\text{Fe}_2\text{VAI}$  [44]

**(1) Further improvement - Reduction of Dimensions** One promising way would be the reduction of dimensions and dimensionalities. Thin film samples can show a meta-stable crystal structure, compared to the bulk material, in calculation and experimental data. Apart from element substitution, Substrate material and the material interface influence the thermoelectric properties. [45]

**(2) Further improvement - Off-stoichiometry** Off-stoichiometric compounds introduce anti-site defects. Some lattice sites, where the lesser concentrated element should sit, get occupied by the element with the higher concentration. A simple example would be  $\text{Fe}_2\text{V}_{1\pm x}\text{Al}_{1\mp x}$ , where vanadium occupies parts of the aluminium sites. This alters the number of valence electrons and therefore drastically alters the thermoelectric properties. [46] At a certain concentration of V-rich compositions, the Seebeck coefficient's sign flips, and then its absolute value increases, while the low temperature resistivity drastically increases. [47] These effects of disorder can also be achieved via the Anderson transition, where impurities percolate, forming a network through-out the entire sample. At the Anderson transition, a region of extended delocalized electronic states are formed, thanks to the critical density of impurities. [48]  $\text{Fe}_2\text{VAl}$  forms a fully ordered  $L2_1$  structure at low temperatures. At around 1400 K, in the  $B2$  phase, vanadium and aluminium will have swapped place randomly, while in the  $A2$  phase, at and above around 1550 K, the entire iron sublattice is uniformly filled with not only iron, but vanadium and aluminium at the stoichiometric ratio. [48]

**(3) Further improvement - High-pressure torsion** Stressing a sample by employing high-pressure torsion destroys the short-range order. The (111) and (200) peaks, corresponding to the  $L2_1$ -structure, completely disappear in XRD [section 3.2](#) due to the severe plastic deformation of the sample. [49] Strain gets released when annealing to a temperature of 900 K and completely removed at 1100 K. An un-annealed sample has lower electrical resistivity and thermal conductivity, but their Seebeck values are basically  $0 \mu\text{V}/\text{K}$  due to the atomic disorder introduced with the plastic deformation. Annealing the sample around 900 K restores the Seebeck and electrical resistivity, but leaves the thermal conductivity at the deformed value, due to the fine grain of the structure, effectively improving the figure of merit. This can be explained by the enrichment of the grain boundaries with substitution elements, which prevent grain growth during annealing. [49]

## 2 Theory

This chapter will focus on describing the physical quantities and effects important in the field of thermoelectricity in more detail. This should help the reader to understand the problems and builds up the necessary foundation for further enhancing thermoelectric properties and transport phenomena. The scenarios discussed here are mostly taken from the textbooks [3, 4, 50–55].

### 2.1 Transport phenomena

Phenomena like electrical and thermal conductivity are caused (at least in part) by charge carriers in the solid. Problems are time-dependent and external electrical fields disturbing the thermodynamic equilibrium. Over time, heat flows from hot to cold, electrons flow from negative to positive along an electrical field  $\vec{E}$ . Electric current  $I$  is the charge that flows, over time, in a system with a certain voltage  $U$  and a resistance  $R$ , following Ohm's law.

$$I = \frac{dQ_{charge}}{dt} = \frac{1}{R} \cdot U \quad (2.1)$$

$I$  is dependent on the area  $A$  the charge carriers pass through. Following Equation 2.1 and  $U = E \cdot l$  together with  $R = \rho \frac{l}{A}$ , the current density  $\vec{J}_{el}$  is proportional to the electric conductivity and the electric field.

$$\vec{J}_{el} = \frac{\vec{I}_{el}}{A} = \sigma \cdot \vec{E} = \frac{1}{\rho} \cdot \vec{E} \quad (2.2)$$

Heat is really similar as energy is transferred over time due to a temperature difference. The heat flow rate depends on the thermal conductivity  $\kappa$ , the cross section  $A$  and the temperature gradient  $\frac{\partial T}{\partial x}$ .

$$\frac{Q_{heat}}{\partial t} = -\kappa \cdot A \cdot \frac{\partial T}{\partial x} \quad (2.3)$$

Equivalent to the current density, the heat flux describes the flow of energy per unit of area over time.

$$\vec{j}_q = -\kappa \cdot \vec{\nabla} T \quad (2.4)$$

From here on we will try to describe, how charge carriers behave in the electronic band structure using solid state physics.

### 2.1.1 Semi-classic model

One can use classical mechanics to describe the movement of charge carriers, for example free electrons, with velocity

$$\frac{d\vec{r}}{dt} = \frac{d\vec{p}}{m}, \quad (2.5)$$

as well as an external force caused by an electrical and magnetic field

$$\vec{F} = -q(\vec{E} + \vec{v} \times \vec{B}), \quad (2.6)$$

and confine them to a lattice by superposing a Bloch wave. [54]  $q$  is used for any charge, while the elementary charge is  $1.602176634 \cdot 10^{-19}\text{C}$ . The infinite waves become localised wave packets with wavenumbers in an interval  $k - \frac{\partial k}{2}, k + \frac{\partial k}{2}$ . [53]

$$\Psi(x, t) = \int_{k-\frac{\partial k}{2}}^{k+\frac{\partial k}{2}} a(k) e^{i(kx - \omega(k)t)} dk \quad (2.7)$$

$E_j(\vec{k})$ , the energy of a crystal electron, and the external forces  $\vec{F}(\vec{r}, t)$  can be incorporated into the mechanics as

$$\vec{v} = \frac{d\vec{r}}{dt} = \frac{1}{\hbar} \frac{\partial E_j(\vec{k})}{\partial \vec{k}}, \quad E = \frac{\hbar^2 k^2}{2m} \quad (2.8)$$

and

$$\vec{F} = \hbar \frac{d\vec{k}}{dt} = \frac{\hbar^2}{\left(\frac{d^2 E}{dk^2}\right)} \frac{d\vec{v}}{dt}. \quad (2.9)$$

$\vec{v}$  describes the propagation speed of the wave packet.  $\vec{F}$  is the external force acting on electrons in the band structure. The effective mass  $m_{effective}$  of the charge carrier in the band structure is required to describe its movement correctly. This will be vital when looking into electrical resistivity subsection 2.2.1.

$$m_{effective} = \frac{\hbar^2}{\left(\frac{d^2 E}{dk^2}\right)} \quad (2.10)$$

While an external electrical field is present over a time  $dt$ , the energy of the wave packet is

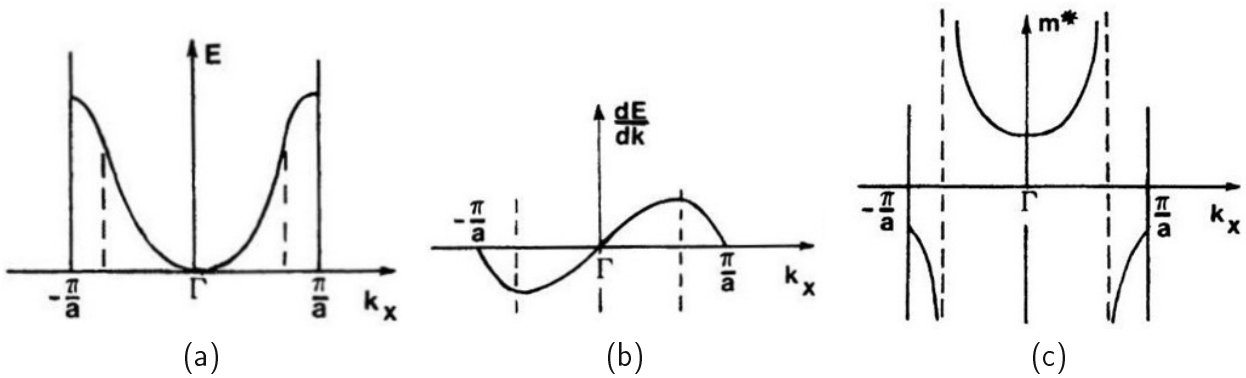


Figure 2.1: (a): Simple energy band  $E$ . (b): First derivative of the energy band  $dE/dk$ . (c): Inversion of the second derivative of the energy band  $1/(d^2E/dk^2)$ . [56]

increased.

$$\delta E = -q\vec{E} \cdot \vec{v} dt \quad (2.11)$$

Also the wave vector  $\vec{k}$  will change with increasing energy. Assuming that the external fields cannot induce band transitions, the bands will always have the same number of electrons, although more sophisticated descriptions also allow interband scattering. Considering the time-dependent Schrödinger equation for wave packets of Bloch states, one should note that the semi classic model cannot be used if the electrical field  $\vec{E}$  is too high or varies a lot over distance and time.

### 2.1.2 Boltzmann theory

[52–55] The Boltzmann transport equation is probably the most well known description of transport phenomena. It describes the driving force by external fields and the retardation via collisions of the charge carriers scattering centres. The Fermi-Dirac distribution function  $f_0$  gives the average number of electrons at a specific energy  $E(\vec{k})$ .

$$f_0(E(\vec{k})) = \frac{1}{e^{\frac{E(\vec{k})-\mu}{k_B T}} + 1} \quad (2.12)$$

$\vec{k}$  is a vector in reciprocal space. It is the way one looks at solids using diffractometry.  $\mu$  is the chemical potential. It is a form of energy responsible for phase changes and chemical reactions. In the simplest case the temperature is homogeneous and there are no external fields. If external forces are applied and collisions are left out, the electrons follow this equation:

$$f(\vec{r}, \vec{k}, t) = f(\vec{r} - \vec{v}dt, \vec{k} - (\vec{F}/\hbar)dt, t - dt) \quad (2.13)$$

To consider collisions, a correction term  $+(\frac{\partial f}{\partial t})dt$  has to be added. The partial derivative of semi-classical model with collision term reads

$$\left(\frac{df(\vec{r}, \vec{k}, t)}{dt}\right)_{coll} = \left(\frac{\partial f(\vec{r}, \vec{k}, t)}{\partial \vec{r}}\right)\left(\frac{\partial \vec{r}}{\partial t}\right) + \left(\frac{\partial f(\vec{r}, \vec{k}, t)}{\partial \vec{k}}\right)\left(\frac{\partial \vec{k}}{\partial t}\right) + \left(\frac{\partial f(\vec{r}, \vec{k}, t)}{\partial t}\right) + \dots \quad (2.14)$$

If we solve for  $\left(\frac{\partial f(\vec{r}, \vec{k}, t)}{\partial t}\right)$  with  $\left(\frac{\partial \vec{r}}{\partial t}\right) = \vec{v}$  and  $\left(\frac{\partial \vec{k}}{\partial t}\right) = \frac{\vec{F}}{\hbar}$  we get the Boltzmann equation:

$$\frac{\partial f}{\partial t} = -\vec{v}\nabla_{\vec{r}}f + \frac{-q}{\hbar}(\vec{E} + \vec{v} \times \vec{B}) \cdot \nabla_{\vec{k}}f + \left(\frac{\partial f}{\partial t}\right)_{coll} \quad (2.15)$$

### 2.1.3 Landauer theory

[50] The Landauer theory can be seen as alternate to the Boltzmann theory. It was originally developed to describe electric conductivity more elegantly, but can be generalized for more broad application. This microscopic theory is general and applies to inorganic and organic materials, crystalline and amorphous structures. [50] It takes the molecular level into consideration and can scale up to bulk materials. For example the net current through a single molecule is governed by the number of parallel transport channels  $\mathfrak{M}(E)$  and the transport probability  $\mathfrak{T}(E)$  through such a channel. Thus an electric current through a molecule between two electrodes is given by:

$$I = -\frac{2q}{h} \int_{-\infty}^{\infty} \mathfrak{T}(E)\mathfrak{M}(E)(f_2 - f_1)dE \quad (2.16)$$

Scaling up to a bulk material, the net current turns into a current density  $J$ . The difference in occupation becomes a gradient. Lastly combining  $\mathfrak{M}(E)$  and  $\mathfrak{T}(E)$  yields the transport function  $G(E)$ ,

$$\vec{J}_q = -q \int_{-\infty}^{\infty} G(E)\vec{\nabla}f dE. \quad (2.17)$$

$G(E)$  in a crystalline material consists of the mean square of the velocity of all the particles involved over their respective energy band, the relaxation time  $\tau$  after scattering, and the density of states  $D(E)$ .

$$G(E) = \langle v(E)^2 \rangle \tau(E) \cdot D(E) \quad (2.18)$$

The Landauer theory can be used for all sorts of particles, not just electrons and the gradient can be induced by a chemical, temperature or voltage difference. In our case, final expressions of both the Boltzmann theory and the Landauer theory for similar scenarios, however, are very similar.

## 2.2 Electrical resistivity

### 2.2.1 Simple model for electrical resistivity

Drude described electrical conductivity in metals as an ideal electron gas, moving through a bulk material. The driving force is an external field  $\vec{E}$ . The classical equation of motion looks like this:

$$m \cdot \frac{d\vec{v}}{dt} + \frac{m}{\tau} \vec{v}_D = -q \cdot \vec{E} \quad (2.19)$$

The term  $\frac{m}{\tau} \vec{v}_D$  describes friction.  $\tau$  is the mean free time between collisions and  $\vec{v}_D$  is the drift velocity which is defined by the flux  $\vec{J}_{el}$ , the charge  $q$  and the number of the charge carriers per volume  $n = \frac{n_{total}}{V}$ :

$$\vec{v}_D = \vec{v} - \vec{v}_{Fermi} = \frac{\vec{J}_{el}}{n \cdot q} \quad (2.20)$$

This simple model is in direct violation of the Pauli principle. Due to the difference of the effective mass  $m_{effective}$  subsection 2.1.1 electrons on the upper end of the band move in the opposite direction of those on the lower one. [54] Consider now a current in the smallest volume in phase space.  $\frac{1}{2\pi}$  is the factor for every direction getting the following infinitesimal current density in three dimensions:

$$d\vec{J} = \frac{2q}{(2\pi)^3} \vec{v}(\vec{k}) f(\vec{k}) = \frac{1}{4\pi^3 \hbar} \nabla_{\vec{k}} E(\vec{k}) d^3k \quad (2.21)$$

Note the factor 2 because of the electrons' spin directions!  $E(\vec{k}) = E(-\vec{k})$  We integrate over the first Brillouin zone to obtain the total current density,

$$\vec{J}_{el} = \frac{-2 \cdot q}{(2\pi)^3} \int_{1stBZ} \vec{v}(\vec{k}) f(\vec{k}) d^3k = \frac{-q}{4\pi^3 \hbar} \int_{1stBZ} \nabla_{\vec{k}} E(\vec{k}) d^3k. \quad (2.22)$$

In case of an partially filled band we integrate only over occupied states. This is different to holes. If we want to calculate their current, one has to flip the sign and integrate over all unoccupied states.

The definition of the specific electrical resistivity  $\rho$  is the resistance against an electric current over a given length. Generally it fulfills this relation.

$$\rho = \frac{1}{\sigma} = \frac{\vec{E}}{\vec{J}_q} \quad (2.23)$$

The electrical conductivity  $\sigma$ , which is the reciprocal of the resistivity, can be obtained by solving the Boltzmann equation, which for a constant electrical field  $\vec{E}$  reads [57]:

$$f(\vec{k}) = f_0(\vec{k}) - q \cdot \vec{E} \cdot \vec{v}(\vec{k}) \cdot \tau(E(\vec{k})) \cdot \left( \frac{-\delta f_0(\vec{k})}{\delta E(\vec{k})} \right) \quad (2.24)$$

Continuing, we calculate:

$$\rho = \int \frac{1}{\frac{-q \cdot \vec{v}(\vec{k}) \cdot \tau(E(\vec{k})) \cdot \left( \frac{-\delta f_0(\vec{k})}{\delta E(\vec{k})} \right)}{\frac{-2 \cdot q}{(2\pi)^3} \vec{v}(\vec{k}) f(\vec{k})}} d^3k = \frac{4\pi^3}{\int q^2 \cdot \vec{v}^2(\vec{k}) f(\vec{k}) \tau(E(\vec{k})) \cdot \left( \frac{-\delta f_0(\vec{k})}{\delta E(\vec{k})} \right) d^3k} \quad (2.25)$$

For solving this, one replaces the volume elements  $d^3k$  with surface elements  $dk_{\perp} \cdot dA_E = dA_E \frac{dE}{\hbar \cdot v(E)}$ . [58]  $v(E)$  here is the group velocity. Additionally assuming,  $k_B \cdot T \ll E_F$  allows to integrate over states with constant energy at the Fermi level  $E_F$ .

$$\rho = \frac{4\pi^3 \cdot \hbar}{q^2} \frac{1}{\int_{E=E_F} \frac{(\vec{v}^2(\vec{k}) \cdot \tau(E(\vec{k})))}{v(E)} dA_E} \quad (2.26)$$

With  $\int_{E=E_F} dA_E = 4\pi \cdot k_F^2$  and  $v(E = E_F) = \frac{\hbar \cdot k_F}{m}$ :

$$\rho = \frac{4\pi^3 \cdot \hbar}{q^2} \frac{1}{\frac{v^2 \cdot \tau \cdot 4\pi \cdot k_F^2}{\frac{\hbar \cdot k_F}{m}}} = \frac{4\pi^3 \cdot \hbar}{q^2} \frac{m}{\vec{v}^2 \cdot \tau \cdot 4\pi \cdot \hbar \cdot k_F^3} \quad (2.27)$$

And simplified one finally gets:

$$\rho = \frac{\pi^2}{q^2} \frac{m}{v^2 \cdot \tau \cdot k_F^3} = \frac{m_{effective}}{n \cdot q^2 \cdot \tau(E)} \quad (2.28)$$

### 2.2.2 Electrical resistivity using the Landauer theory

Alternatively one could derive the electrical conductivity with the Landauer theory [Equation 2.17](#) by adding a voltage gradient.

$$J_{\nabla U}^{\vec{}} = -q^2 \nabla U \int_{-\infty}^{\infty} G(E) \frac{-\delta f}{\delta E} dE \quad (2.29)$$

And using Ohm's law  $J = -\sigma \nabla U$  we end up with a conductivity:

$$\sigma = q^2 \int_{-\infty}^{\infty} G(E) \frac{-\delta f}{\delta E} dE \quad (2.30)$$

or resistivity

$$\rho = \frac{1}{q^2 \int_{-\infty}^{\infty} G(E) \frac{-\delta f}{\delta E} dE} \quad (2.31)$$

In contrast to the classical model, it considers the multiple scatter and transport possibilities of a propagating electron at a certain energy.

### 2.2.3 Electrical resistivity summary

Electrical resistivity  $\rho$  hinders the flow of electrical current  $J$ , when an electrical field  $\vec{E}$  is present. Resistivity is governed by the number of particles  $n$ , their charge  $q$  and ability to move unobstructed over a certain time  $\tau$ .  $q^2$  ensures that those particles can be either positive or negative. In essence, more free moving charged particles in a system, reduce the system's electrical resistivity. The electronic band structure of the material is also a contributing factor. Except for  $q^2$ , all the parameter mentioned above are summed up in the transport function  $G$  of the Landauer theory [subsection 2.2.2](#). In thermoelectric applications, a low electrical resistivity is necessary.

## 2.3 Thermal conductivity

### 2.3.1 Simple model for thermal conductivity

Analogous to the electrical conductivity, thermal conductivity can be defined by the heat flux  $\vec{J}_Q$  and the temperature gradient:

$$\kappa = -\frac{\vec{J}_Q}{\vec{\nabla}T} \quad (2.32)$$

The heat flux  $\vec{J}_Q$  gives the amount of heat energy  $Q$  flowing through an area  $A$  per time  $\delta t$ .

$$\vec{J}_Q = \frac{Q}{A \cdot \delta t} \quad (2.33)$$

In 1853 Wiedemann and Franz related the thermal conductivity  $\kappa$  of an ideal metal to its electric resistivity  $\rho$ :

$$\kappa_{el} = \frac{L \cdot T}{\rho} \quad (2.34)$$

With  $L$  being the so-called Lorenz number.

$$L = \frac{\pi^2}{3} \cdot \left(\frac{k_B}{q}\right)^2 = 2.44 \cdot 10^{-8} \text{V}^2\text{K}^{-2} \quad (2.35)$$

The Wiedemann-Franz law is surprisingly accurate for an empirically found relation. The factor  $2.44 \cdot 10^{-8}$  might not be correct for all materials, but other than that, the law fits metals for high and really low temperatures very well. Its major flaw is it only considers heat transfer by electrons. Therefore, the total thermal conductivity is a combination of electronic and phononic contributions [59]

$$\kappa = \kappa_{el} + \kappa_{ph}, \quad (2.36)$$

with

$$\kappa_{el} = \frac{\pi^2 k_B T}{3 q \rho} \quad (2.37)$$

and [54]

$$\kappa_{ph} = \frac{1}{3} c_{V(ph)} \cdot v \cdot \mathfrak{l}. \quad (2.38)$$

$\kappa_{el}$  is obtained by combining kinetic theory with the Sommerfeld model. The main factors are the number of charge carriers  $n$ , the specific heat of free electrons  $c_{V(el)}$  and the relaxation time  $\tau$ . We can use  $\rho$  from Equation 2.28:

$$\kappa_{el} = \frac{\pi^2 k_B T}{3 q} \frac{T}{\frac{m_{effective}}{n \cdot q^2 \cdot \tau}} = \frac{n \cdot \pi^2 \cdot k_B^2 \cdot T \cdot \tau}{3 \cdot m_{effective}} \quad (2.39)$$

Further more, we can use the kinetic energy formula  $E = \frac{m \cdot v^2}{2}$  and specific heat for electrons  $c_{V(el)} = \frac{\pi^2 \cdot k_B^2}{2} \cdot \frac{T}{E_F}$ , while using the Fermi-velocity to determine the mean free path  $\mathfrak{l} = v_F \cdot \tau$ . Only electrons in a range of  $\pm k_B T$  of  $E_F$  with  $v_F$  can take part in scattering processes. [53]

$$\kappa_{el} = \frac{n \cdot \pi^2 \cdot k_B^2 \cdot T \cdot \tau}{3} \cdot \frac{v_F^2}{2E_F} = \frac{n \cdot c_{V(el)}}{3} \cdot v_F \cdot \mathfrak{l} \quad (2.40)$$

The last step was using:

$$c_{V(el)} = \frac{\pi^2 \cdot k_B^2}{2} \cdot \frac{T}{E_F} \quad (2.41)$$

$\kappa_{ph}$  contains the specific heat  $c_{V(ph)}$ , while  $v$  - in this case - is the phonon group velocity and  $l$  is the mean free path.

$$c_{V(ph)} = \begin{cases} \frac{12 \cdot \pi^4}{5} \cdot k_B \cdot \mathfrak{L} \cdot \left(\frac{T}{T_D}\right)^3, & \text{if } T \ll T_D \\ 3 \cdot k_B \cdot \mathfrak{L}, & \text{if } T \gg T_D \end{cases} \quad (2.42)$$

Both the Debye model and the Einstein model are used for lower and higher temperatures, yielding for the latter the same result as the Dulong-Petit law. [53] The Debye temperature  $T_D$  is a consequence of the cut-off frequency  $\omega_D$  for waves of a harmonic chain of masses, meaning the upper frequency limit. [60] This describes the dynamics of a crystal lattice. The upper frequency limit is calculated using the volume  $V$  and speed of sound in the solid  $v_S$ . [53]

$$3 \cdot N = \int_0^{\omega_D} D(\omega) d\omega = \frac{3 \cdot V}{2 \cdot \pi^2 \cdot v_S^3} \int_0^{\omega_D} \omega^2 d\omega = \frac{V}{2 \cdot \pi^2 \cdot v_S^3} \omega_D^3 \quad (2.43)$$

and the Debye temperature is just

$$T_D = \frac{\hbar \cdot \omega_D}{k_B}. \quad (2.44)$$

### 2.3.2 Thermal conductivity using the Landauer theory

The Landauer theory - as mentioned in its own chapter [subsection 2.1.3](#) - can also be used for heat transport. Instead of a charge  $q$  we use  $-\nabla T$ . On top of that one also has to consider the particles carrying the heat. The second law of thermodynamics connects the heat transported by a particle to the entropy  $\mathcal{S}$ .

$$\delta Q = T \cdot \delta \mathcal{S} \quad (2.45)$$

$\mathcal{S}$  implicates a binomial distribution:

$$\mathcal{S} = k_B \cdot \log \Omega \quad (2.46)$$

with  $\Omega$  being the binomial coefficient:

$$\Omega = \binom{N}{c} = \frac{N!}{(N-c)! \cdot c!} \quad (2.47)$$

$N$  is the number of available spaces and  $c$  is the number of occupants. Electrons, which are fermions following the Pauli principle, have a different distribution than phonons, where multiple particles can occupy the same state. [50]

$$f_b(E) = \frac{1}{e^{\frac{E}{k_B \cdot T}} - 1} \quad (2.48)$$

While one fermion can occupy only one state, the fermionic Binomial coefficient looks like this:

$$\Omega_f(E) = \binom{D(E)}{D(E) \cdot f_0(E)} \quad (2.49)$$

For bosons the number of states effectively scales with the number of bosons.

$$\Omega_b(E) = \left( \frac{D_b(E) + D_b(E) \cdot f_b(E) - 1}{D_b(E) \cdot f_b(E)} \right) \quad (2.50)$$

$$\vec{J}_{el, \nabla T} = -\nabla T \int_{-\infty}^{\infty} G(E) \frac{(E - \mu)^2}{T} \cdot \frac{-\delta f}{\delta E} dE \quad (2.51)$$

For an open circuit situation, i.e. no voltage gradient, the only driving factor for electrons is the temperature:

$$\kappa_{temperature} = \int_{-\infty}^{\infty} G(E) \frac{(E - \mu)^2}{T} \cdot \frac{-\delta f}{\delta E} dE \quad (2.52)$$

More interesting is the voltage driven thermal conductivity, which induces a temperature gradient with a certain voltage applied.

$$\kappa_{voltage} = q \cdot \frac{\nabla U}{\nabla T} \Big|_{J=0} \int_{-\infty}^{\infty} G(E) \cdot (E - \mu) \frac{-\delta f}{\delta E} dE \quad (2.53)$$

One should notice  $\frac{\nabla U}{\nabla T}$  which relates temperature to voltage - thereby a foreshadowing of the upcoming Seebeck effect.

$$\kappa_{el} = \kappa_{temperature} - S^2 \frac{T}{\rho} \quad (2.54)$$

So far, only the electronic part of the thermal conductivity was considered. One can use the general heat transport Landauer equation to consider the lattice part:

$$J_Q = - \int_{-\infty}^{\infty} \frac{\delta Q}{\delta c} \cdot G(E) \cdot \vec{\nabla} f dE \quad (2.55)$$

and use the chain rule to relate the gradient of Bose-Einstein statistics with temperature gradient since phonons are of bosonic nature:

$$\vec{\nabla} f_b = \frac{\delta f_b}{\delta T} \cdot \vec{\nabla} T = \frac{E}{T} \cdot \frac{-\delta f_b}{\delta E} \cdot \vec{\nabla} T \quad (2.56)$$

$$J_{Q, \nabla T} = -\vec{\nabla} T \int_0^{\infty} G(E) \cdot \frac{E^2}{T} \cdot \frac{-\delta f_b}{\delta E} dE \quad (2.57)$$

$$\kappa_{ph} = \int_0^{\infty} G(E) \cdot \frac{E^2}{T} \cdot \frac{-\delta f_b}{\delta E} dE \quad (2.58)$$

### 2.3.3 Thermal conductivity summary

Thermal conductivity  $\kappa$  is a system's ability to transfer heat. It has 2 components. Heat can be transported by free charged particles described by  $\kappa_{el}$  or via lattice vibrations, which can be represented by a bosonic quasi-particle, a phonon, described by  $\kappa_{ph}$ . The electronic component can be directly linked with the electrical resistivity [section 2.2](#) as seen in the Wiedemann-Franz law [Equation 2.34](#). Jumping a bit ahead when looking at the Landauer theory [subsection 2.3.2](#) one can also link it directly to the Seebeck coefficient in [equation Equation 2.54](#). The lattice component of the thermal conductivity depends on the isochoric specific heat  $c_V$ , which gives the heat capacity per volume, as well as the phonon group velocity  $v$  and mean free path  $l$  of said phonons. It could also be described as relaxation time  $\tau = \frac{l}{v}$ , the time between scattering events. This means that the regularity and density of a material have a positive effect on the thermal conductivity, while any lattice defects have a negative impact. Using the Landauer theory [subsection 2.3.2](#), the characteristic of phonons behaving like light particles is emphasized. In thermoelectric applications, a low thermal conductivity is necessary.

## 2.4 Seebeck coefficient

### 2.4.1 Simple model for Seebeck coefficient

The Seebeck coefficient, also known as thermopower, is -as hinted in the previous section- the link between an electrical potential and a temperature gradient. "Free moving" charged particles diffuse due to the temperature gradient and induce an electrical field  $\vec{E}$ . In case of electrons with charge  $-q$  and an average velocity  $v$ , the diffusion velocity in a 1-dimensional model is given by [52]

$$\vec{v}_{diff} = \frac{1}{2}[v(x - v \cdot \tau) - v(x + v \cdot \tau)] \quad (2.59)$$

$\tau$  is the relaxation time between scattering events. The velocity  $v(T(x))$  is temperature dependent. One derives the first term around  $x_0$ , point of origin,  $v(T(x)) \approx v(x_0) + \frac{dv}{dx}(x - x_0)$  which further gives

$$\vec{v}_{diff} = \frac{1}{2}[v(x_0) + \frac{dv}{dx}(-v \cdot \tau) - v(x_0) - \frac{dv}{dx}(v \cdot \tau)] = -\tau \cdot v \frac{dv}{dx} = -\tau \cdot \frac{d}{dx}\left(\frac{v^2}{2}\right) = \frac{-\tau}{2} \cdot \frac{dv^2}{dT} \cdot \frac{dT}{dx}. \quad (2.60)$$

In 3 dimensions there is an additional  $\frac{1}{3}$  factor,  $v^2$  is the mean velocity squared and  $\frac{dT}{dx}$  can be written as  $\vec{\nabla}T$ .

$$\vec{v}_{diff} = \frac{-\tau}{6} \cdot \frac{dv^2}{dT} \vec{\nabla}T \quad (2.61)$$

The induced electrical field comes from drift:

$$\vec{v}_{drift} = \frac{-q \cdot \tau}{m} \vec{E} \quad (2.62)$$

In a stationary system diffusion and drift cancel each other out.

$$\vec{v}_{diff} + \vec{v}_{drift} = \frac{1}{3}\left(\frac{m \cdot v^2}{2}\right) \frac{d}{dT} \vec{\nabla}T + q \cdot \vec{E} \quad (2.63)$$

Written like this one sees the heat capacity per particle  $\frac{c_V}{n} = \left(\frac{m \cdot v^2}{2}\right) \frac{d}{dT}$ , which gives the easier expression:

$$\vec{E} = \frac{c_V}{-3 \cdot n \cdot q} \cdot \vec{\nabla}T \quad (2.64)$$

And this leads to the definition of the thermopower:

$$S = \frac{\vec{E}}{\vec{\nabla}T} = \frac{c_{V(el)}}{-3 \cdot n \cdot q} = -\frac{\pi^2 \cdot k_B}{6 \cdot n \cdot q} \cdot \frac{k_B \cdot T}{E_F} \quad (2.65)$$

Even though the definition seems solid it represents only simple metals. Complex materials do not follow this relation at all. More often than not one finds a positive Seebeck coefficient in experiments, even if this formula states otherwise. To get an accurate description one has to take the electron dispersion and the electronic density of states into account.

### 2.4.2 Seebeck coefficient using the Landauer theory

Using the insights from above as well as [Equation 2.23](#) and [Equation 2.36](#) one can write the Seebeck coefficient as follows with all the additional info from [subsection 2.2.2](#) and [subsection 2.3.2](#):

$$S = \frac{\vec{E}}{\vec{\nabla}T} = \frac{\rho \cdot \vec{J}_{el} \cdot \vec{J}_Q}{-\kappa} = \int_{-\infty}^{\infty} G(E) \cdot \frac{E - \mu}{T} \cdot \frac{-\delta f}{\delta E} dE \quad (2.66)$$

### 2.4.3 Seebeck coefficient summary

As seen in Equation 2.66, the Seebeck coefficient is composed of the electrical and heat current density  $J_{el}$ ,  $J_Q$  as well as the specific electrical resistance  $\rho$  and thermal conductivity  $\kappa$ . Higher electric resistivity and lower thermal conductivity have a positive effect. The Seebeck coefficient can be both positive and negative. For thermoelectric applications, materials with positive and negative Seebeck coefficients are needed.

## 2.5 Thermoelectric effect, Power factor and Figure of Merit

If there is a temperature gradient in the system, then heat is transferred from the hot area to the cold one. This either happens by charge carrying electrons or holes -in case of doped semiconductors- and phonons, which are quasi particles describing lattice vibrations. Since metals have free electrons available, they are good electric and thermal conductors. More important than movable carriers is the ability to retain a gradient. This is, where the Seebeck coefficient  $S$  has to be mentioned.

$$U_{Thermal} = -S(T_1 - T_2) \quad (2.67)$$

Here an example: The electric potential of a temperature gradient of 100 K along 2 different connected metals vanishes quickly, the voltage across the system is only a few mV [61]. If one conducts the same experiment with a doped semiconductor, one finds a higher voltage, usually several 100 mV, which translates to  $10 \mu\text{V K}^{-1}$ . We conclude that the thermoelectric effect strongly depends on thermodiffusion of charge carriers. As one also realizes, good thermal conductivity is detrimental to the goal of a thermoelectric element. One wants to retain the temperature gradient, so a thermal conductivity is actually counter productive, unless it comes from charge carriers. Those can be used to control the propagation of heat. Or they flow as a current, when a temperature gradient is present. To wrap up with a final statement: The goal is a high figure of merit  $zT$ , meaning a high thermoelectric performance at a given temperature  $T$ .

$$zT = \frac{S^2}{\rho \cdot \kappa} \cdot T = \frac{PF}{\kappa} \cdot T \quad (2.68)$$

In literature  $\frac{S^2}{\rho}$  are often combined into the so-called Power factor  $PF$ .

Obviously it is not possible to change any of those quantities without changing another, since the electrical resistivity  $\rho$ , Seebeck coefficient  $S$  and thermal conductivity  $\kappa$  are inevitably connected. Raising the Seebeck coefficient as a result of reducing the charge carrier concentration  $n$  Equation 2.65 reduces the thermal conductivity Equation 2.37 but also the electrical conductivity  $\sigma$ . A balance must be struck to get:

- A high Seebeck coefficient  $S$ , by tuning the band structure to get a high density of states at the Fermi level (Equation 2.65 and Equation 2.66)
- A low electrical resistance  $\rho = \frac{1}{\sigma}$ , by introducing highly mobile charge carriers  $n$  (Equation 2.28)
- A low thermal conductivity  $\kappa$ , by increasing phonon scattering, decreasing  $l$  in Equation 2.38, since we do not want to touch the charge carriers

## 2.6 Electronic band structure manipulation

This work documents the efforts and results of trying to improve the thermoelectric performance of the Full-Heusler alloy (subsection 1.2.6)  $\text{Fe}_2\text{VAl}$ , by substituting vanadium with tungsten and tantalum.  $S(T)$  and  $\rho(T)$  in  $\text{Fe}_2\text{VAl}$  are highly temperature dependent and its maximum power factor is around 300 K, followed by a steep drop. For many technical applications a peak performance at room temperatures would be preferred. The Seebeck coefficient plays the biggest role for thermoelectrics and it is small for pure  $\text{Fe}_2\text{VAl}$  at about  $75 \mu\text{V K}^{-1}$  at about 200 K and about  $65 \mu\text{V K}^{-1}$  at room temperature. [62] For comparison, pure iron's Seebeck coefficient is  $14 \mu\text{V K}^{-1}$ , aluminium's is  $-1.5 \mu\text{V K}^{-1}$  and copper's is about  $1.5 \mu\text{V K}^{-1}$  at room temperature. [63] Substituting elements in  $\text{Fe}_2\text{VAl}$  on all lattice sites is a promising strategy. It is used to manipulate not only the lattice constant but also the electronic structure of the solid. Changing the valence electron concentration (VEC) slightly can have a huge effect on the Seebeck coefficient, as several experiments show Figure 2.2a. Doping with electron acceptors in the V site lead to a slightly higher  $S$ . Having an electron donor on any lattice space, like tungsten, replacing Fe, V or Al leads to a negative  $S$  with a higher magnitude. Low-temperature  $\rho$  also drops significantly with a slightly higher VEC, which this work also confirms.

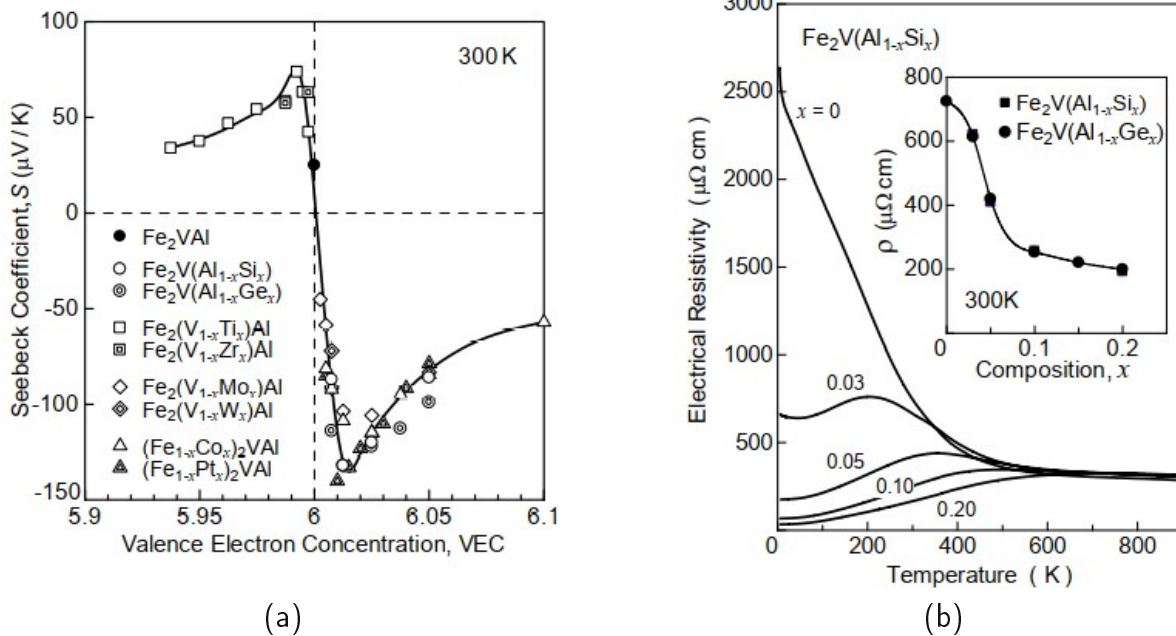


Figure 2.2: (a): Seebeck coefficient as a function of valence electron concentration of pure and doped  $\text{Fe}_2\text{VAl}$  systems. [47] (b): Temperature dependent electrical resistivity of  $\text{Fe}_2\text{VAl}_{1-x}\text{Si}_x$  and comparison to  $\text{Fe}_2\text{VAl}_{1-x}\text{Ge}_x$  in regards to the composition. [47]

Tantalum is iso-electronic to vanadium, meaning, they have the same number of valence electrons for bonding. Its role is to put strain on the lattice and increase phonon scattering. Looking further ahead, tantalum also increases the electronic band gap, as seen in Figure 4.1.

## 3 Experimental methods

In the following, an overview on  $\text{Fe}_2(\text{V},\text{Ta},\text{W})\text{Al}$  sample synthesis will be given.

### 3.1 Synthesis

All the elements - iron, vanadium, aluminium, tantalum and tungsten - were handled with gloves or tweezers during weigh out and cleaned with ethanol in between melting stages.

#### 3.1.1 Sample preparation

Fe was taken from a pure iron rod which was cut with a Struers Labotom into manageable pieces. V was supplied by "smart elements" in small globules of varying masses around 1.3 g. Purity was 99.93%. A 500 g Al ingot was supplied by Alfa Aesar. (Figure 3.1a) It's purity was 99.999%. W was available in pellets of 0.14 g to 0.32 g while Ta was a foil of 99.95% purity. Every element (with the exception of W) was cut and filed with separate tools to avoid cross-contamination. Since tungsten was too hard to work, pieces with the right mass were chosen and weighed the other elements accordingly to get the correct stoichiometry. A precision scale from Sartorius was used to weigh each element to  $\pm 50 \mu\text{g}$ . (Figure 3.1b)



Figure 3.1: (a): Cutting pieces out of the aluminium block using a special saw blade. (b): Precision weighing vanadium using a Sartorius scale.

Target masses were 4 g at first, while the last 3 samples had 7 g to be able to get sample pieces big enough to fit into the new equipment for measuring thermal conductivity. Samples with the following stoichiometry of  $\text{Fe}_2\text{V}_{1-x-y}\text{Ta}_x\text{W}_y\text{Al}$  have been successfully prepared:

- $x=0.025, y=0.050$
- $x=0.050, y=0.075$
- $x=0.050, y=0.100$
- $x=0.025, y=0.075$
- $x=0.025, y=0.100$
- $x=0.075, y=0.100$

Other samples were prepared, but failed to show the Heusler phase due to insufficient heating during the melting process or segregation due to the high doping:

- $x=0.050, y=0.050$
- $x=0.075, y=0.125$
- $x=0.100, y=0.100$
- $x=0.100, y=0.125$

### 3.1.2 Melting process

High frequency induction melting was the preferred method to produce the desired alloy. For the general setup: The inside consists of an elongated water-cooled copper pipe with boats for up to 3 samples. Around that, to decouple from the atmosphere, a quartz glass tube. This tube was evacuated and then filled with argon gas for the melting process. Metals, especially refractory metals, usually oxidise at high temperatures before they start melting when in contact with oxygen. A water-cooled copper coil winds around the tube over the length of a single boat. A current, with a maximum of over 3 A at almost 9 kW and a frequency of 400 kHz [46] through the coil, induces eddy currents in the sample materials via Faraday's law of induction [52]. This causes them to heat up, melt and chemically bind.

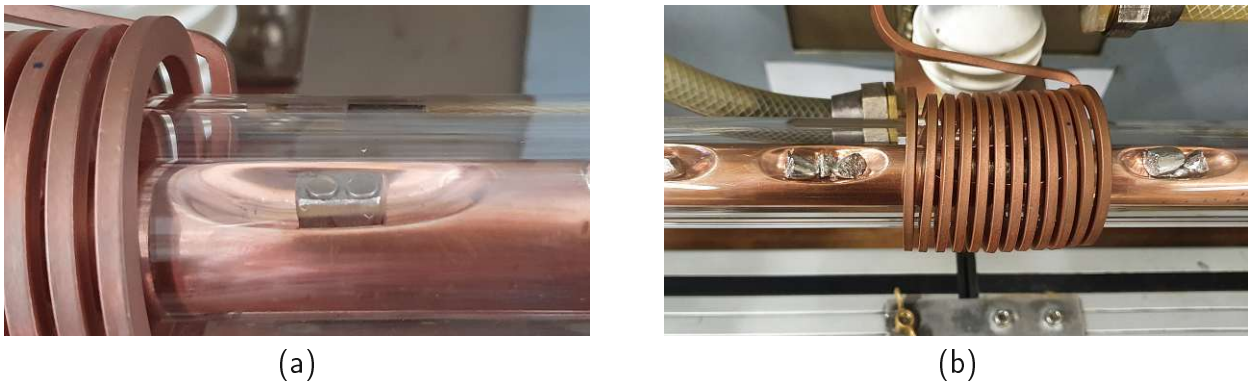


Figure 3.2: (a): Water-cooled copper boat with iron cube and tungsten pellets on top. (b): Broken samples rearranged for melting.

Melting Fe and W first (Figure 3.2a) is appropriate since the W-pieces have a very high melting point of nearly 3700 K. The resulting alloy has a drastically reduced melting point compared to pure tungsten.

element	melting point [K]	boiling point [K]
Iron	1811	3134
Vanadium	2183	3680
Tantalum	3290	5731
Tungsten	3695	5828
Aluminium	933	2792

Table 3.1: Values for melting and boiling point of the used elements [65]

After two or three repetitions, breaking the piece and putting it together in different orientation (Figure 3.2b), V and Al were added and the process was repeated. Aluminium's boiling point is lower than tantalum's (and tungsten's) melting point, but since the foil had such a high surface-to-bulk ratio, Ta was added during the last reruns. A great effort was made, melting and breaking the samples another four to five times just to be sure that the final product would have the desired composition and thus the appropriate crystal structure.

### 3.1.3 Annealing

All samples -except the last three- were annealed right away. For this procedure they were put in quartz glass tubes, which were then evacuated and sealed. This again prevents oxidation or other gasses permeating the sample. The annealing temperature was 1073 K for 7 days. Afterwards they cooled down inside the oven over a few hours. The last three samples were first measured and then annealed.



Figure 3.3: Quartz glass containing sample getting evacuated and then sealed via melting.

### 3.1.4 Cutting

To determine the material properties accurately, the samples had to be cut into precise shapes. Small rectangles are preferred for most of the following experiments with a cross section of 2 by 1.5 mm and a length over 10 mm. For the experiment in [section 3.7](#), especially to fit into the device to measure thermal diffusivity ([subsection 3.7.3](#)), samples were cut into  $6 \times 6 \times 1$  mm platelets. A Struers Accutom-10 and Struers 50A15  $\text{Al}_2\text{O}_3$  cutting discs, for appropriately shaping the samples, were used. Those alumina discs are especially suitable for hard ferritic alloys. The samples were glued to metal platelets, which could be firmly mounted in the machine, but if the rotation speed was too high, the sample would be ripped off the metal plate. Optimal settings were:

- Rotation Speed: 2500 Rotations/min
- Advance:  $5 \mu\text{m s}^{-1}$  to  $15 \mu\text{m s}^{-1}$



(a)



(b)



(c)



(d)

Figure 3.4: (a), (c): Sample pieces glued to a metal platelet for optimal mounting.  
 (b): View into the Accutom-10 while cutting a sample.  
 (d): Final sample piece measured with a micrometer caliper.

## 3.2 X-ray diffractometry

X-ray diffraction was performed in order to check, whether the sample crystallized in the Heusler structure and to obtain the respective lattice parameter. Preparation and measurement were performed on a X'Pert MPDII ("Luthien") diffractometer. Otherwise unusable sample pieces, left over after cutting, were smashed into tiny fragments inside a tungsten carbide receptacle and then pulverised in a ceramic mortar with a pestle. Diffractometry is widely used for structure analysis. A monochromatic beam of penetrating radiation is used at different angles. As an example for Bragg's law, interfering backscattered radiation gives the distance between crystallographic planes according to

$$n \cdot \lambda = 2 \cdot d \cdot \sin(\theta). \quad (3.1)$$

Multiple  $n$  of the wavelength  $\lambda$  are equal to twice the distance between crystallographic planes  $d$  times sinus of the beam angle  $\theta$ . If the interference pattern matched up with the known  $\text{Fe}_2\text{VAl}$  structure, the sample was considered good and further measuring would commence.

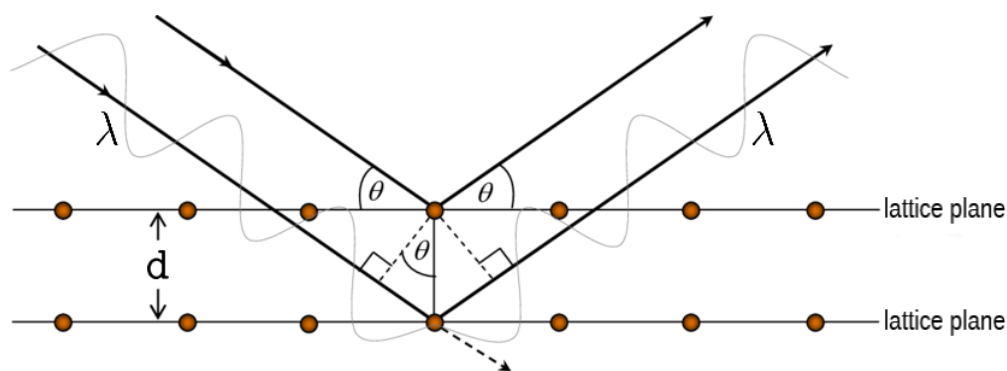


Figure 3.5: Conditions for diffraction and derivation of Bragg's law. Incoming light gets scattered at different lattice planes. Image from: researchgate.net [66]

Measurements were taken with  $\text{CuK}_{\alpha 1}$  radiation at an angle at least between 20 degree and 100 degree.

### 3.3 High-temperature resistivity and Seebeck measurements

Resistivity and Seebeck measurements at high temperature, meaning above room temperature, were conducted using the ULVAC-Riko ZEM-3. [67] In about half a day one can figure out both quantities with minimal effort in a 400 K to 500 K temperature range. The device heats the sample via an infrared heater and measures the sought-after quantities using the two contacts (Figure 3.6) and the electrodes at both ends of the sample. The measurement atmosphere was helium gas at 0.2 bar after flushing the chamber three times. The only parameter required is the cross sectional area of the sample and a piece long enough to fit between the electrodes. The same sample piece is used to measure the Seebeck coefficient, electrical resistivity and thermal conductivity at low temperatures.

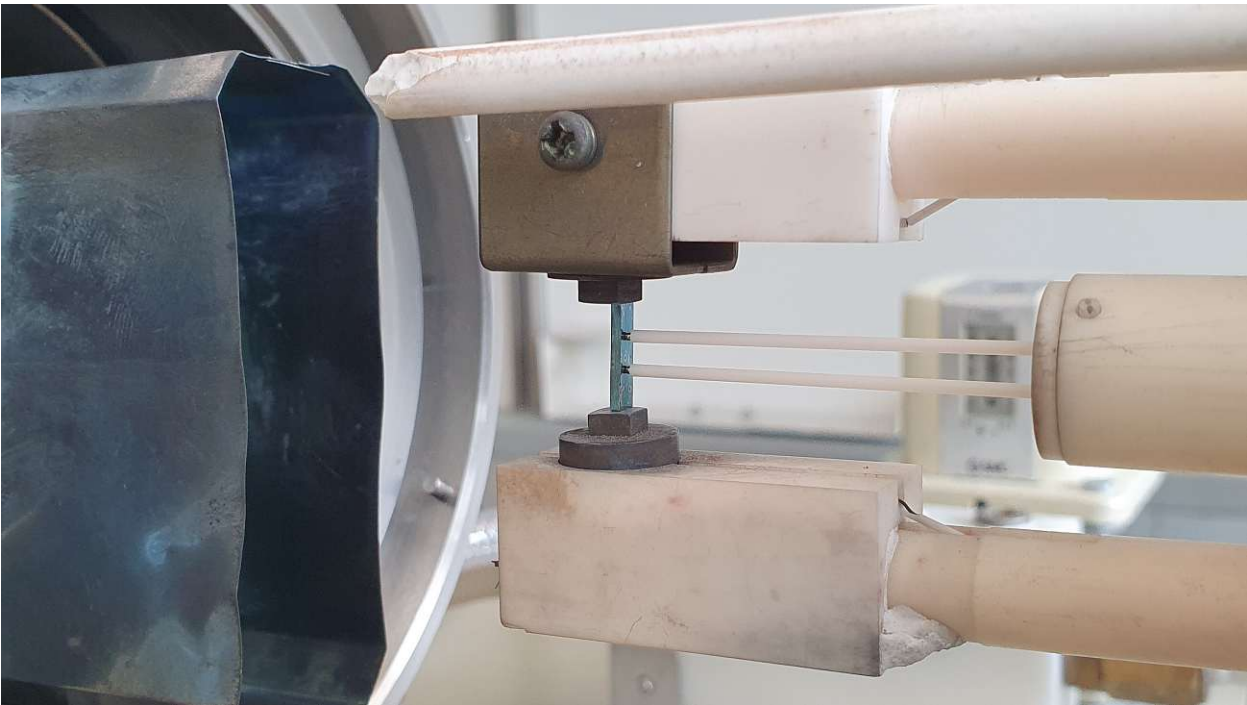
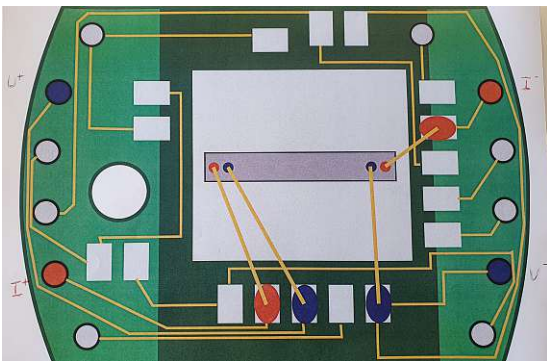
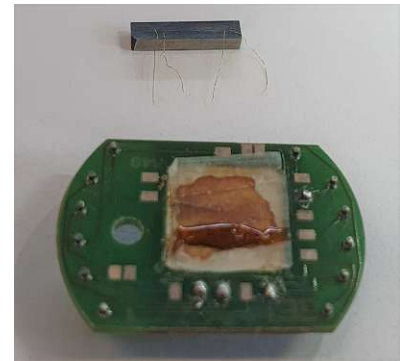


Figure 3.6: Sample inbetween the prongs and contacts on



(a)



(b)

Figure 3.7: (a): Puck layout. (b): Sample with wires at top and puck with varnish below.

### 3.4 Low-temperature electrical resistivity

For measuring the electrical resistivity below room temperature, down to 4 K, the sample had to undergo another preparation step. Four 50  $\mu\text{m}$  thick gold wires were spot-welded to the sample and the distance between the innermost wires was measured using a microscope. This ensures a high accuracy of the following 4-point measurement. The sample was then glued to a puck [Figure 3.7](#) using varnish and the gold wires were connected via solder to the puck's contacts. The puck could then be placed onto the measuring stick, equipped with a shield. The whole stick was then put into the cryostat, [Figure 3.8](#), evacuated and then filled with liquid helium. The controlling program on the computer was started and measurements were taken automatically in regular temperature intervals, while the system was cooling down as well as warming up back to room temperature. The resistance can easily be calculated with the voltage and currents used in combination with the sample geometry.

$$\rho = \frac{U}{I} \cdot \frac{A}{l} \quad (3.2)$$

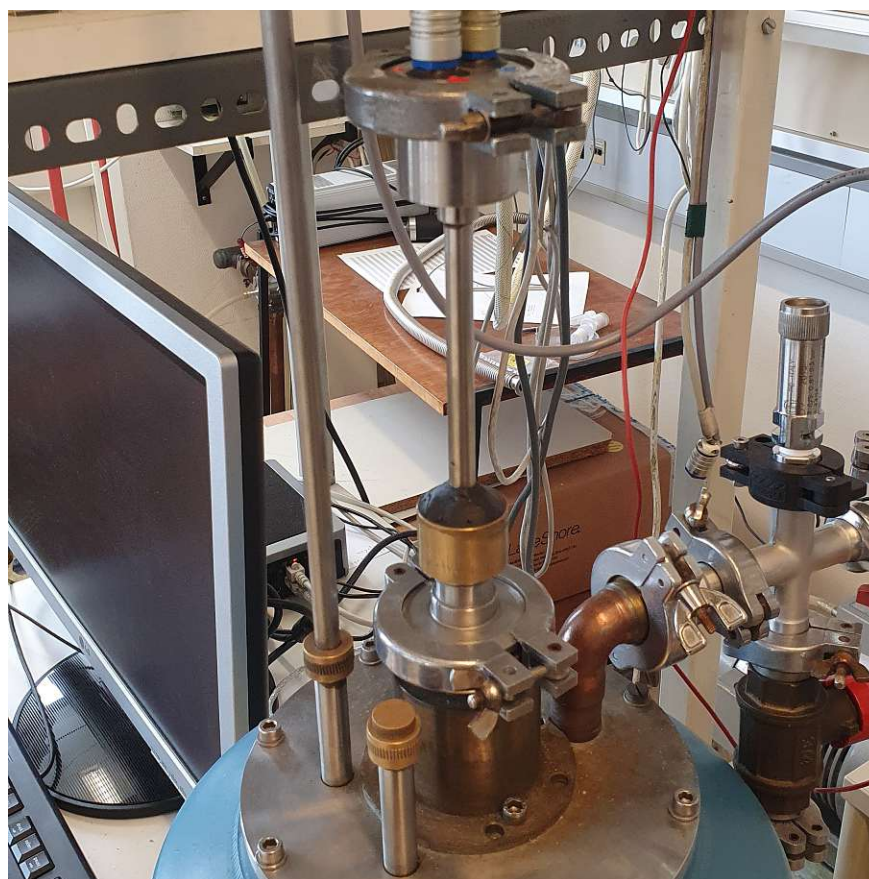


Figure 3.8: Measuring stick placed into the cryostat (blue cylinder) for low-temperature electrical resistivity measurement.

### 3.5 Low-temperature Seebeck coefficient

In preparation for the experiment, three copper wires got twisted. One end was flattened and then welded to the sample. Then the welded parts got treated with a two component silver glue, which was hardened for 20 min in the oven at 160°C. Then the sample was glued into another measuring stick onto some resistive wire strains for heating. The copper wires then were soldered to the thermocouples for measuring. A shield was placed over the sample and the entire measuring setup was sealed inside sample holder with the help of some indium wire. Then the sample holder got placed into a cryostat. Unlike the other device for measuring low-temperature electrical resistivity, this one has to be evacuated. The vacuum ensures that there is no interaction between any gasses or liquids with the sample, so to allow a stable temperature during measurement.

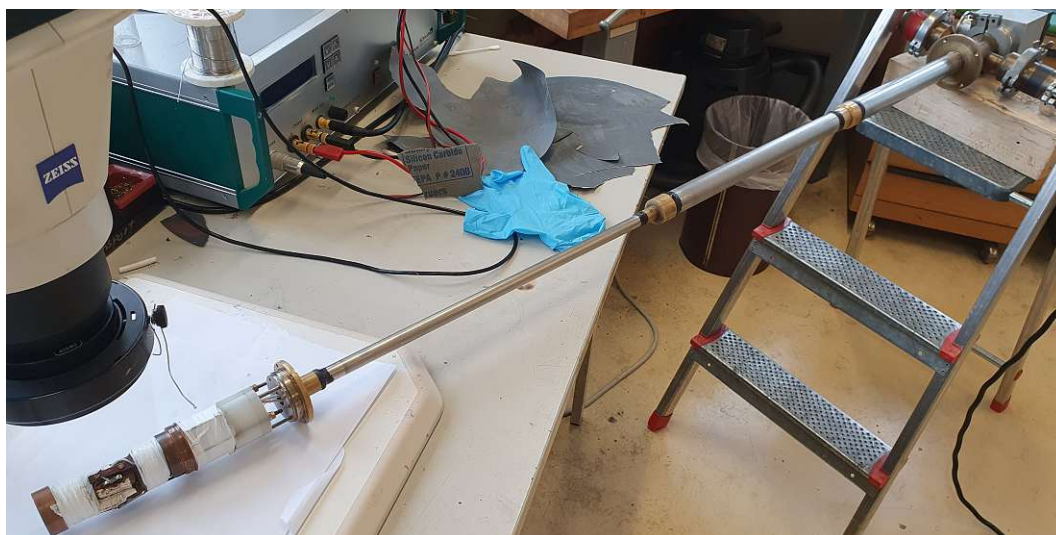
$$S = \frac{U_1 - U_2}{T_1 - T_2} \quad (3.3)$$



(a)



(b)



(c)

Figure 3.9: (a): Twisted wires welded to the sample. (b): Sample (with silver glue on top) glued onto resistive wire strains (with resin) for heating. (c): Measuring device; measuring the contact distance with the microscope.

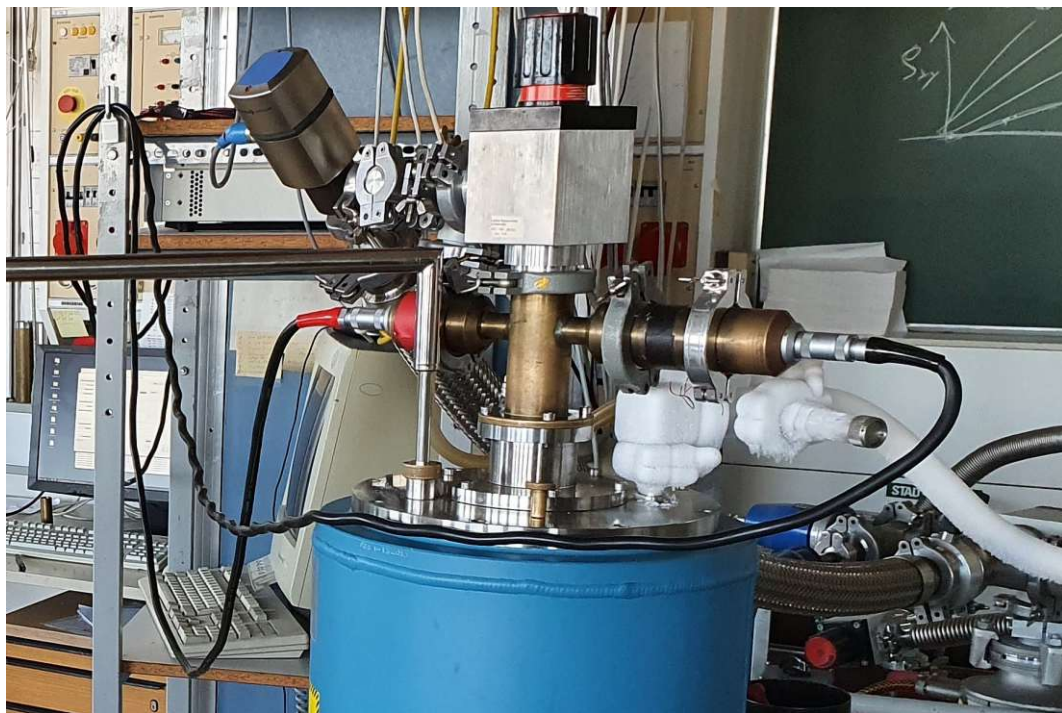
Test measurements were done to ensure the welding and gluing provided a solid connection. [Figure 3.9](#) After the two shields got applied, [Figure 3.10a](#) [Figure 3.10b](#), the measuring device was placed into the cryostat and the sample chamber was evacuated. If the target pressure of 0.1 mbar was reached the Indium-seal was considered stable and one could proceed. Liquid helium was transferred into the cryostat and the sample space was flushed with the gas. Upon reaching 4 K on the sample the feed of helium was stopped, the sample space was evacuated again and the measurement could be started.



(a)



(b)



(c)

Figure 3.10: (a): First radiation shield applied. (b): Second shielding to ensure vacuum condition. (c): Setup for Low-temperature Seebeck measurement, measuring device inserted into the cryostat (blue cylinder).

### 3.6 Low-temperature thermal conductivity

Samples were prepared by gluing resistive strain gauges with Stycast on top of the sample. They were used for heating. It seems wasteful, but strain gauges are extremely precisely manufactured, therefore their heating properties are the same with every experiment, so the results are comparable. Then copper wires were wrapped around the samples. The wires each got twisted together, then covered with solder. This ensures proper thermal contact with the sample surface. The principle of measurement is rather simple:

$$\kappa = \frac{\dot{Q} \cdot l}{(T_1 - T_2) \cdot A} \quad (3.4)$$

The sample gets heated on one side and cooled via a heatsink on the other side.  $\dot{Q}$  is the heat input via the heater, which gets divided by the temperature difference  $(T_1 - T_2)$  between the two measuring points that are a distance  $l$  apart on a sample with a cross sectional area of  $A$ . So the sample got dipped into thermal grease and then clamped onto the heatsink. The resistive strain gauges got hooked up to the power supply wires and temperature probes were attached to the sample's copper wires with solder. The inner radiation shield was screwed over the sample space and all the cables were connected to measure heating current, sample as well as shield temperatures. Of course an outer shield needs to be applied and tightly screwed down to ensure vacuum conditions during the measurement. The whole setup was sitting on a long thin pipe which then was put directly into liquid helium, which was then pumped into the entire setup. To reach the desired temperature, a screw-like heat exchanger was used to cool and set constant temperatures via a PID temperature controller Lakeshore 91C.

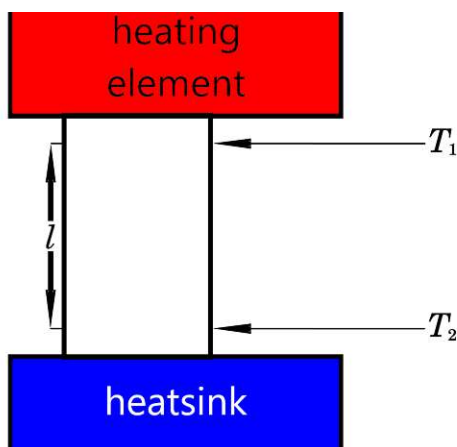


Figure 3.11: Principle setup for low-temperature thermal conductivity measurement.



Figure 3.12: Outer shield with valves for the vacuum pump and helium pipe.

After some troubles with the calibration and more time spent on fixing the setup instead of measuring, it was decided not to feature those measurements here.

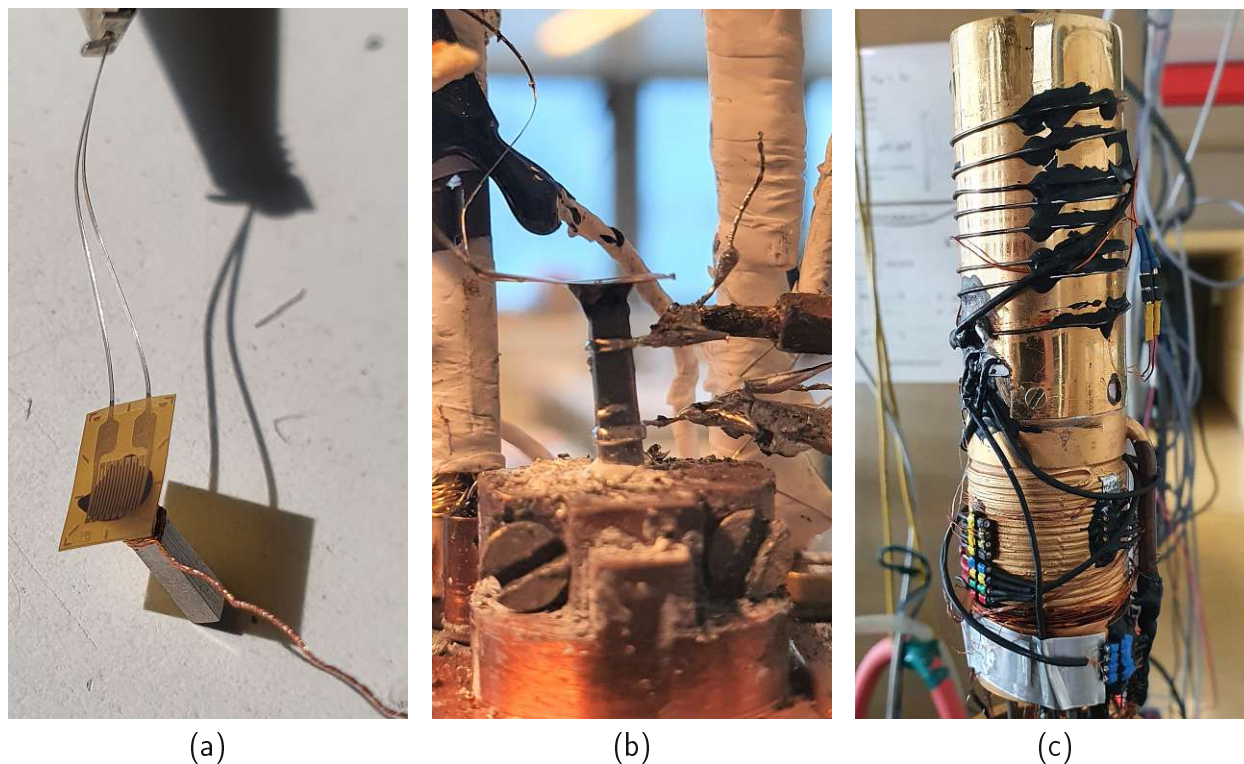


Figure 3.13: (a): Wiring up a sample after heating element is applied. (b): Sample fixed in the heatsink (bottom), temperature probes connected (right) and heating element connected. (c): Inner radiations shield applied and sensor wires connected.

## 3.7 High-temperature thermal conductivity

The thermal conductivity at and above room temperature was measured employing the “flash method” (subsection 3.7.3) according to:

$$\kappa = \frac{\alpha}{\rho_d \cdot c_p} \quad (3.5)$$

The next sections explain how the values for thermal diffusivity  $\alpha$ , density  $\rho_d$  and specific heat  $c_p$  were measured to obtain the thermal conductivity  $\kappa$ .

### 3.7.1 Specific heat

$c_p$  was determined by measuring a small sample piece of around 50 mg with a Linseis DSC PT 10<sup>TM</sup> against an empty sample holder. For this a fragment was used, which was weight and filed down precisely to fit into the sample holder.

$$c_p = \frac{1}{m} \cdot \frac{dQ}{dT} \quad (3.6)$$

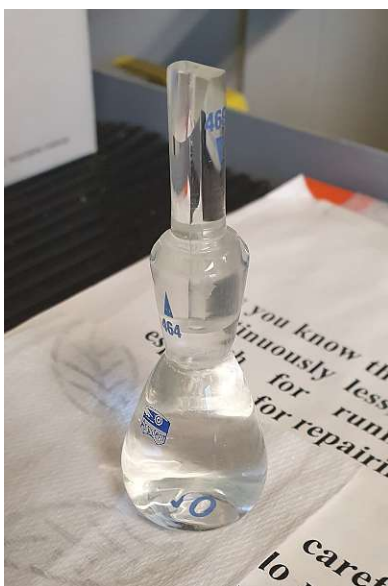
$dQ$  is the amount of heat required to raise the temperature of the piece by  $dT$ .



Figure 3.14: Sample holder for specific heat( $c_p$ )-measurement.

### 3.7.2 Density

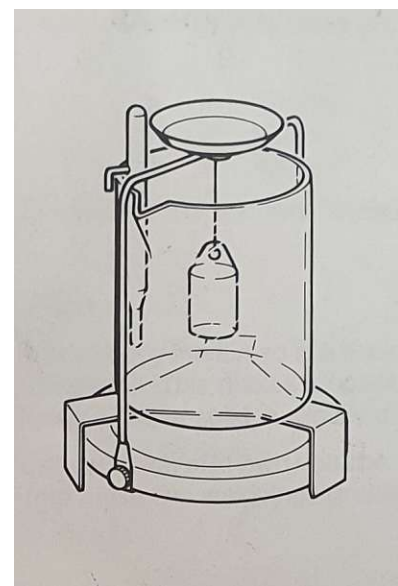
Measuring the density  $\rho_d$  accurately had proven to be more difficult than imagined. It turns out that small deviation in the precise weighing of the pycnometer and sample led to huge deviations in measured density. This is because the sample volume is too small in relation to the pycnometer. Luckily there was the possibility to access a hydrostatic balance device at the University of Vienna. Weighing the sample inside a liquid against an empty sample holder with the sample on top proved to be very accurate.



(a)



(b)



(c)

Figure 3.15: (a): Pycnometer with distilled water. (b): Scale for hydrostatic balance. (c): Sketch for hydrostatic balance in the instruction manual.

### 3.7.3 Thermal diffusivity

Thermal diffusivity  $\alpha$  is the velocity that heat travels through the sample. A standard flash method was used, Linseis LFA 500<sup>TM</sup>, where a precise light pulse heats the sample on one side and while the temperature on the other side of the sample is measured.

$$\alpha = \frac{1}{\nabla^2 T} \cdot \frac{\delta T}{\delta t} = 0.1338 \cdot \frac{l_{thick}^2}{t_{1/2}} \quad (3.7)$$

[68] The samples thickness  $l_{thick}$  was measured before the sample was coated with a thin carbon layer for optimal absorption. The Linseis LFA 500<sup>TM</sup> - Light Flash Analyzer [Figure 3.16](#) measured the temperature and then took the time of the half maximum of the diffusion curve. To fit into the machine, the sample had to be a very specific size of 6 by 6 mm and not more than 1.5 mm thick. This was one reason, why new samples were produced.



Figure 3.16: Laser flash apparatus Linseis LFA 500<sup>TM</sup>

### 3.8 Scanning electron microscopy

Sample preparation for electron microscopy measurements is time consuming. First of all, the sample surface has to be flat. One sands the surface with increasingly finer abrasive paper for progressively longer times. The final stage is polishing and wiping down with acetone.



Figure 3.17: (a): Sample embedded in wax prepared for sanding. (b): Struers Planopol-2 polisher

The sample was glued to the sample holder with double sided tape and grounded with silver paste. Non-conductive or non-grounded objects are impossible to be studied under an electron microscope. The sample also has to withstand the vacuum inside the sample chamber. We used a FEI Quanta 250 FEG [69] at USTEM at TU Wien [70]. A beam of electrons is used to partially scan the sample at different magnifications and positions. Electrons from various depths and different energies can be detected at different angles with several detectors. X-rays created in the process can be used too, to analyse the sample. This allows to interpret the topography as well as the microstructure of the top layers of the sample surface. The goal was to detect precipitations of unalloyed elements or other impurities, which were not detected by XRD.

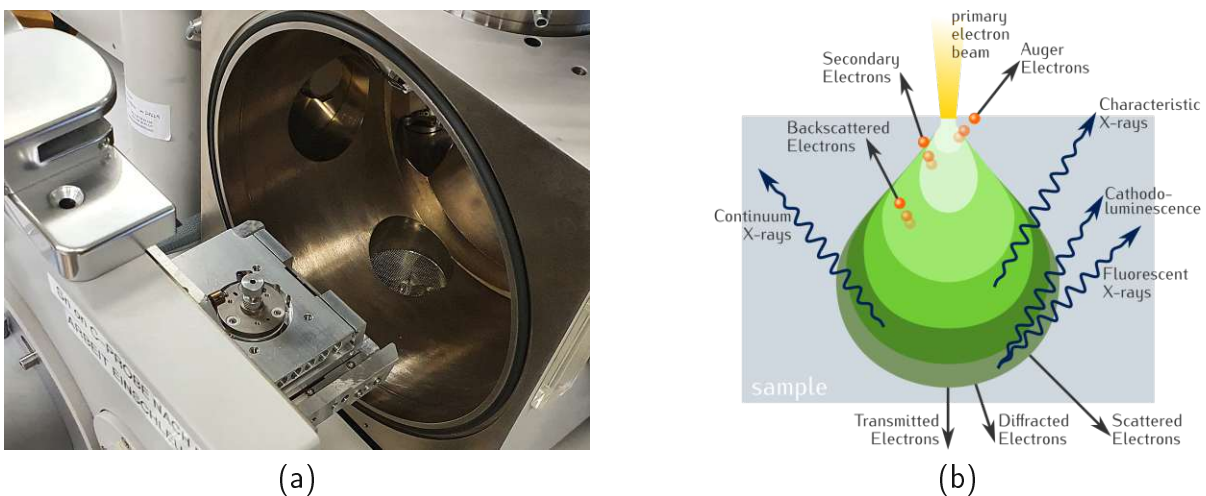


Figure 3.18: (a): FEI Quanta 250 FEG sample chamber. (b): Electron beam interaction with matter. Image from wikipedia [71]

## 4 Problem formulation and motivation

The properties of all Heusler alloys vary with heat treatment and composition. To enhance certain characteristics, doping can be used, replacing atoms at defined lattice sites. Pure  $\text{Fe}_2\text{VAl}$  has a very low power factor on its own, but looking at other studies and experiments, like for example F. Garmroudi's diploma thesis [57]:  $\text{Fe}_2\text{V}_{0.95}\text{Ta}_{0.05}\text{Al}_{0.9}\text{Si}_{0.1}$  had a power factor of  $8.4 \text{ mW m}^{-1} \text{ K}^2$ , up from about 0.1. Just as it is stated in the subsection "Thermoelectric effect" 2.5, each thermal electric property cannot be changed without affecting the other ones.

### 4.1 Effect of Ta-W co-substitution

Many researcher teams have already been using tantalum as a substitution element for vanadium in  $\text{Fe}_2\text{VAl}$  because it serves several purposes.  $\text{Fe}_2\text{VAl}$  has an indirect band gap, meaning that a phonon assisted transition from valence to conduction band is required. In contrast, calculations of  $\text{Fe}_2\text{TaAl}$  reveal a direct band gap at the  $X$  point in the first Brillouin zone. So, substituting tantalum at the vanadium site shifts the band structure from the tightest gap being at the  $X$  point in the first Brillouin zone to the  $\Gamma$  point, where the valence band reaches the highest energy.

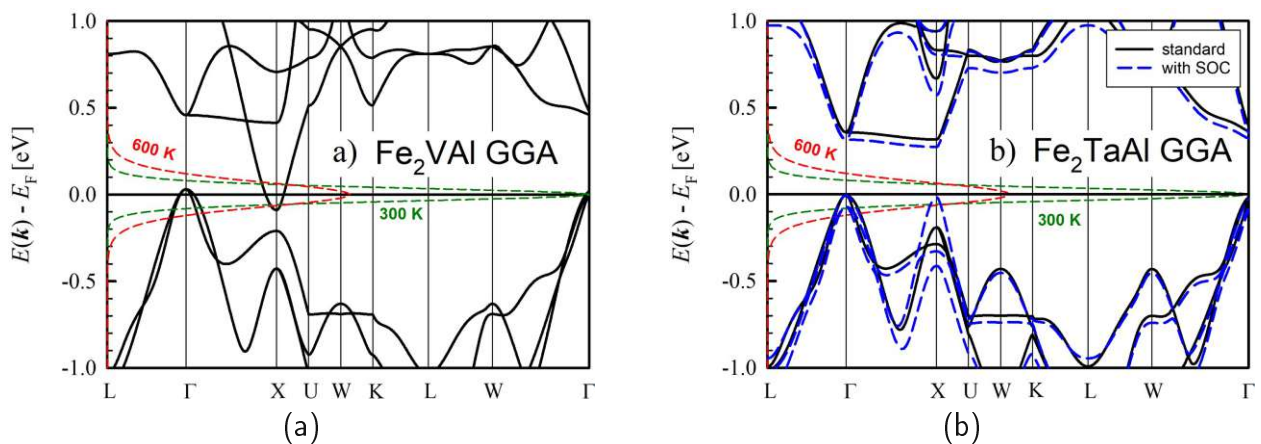


Figure 4.1: Calculated electronic band structures of (a)  $\text{Fe}_2\text{VAl}$  and (b)  $\text{Fe}_2\text{TaAl}$ . SOC = spin-orbit coupling. [72]

The other element we used for doping is tungsten. W and Ta are heavy metals, big atoms that strain the lattice, when being put onto the vanadium site. This should increase phonon scattering and therefore decrease the lattice thermal conductivity and so further increase the figure of merit. Tungsten also has one more electron in its outer shell compared to vanadium, so it also acts as an electron donor, which also can decrease electric resistivity by shifting the Fermi energy.

## 4.2 Problem of Solubility

After the melting process the alloys can be in a metastable state due to quenching in the water-cooled boat. Additionally, strains and stresses might be present. Annealing at appropriate temperatures should give the material enough time and energy to reach an equilibrium or stable state. Sometimes the alloy shows phase changes after annealing and traces of pure tungsten were found. In other samples less inhomogeneous zones were found, even though the samples were manufactured in the same manner with the same parameters. Figure 4.2 shows the solubility space observed as part of this thesis.

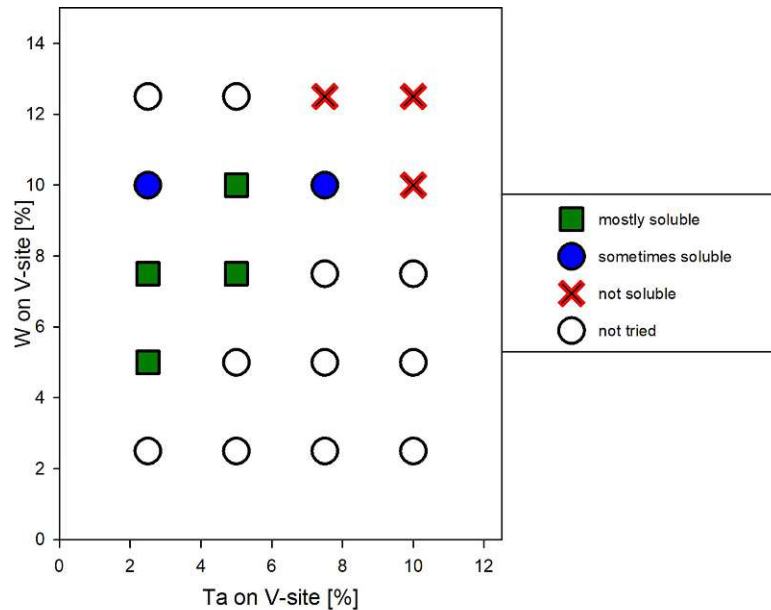


Figure 4.2: Observed solubility of tantalum and tungsten in  $\text{Fe}_2\text{VAl}$  after annealing.

Looking at Figure 4.2 the sample  $\text{Fe}_2\text{V}_{0.875}\text{Ta}_{0.025}\text{W}_{0.1}\text{Al}$  should have been stable too, but it wasn't. It is also very much possible, that annealing over 7 days at 1073 K was too short of a time frame and the sample  $\text{Fe}_2\text{V}_{0.85}\text{Ta}_{0.05}\text{W}_{0.1}\text{Al}$  might have shown different - more unstable - behaviour than discussed in the following chapters.

## 5 Results

The following sections summarise the results of experimental studies of this diploma thesis. Every samples' quality was first checked by eye for spots, where the elements did not mix properly. Samples featuring signs of demixing were discarded right away. This could have been because the temperature was not high enough during the melting process or because a miscibility gap was reached.

### 5.1 XRD analysis

X-ray diffraction (XRD) is a rather common practice to analyse crystalline materials. Depending on the angle of the incoming x-rays, the electromagnetic waves are diffracted by the bulk material. This way, diffraction pattern are obtained, which correlate with a specific crystal structure. At shallow angles, this method can also be used to obtain surface information.

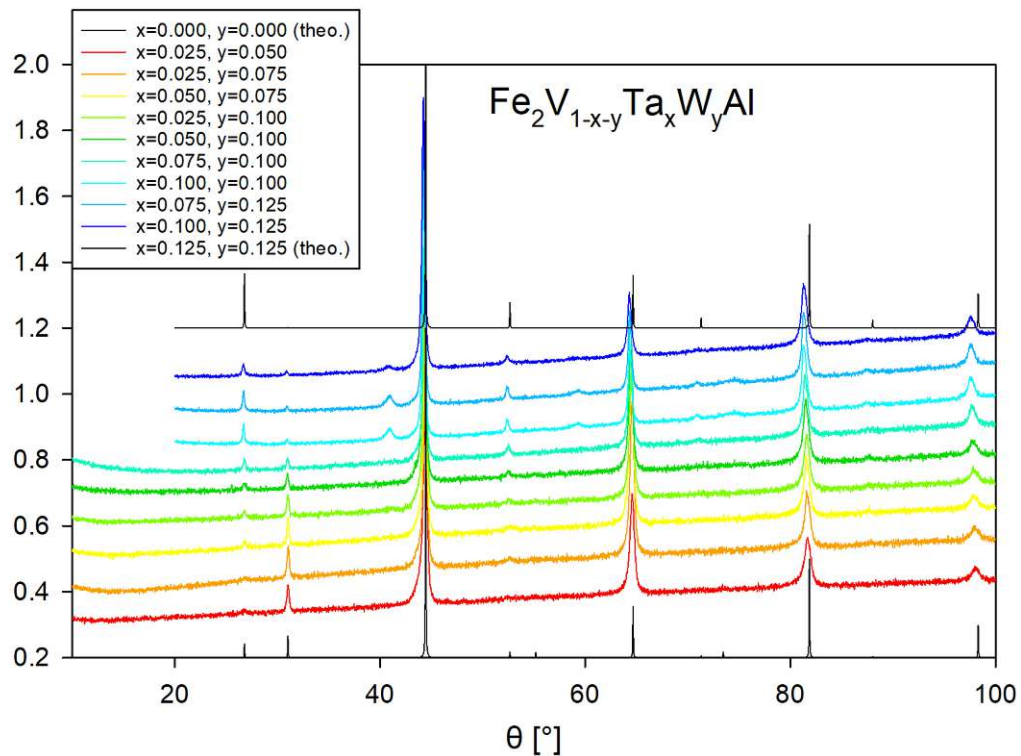


Figure 5.1: X-ray diffraction (XRD) pattern of 9 of the first 13 samples, arranged from lowest doped  $\text{Fe}_2\text{V}_{0.925}\text{Ta}_{0.025}\text{W}_{0.05}\text{Al}$  (red) to highest  $\text{Fe}_2\text{V}_{0.775}\text{Ta}_{0.1}\text{W}_{0.125}\text{Al}$  (dark blue). Simulated XRD patterns, here shown in black, with pure  $\text{Fe}_2\text{VAl}$  (below the red pattern) and  $\text{Fe}_2\text{V}_{0.75}\text{Ta}_{0.125}\text{W}_{0.125}\text{Al}$  (above the dark blue pattern) were added to compare the results with the theoretical expectations.

A simple comparison of x-ray data with model calculations employing the full-Heusler structure, already allows an assessment of the sample's quality. The model was created and simulated with the program PowderCell. Full-Heusler alloys crystallise in a face-centered cubic structure. The most significant peak can be seen at  $44.5^\circ$  (for  $\text{Cu} - K_\alpha$  radiation), which correlates to the (220) crystal plane. Due to the background shift the peaks at higher

angles look a bit off, but even the one at  $98.3^\circ$  should be fine. One notices the peak at  $31^\circ$  disappears with higher doping and another one is growing at about  $26.5^\circ$ . This phenomenon is expected and has been observed, when doping  $\text{Fe}_2\text{VAl}$  with heavy elements. There is also an emerging peak at  $52.6^\circ$  at the (311) plane which is normal. The peak at  $82^\circ$  should be twice as high as the one at  $64.5^\circ$  at low and high doping. This unexpected feature was probably introduced from grinding the sample into a powder for the XRD-analysis. As a result, grains might have preferred orientations. On the higher doped alloys there is a peak at  $41^\circ$  which is probably a Ta-rich Laves phase. Also the peak at  $26.8^\circ$  should be significantly higher.

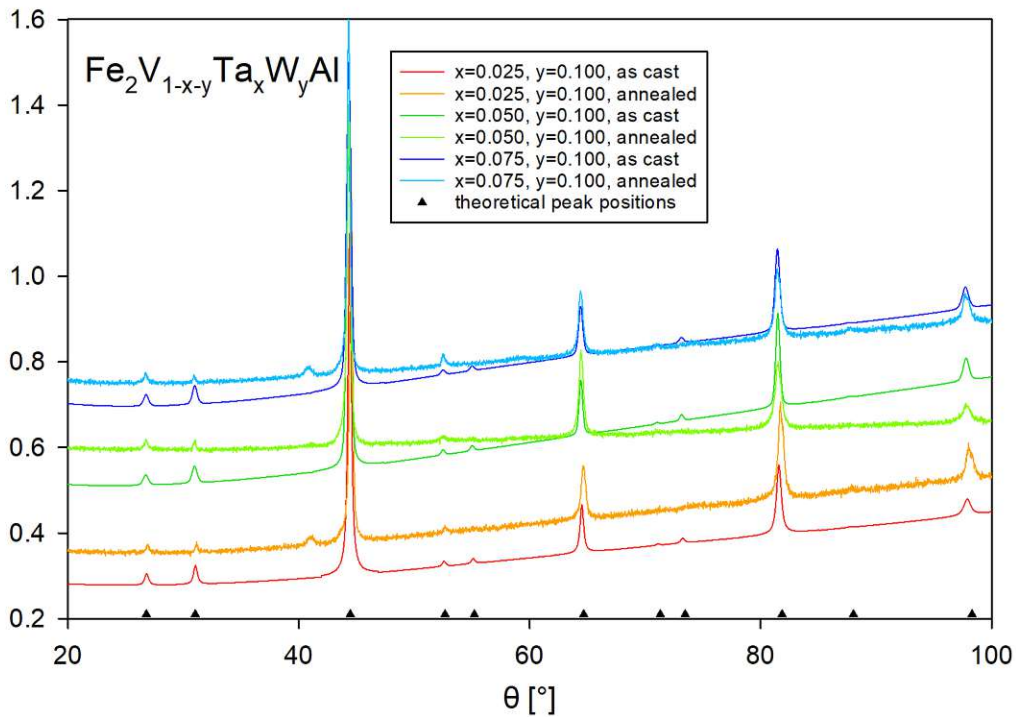


Figure 5.2: X-ray diffraction pattern of the 2nd batch of samples,  $\text{Fe}_2\text{V}_{0.875}\text{Ta}_{0.025}\text{W}_{0.1}\text{Al}$  (red),  $\text{Fe}_2\text{V}_{0.85}\text{Ta}_{0.05}\text{W}_{0.1}\text{Al}$  (green) and  $\text{Fe}_2\text{V}_{0.825}\text{Ta}_{0.075}\text{W}_{0.1}\text{Al}$  (blue), before (as cast) and after annealing (annealed). The theoretical peak positions are given with no intensity, since the intensity is varying strongly with doping concentration.

One also notices the  $41^\circ$  peaks, which have not been there before annealing on two of the samples. Interestingly enough all samples from 5 to 16 have been produced in the same exact way - Meaning same heating cycles during melting, same annealing time and temperature.

### 5.1.1 Lattice parameter

Table 5.1, Table 5.2 and Table 5.3 show, that the lattice parameters were not even 0.5% bigger than the pure  $\text{Fe}_2\text{VAl}$ . This was the case when measuring the samples straight after casting and after annealing using the XRD analysis tool “PANalytical Data Viewer”. A large deviation from the non-doped alloy was expected.

$Ta_x$ [%]	$W_y$ [%]	lattice parameter [Å]
2.5	5.0	5.769
2.5	7.5	5.775
5.0	7.5	5.778
2.5	10.0	5.777
5.0	10.0	5.781
7.5	10.0	5.791

Table 5.1: Lattice parameter of 1st batch  $Fe_2V_{1-x-y}Ta_xW_yAl$  samples with various  $x$  and  $y$  annealed at 800 °C for 168 hours.

$Ta_x$ [%]	$W_y$ [%]	lattice parameter [Å]
2.5	10.0	5.780
5.0	10.0	5.777
7.5	10.0	5.782

Table 5.2: Lattice parameter of 2nd batch  $Fe_2V_{0.9-x}Ta_xW_{0.1}Al$  samples with various  $x$  before annealing.

$Ta_x$ [%]	$W_y$ [%]	lattice parameter [Å]
2.5	10.0	5.778
5.0	10.0	5.773
7.5	10.0	5.785

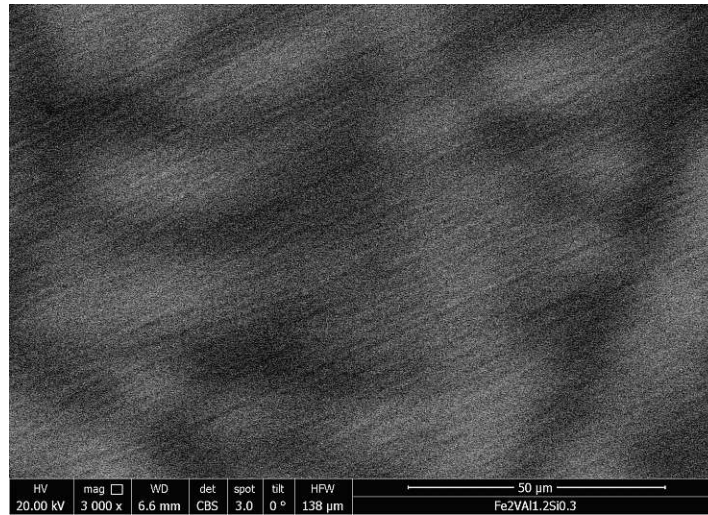
Table 5.3: Lattice parameter of 2nd batch  $Fe_2V_{0.9-x}Ta_xW_{0.1}Al$  samples with various  $x$  annealed at 800 °C for 168 hours.

## 5.2 Microstructure

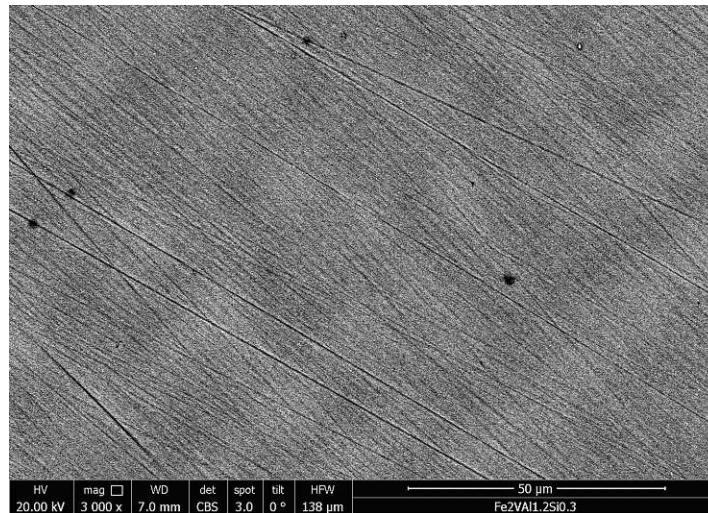
The SEM (scanning electron microscope) results will be presented in this section. Some randomly dispersed spots of high mass particle clusters were detected on the first few annealed higher doped samples. Heavier elements are usually brighter, when viewing the backscattered electrons in an electron microscope. The dark and light grooves, one can see in the SEM images in this section 5.2 (Figure 5.3, Figure 5.4, Figure 5.5, Figure 5.6, Figure 5.7, Figure 5.8, Figure 5.9), are marks from grinding and polishing the sample. Lighter spots are most likely clusters of unalloyed tungsten, while the darker background is dominated  $Fe_2VAl$ .

### 5.2.1 First batch

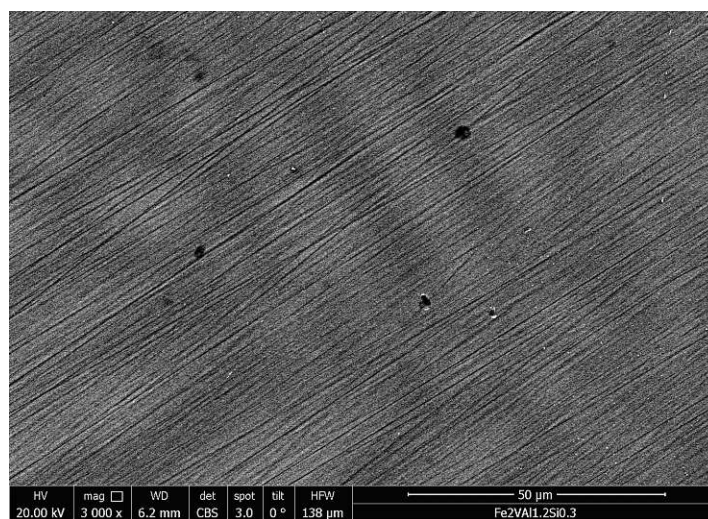
While the  $Fe_2V_{0.875}Ta_{0.025}W_{0.1}Al$  and  $Fe_2V_{0.85}Ta_{0.05}W_{0.1}Al$  samples were homogeneous, some brighter spots were visible on the  $Fe_2V_{0.825}Ta_{0.075}W_{0.1}Al$  sample.



(a)

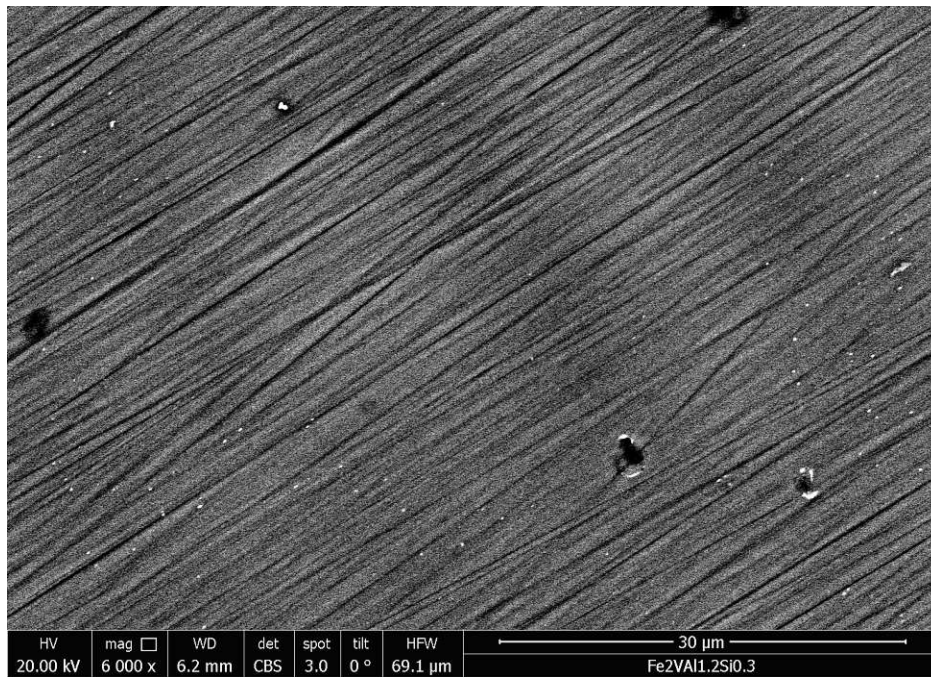


(b)

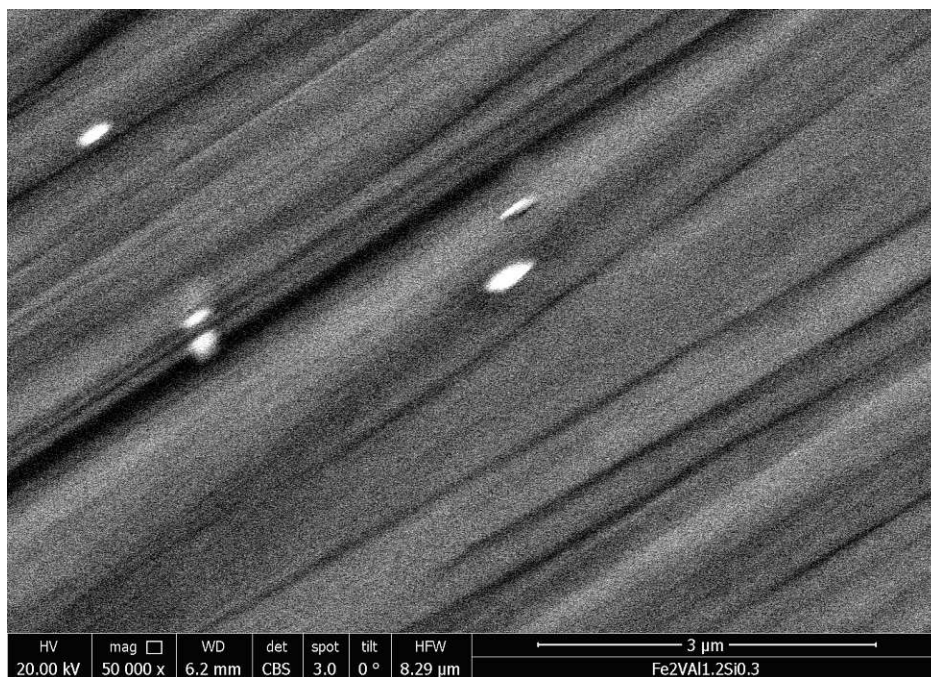


(c)

Figure 5.3: SEM images of the 1st batch of samples at 3000x magnification. (a):  $\text{Fe}_2\text{V}_{0.875}\text{Ta}_{0.025}\text{W}_{0.1}\text{Al}$ , (b):  $\text{Fe}_2\text{V}_{0.85}\text{Ta}_{0.05}\text{W}_{0.1}\text{Al}$ , (c):  $\text{Fe}_2\text{V}_{0.825}\text{Ta}_{0.075}\text{W}_{0.1}\text{Al}$



(a)

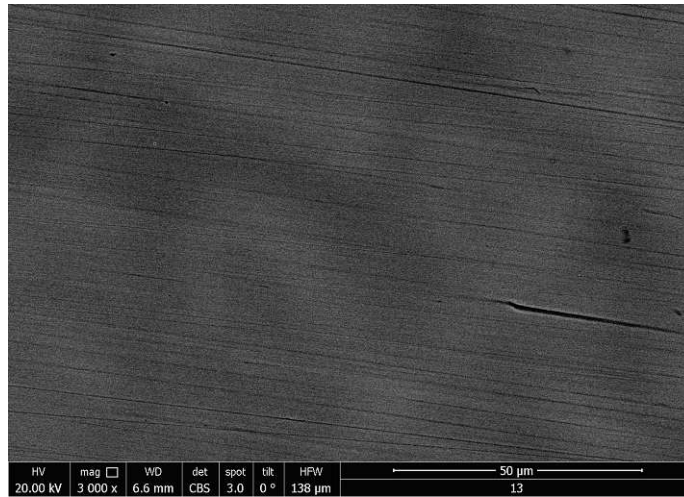


(b)

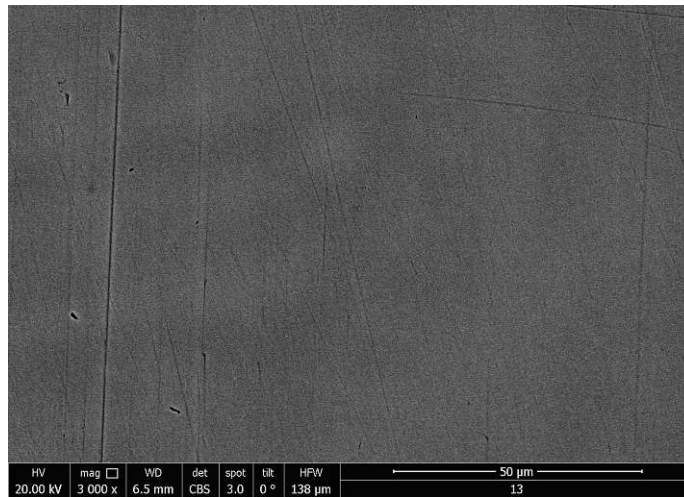
Figure 5.4: SEM image of the first  $\text{Fe}_2\text{V}_{0.825}\text{Ta}_{0.075}\text{W}_{0.1}\text{Al}$  sample at (a) 6000x and (b) 50000x magnification. The bright spots are most likely unalloyed tungsten.

### 5.2.2 Second batch

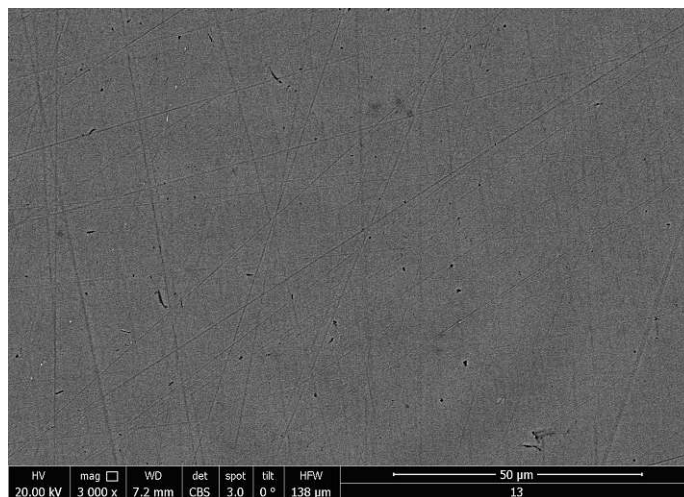
The next samples were not heat treated to observe the difference before, in [Figure 5.5](#) and [Figure 5.6](#), and after annealing, in [Figure 5.7](#) and [Figure 5.8](#).



(a)

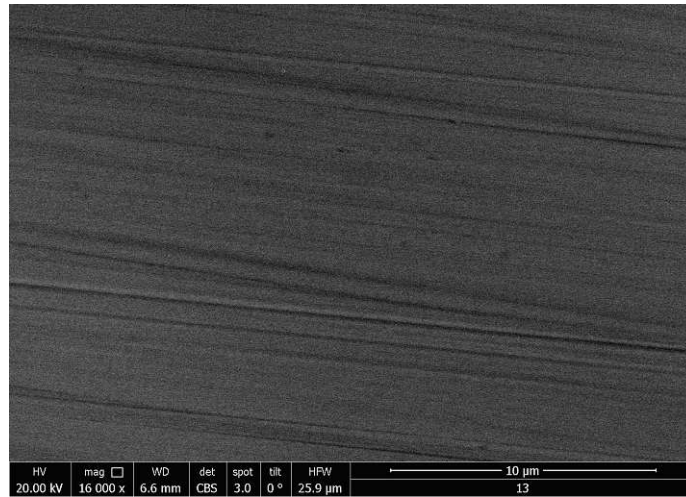


(b)

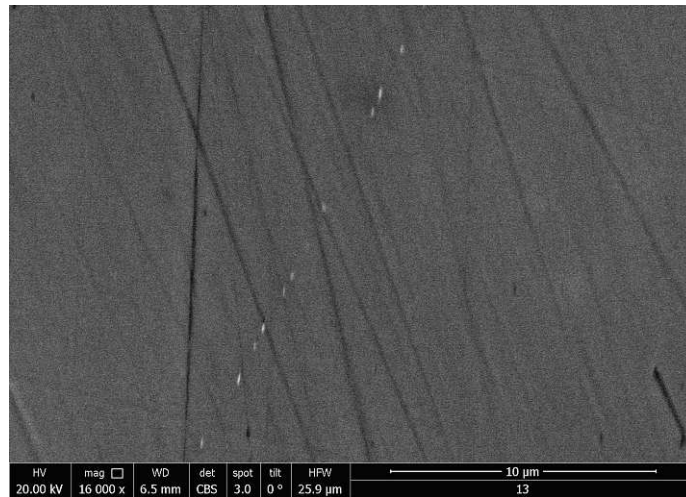


(c)

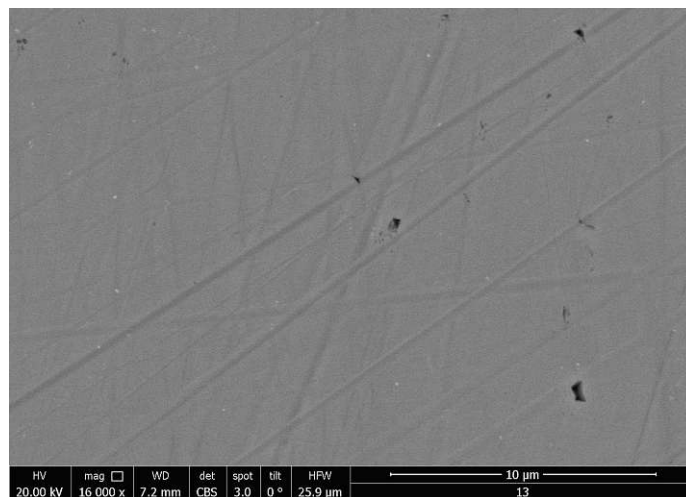
Figure 5.5: SEM images of samples before annealing at 3000x magnification.  
 (a):  $\text{Fe}_2\text{V}_{0.875}\text{Ta}_{0.025}\text{W}_{0.1}\text{Al}$ , (b):  $\text{Fe}_2\text{V}_{0.85}\text{Ta}_{0.05}\text{W}_{0.1}\text{Al}$ , (c):  $\text{Fe}_2\text{V}_{0.825}\text{Ta}_{0.075}\text{W}_{0.1}\text{Al}$



(a)



(b)



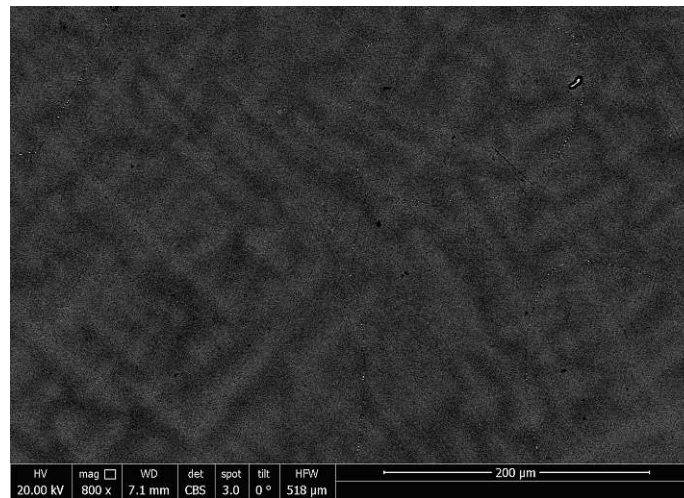
(c)

Figure 5.6: SEM images of samples before annealing at 16000x magnification.

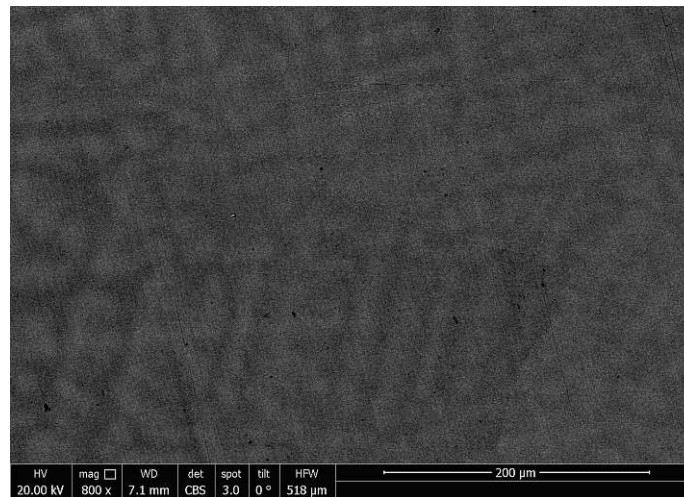
(a):  $\text{Fe}_2\text{V}_{0.875}\text{Ta}_{0.025}\text{W}_{0.1}\text{Al}$ , (b):  $\text{Fe}_2\text{V}_{0.85}\text{Ta}_{0.05}\text{W}_{0.1}\text{Al}$  as cast 16000x, (c):  $\text{Fe}_2\text{V}_{0.825}\text{Ta}_{0.075}\text{W}_{0.1}\text{Al}$

Second batch samples were examined with different contrast settings, so one can spot heavy elements in the grain boundaries at lower magnification after annealing, as demonstrated

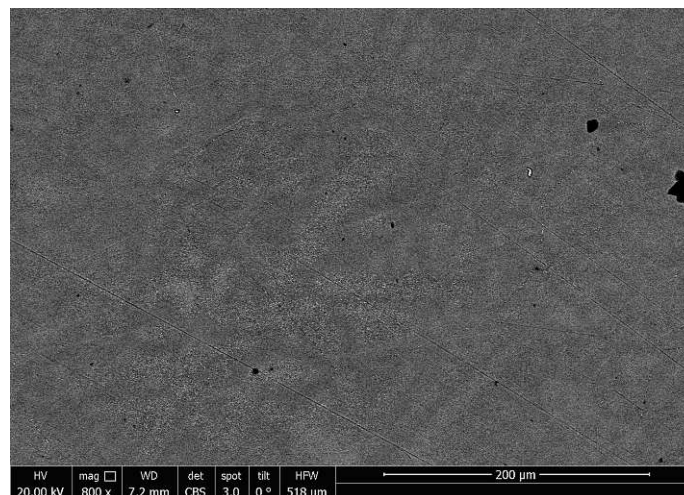
in Figure 5.7 and Figure 5.8. There are also more and bigger dark spots, which indicate different phases, with less ideal thermoelectric properties.



(a)

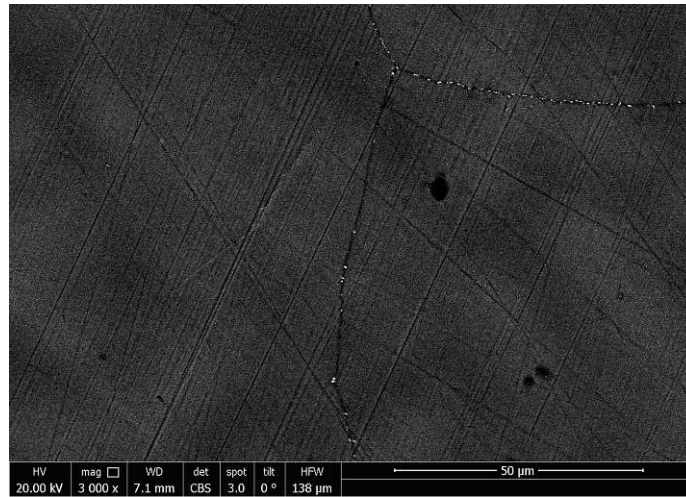


(b)

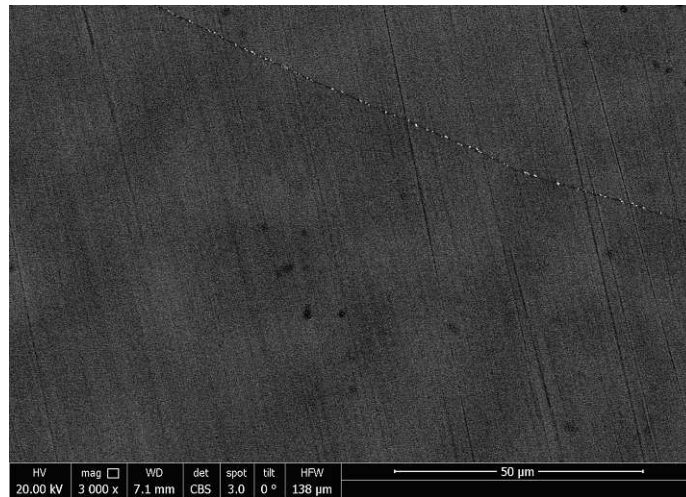


(c)

Figure 5.7: SEM images of samples after annealing at 800x magnification. (a):  $\text{Fe}_2\text{V}_{0.875}\text{Ta}_{0.025}\text{W}_{0.1}\text{Al}$ , (b):  $\text{Fe}_2\text{V}_{0.85}\text{Ta}_{0.05}\text{W}_{0.1}\text{Al}$ , (c):  $\text{Fe}_2\text{V}_{0.825}\text{Ta}_{0.075}\text{W}_{0.1}\text{Al}$



(a)



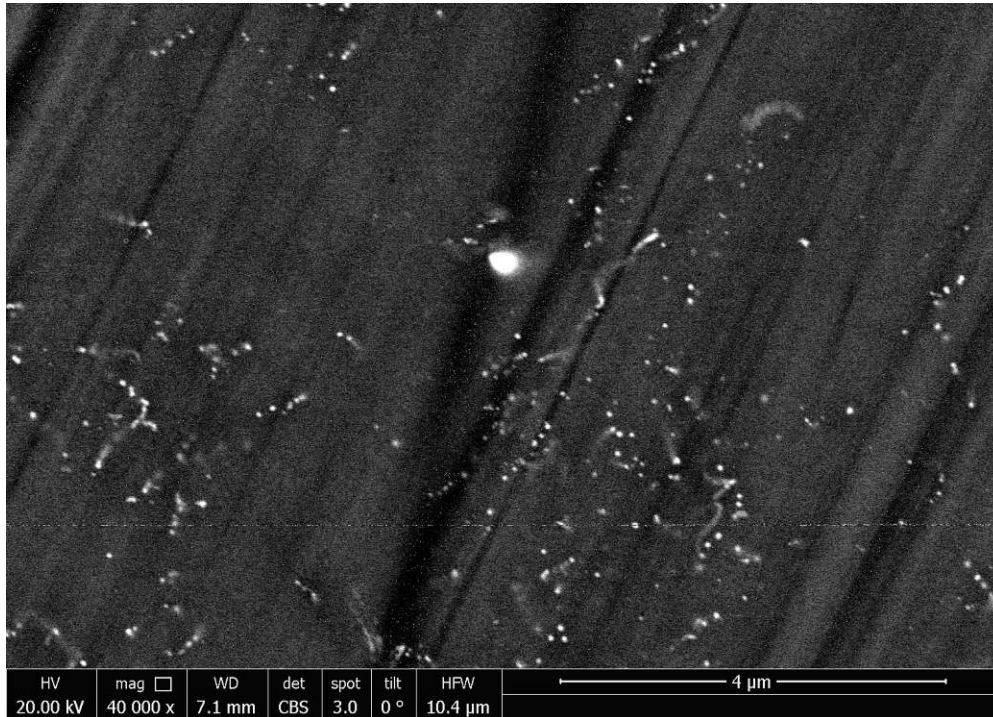
(b)



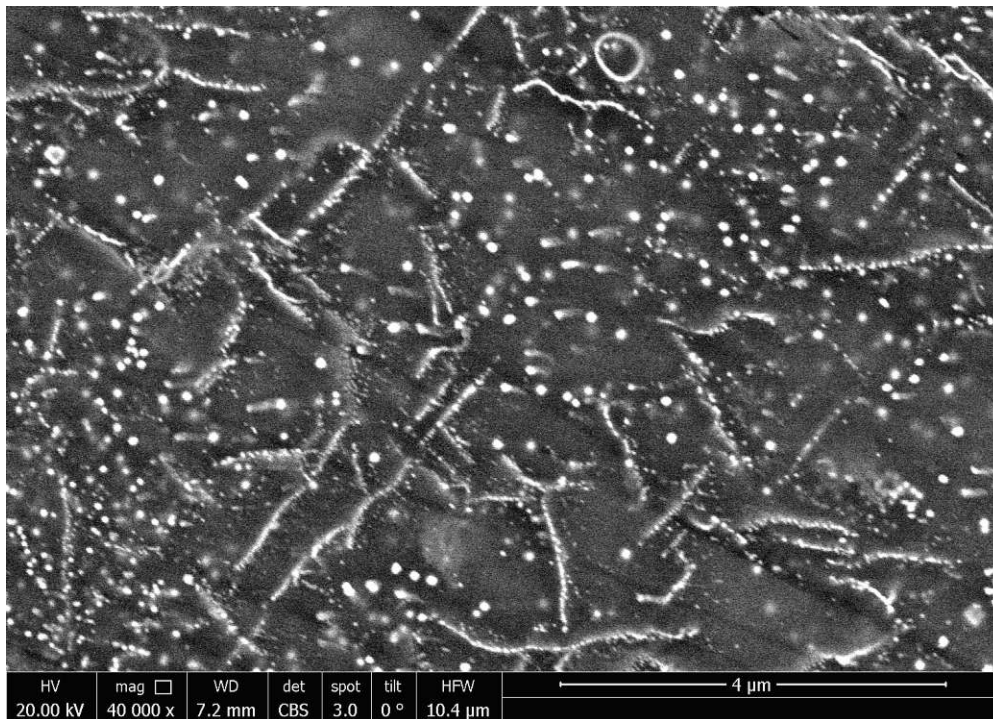
(c)

Figure 5.8: SEM images of samples after annealing at 3000x magnification.  
 (a):  $\text{Fe}_2\text{V}_{0.875}\text{Ta}_{0.025}\text{W}_{0.1}\text{Al}$ , (b):  $\text{Fe}_2\text{V}_{0.85}\text{Ta}_{0.05}\text{W}_{0.1}\text{Al}$ , (c):  $\text{Fe}_2\text{V}_{0.825}\text{Ta}_{0.075}\text{W}_{0.1}\text{Al}$

In Figure 5.8 one can easily spot something else in the image of  $\text{Fe}_2\text{V}_{0.825}\text{Ta}_{0.075}\text{W}_{0.1}\text{Al}$  (Figure 5.8c) at 3000 times magnification. An odd looking structure has formed. Zooming in closer (Figure 5.9) it also appears on the  $\text{Fe}_2\text{V}_{0.875}\text{Ta}_{0.025}\text{W}_{0.1}\text{Al}$  sample (Figure 5.8a). A local cluster of tungsten, which must have been overlooked, when examined before annealing.



(a)

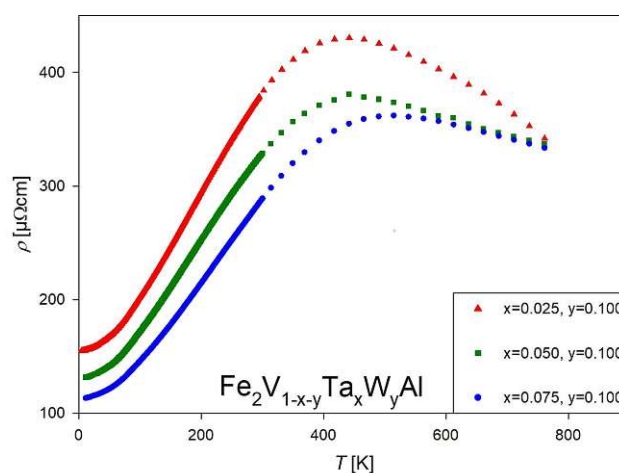


(b)

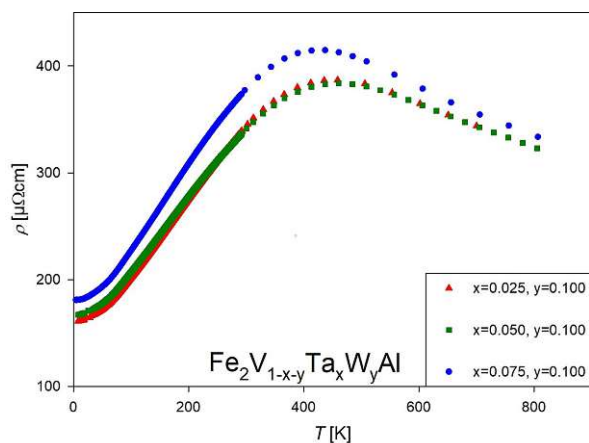
Figure 5.9: SEM images of second batch samples (a)  $\text{Fe}_2\text{V}_{0.875}\text{Ta}_{0.025}\text{W}_{0.1}\text{Al}$  and (b)  $\text{Fe}_2\text{V}_{0.825}\text{Ta}_{0.075}\text{W}_{0.1}\text{Al}$  sample at 40000x magnification showing a localized tungsten cluster.

## 5.3 Electrical resistivity

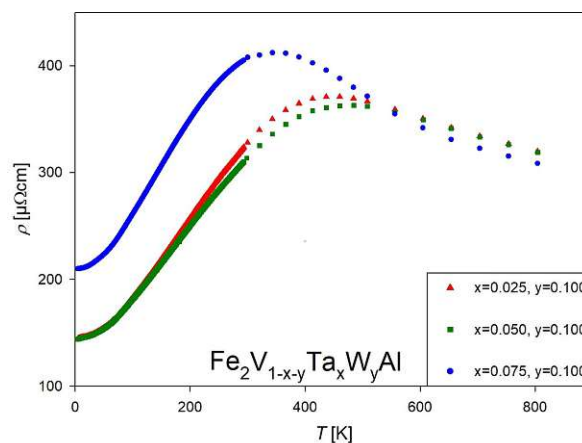
The temperature dependent electrical resistivity of  $\text{Fe}_2\text{V}_{0.9-x}\text{Ta}_x\text{W}_{0.1}\text{Al}$  is shown in Figure 5.10(a-c). Obviously, the overall behaviour results from a complicated overlay of metallic and semiconducting features. There is a maximum formed around 400 K. Below that the samples show metallic behaviour, the electrical resistivity rises with temperature, and above the maximum the resistivity falls, typical for a semiconductor. In Figure 5.10a, annealed samples with higher doping exhibit reduced electrical resistivity, since donor or acceptor elements introduce either added electrons or holes for enhanced conductivity. The following samples in Figure 5.10b, Figure 5.10c and Figure 5.11 are n-type doped, iso-electronically in relation to each other. So any difference should stem from the band gap widening effect of tantalum, as seen in Figure 4.1.



(a)



(b)

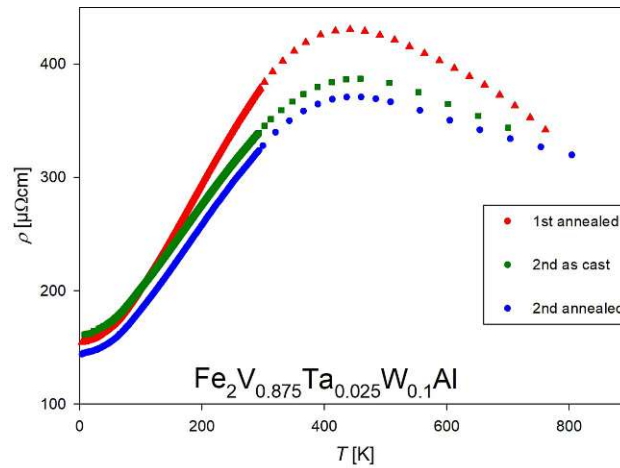


(c)

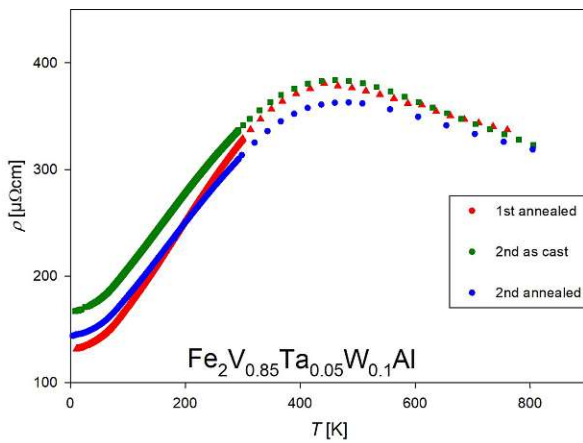
Figure 5.10: Comparing the (a) 1st batch (annealed), (b) 2nd batch “as cast” and (c) 2nd batch annealed samples regarding the temperature dependent electrical resistivity  $\rho$  of  $\text{Fe}_2\text{V}_{0.9-x}\text{Ta}_x\text{W}_{0.1}\text{Al}$  for various  $x$ .

The assumption of reduced resistivity with higher tantalum doping, observed in Figure 5.10a, does not hold true, when comparing the second batch (Figure 5.11c). The maximum shifting to higher temperatures with increased doping, seen in Figure 5.10a doesn't show up in the second sample set (Figure 5.10b & Figure 5.10c).

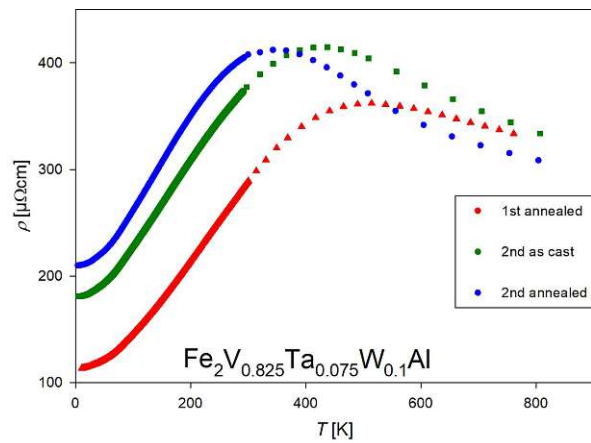
Only the resistivity of  $\text{Fe}_2\text{V}_{0.85}\text{Ta}_{0.05}\text{W}_{0.1}\text{Al}$  (Figure 5.11b) is matching with the sample from the previous batch. The highest doped sample confirms further changes throughout the sample during annealing, which was spotted under the microscope in the previous section 5.9. Its resistivity and following Seebeck coefficient (section 5.4) are definitely off from the expected values.



(a)



(b)



(c)

Figure 5.11: Comparing the temperature dependent electrical resistivity  $\rho$  of samples with the same stoichiometric composition.

(a):  $\text{Fe}_2\text{V}_{0.875}\text{Ta}_{0.025}\text{W}_{0.1}\text{Al}$ , (b):  $\text{Fe}_2\text{V}_{0.85}\text{Ta}_{0.05}\text{W}_{0.1}\text{Al}$ , (c):  $\text{Fe}_2\text{V}_{0.825}\text{Ta}_{0.075}\text{W}_{0.1}\text{Al}$

Shown in Figure 5.12, is a reduction of the electrical resistivity, as expected after annealing.

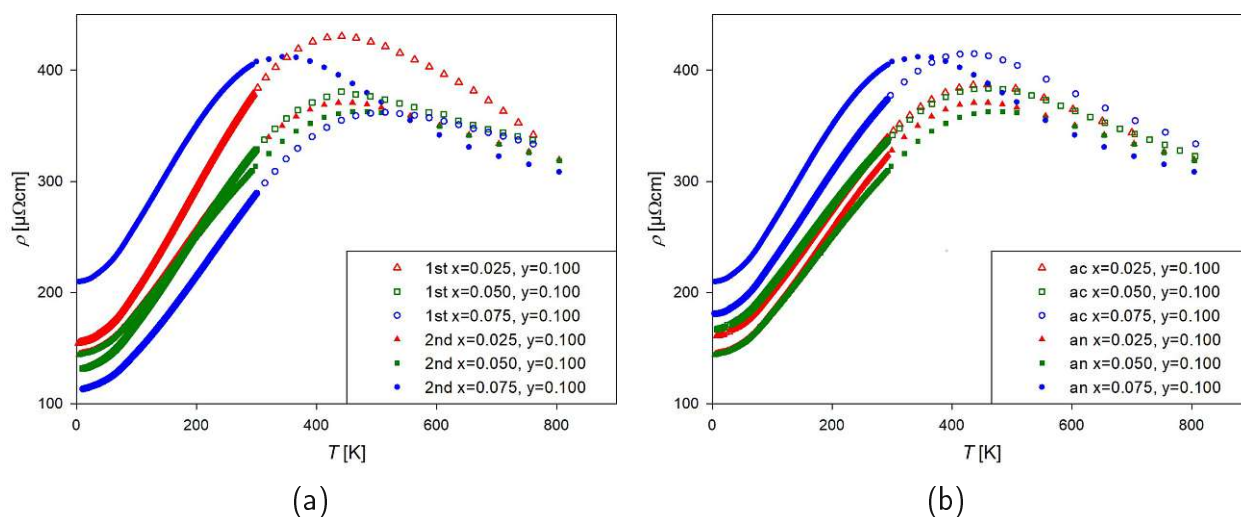


Figure 5.12: Comparison of the temperature dependent electrical resistivity  $\rho$  between (a) 1st and 2nd batch and (b) impact of annealing as seen in the 2nd batch.

Despite all the unexpected results, the electrical resistivity was lowered with annealing at least for the samples  $\text{Fe}_2\text{V}_{0.875}\text{Ta}_{0.025}\text{W}_{0.1}\text{Al}$  and  $\text{Fe}_2\text{V}_{0.85}\text{Ta}_{0.05}\text{W}_{0.1}\text{Al}$ , clearly shown by Figure 5.12b, which was expected.

For completion's sake, Figure 5.13 depicts some of the earliest samples, created to gauge the effectiveness of co-doping tantalum and tungsten. Those samples were not examined as closely, so it is possible that these samples also experienced changes through the crystal during annealing.

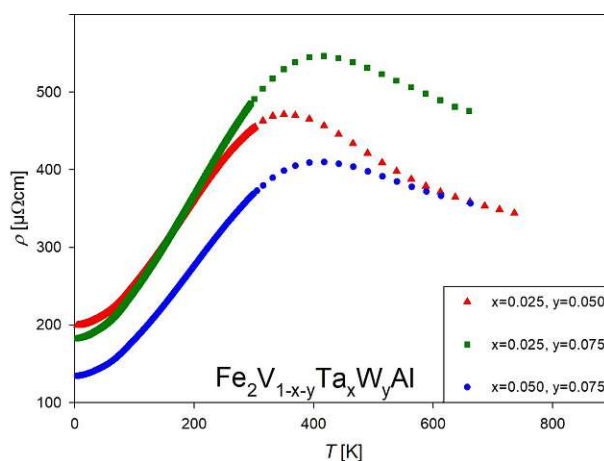


Figure 5.13: Temperature dependent electrical resistivity  $\rho$  of  $\text{Fe}_2\text{V}_{1-x-y}\text{Ta}_x\text{W}_y\text{Al}$  for various values of  $x$  and  $y$ .

## 5.4 Seebeck coefficient

Usually, the temperature dependent Seebeck coefficient of pure  $\text{Fe}_2\text{VAl}$  is positive up to 750 K, with a maximum of about  $65 \mu\text{V K}^{-1}$  around 200 K ([62]), but is shown to be negative when doped with tungsten. [44] In Figure 5.14, Figure 5.15 and Figure 5.17 the temperature dependent Seebeck coefficient of  $\text{Fe}_2\text{V}_{1-x-y}\text{Ta}_x\text{W}_y\text{Al}$  is summarised. Common to all the samples are large negative values and maxima around 300 K. Qualitatively, such scenarios follow from electrons as the most relevant charge carriers, as well as from charge carriers, which are thermally excited across the gap in the electronic density of states. The Seebeck coefficient is similar for all samples at higher temperatures, while solubility and stability had a notable impact, as seen in Figure 5.17. Low temperature Seebeck measurement were not done due to the large number of first batch samples (Figure 5.14a & Figure 5.15d). Seeing in how the second batch has turned out (Figure 5.14c), it would have been interesting to measure the more stable 1st batch samples with the same stoichiometric composition.

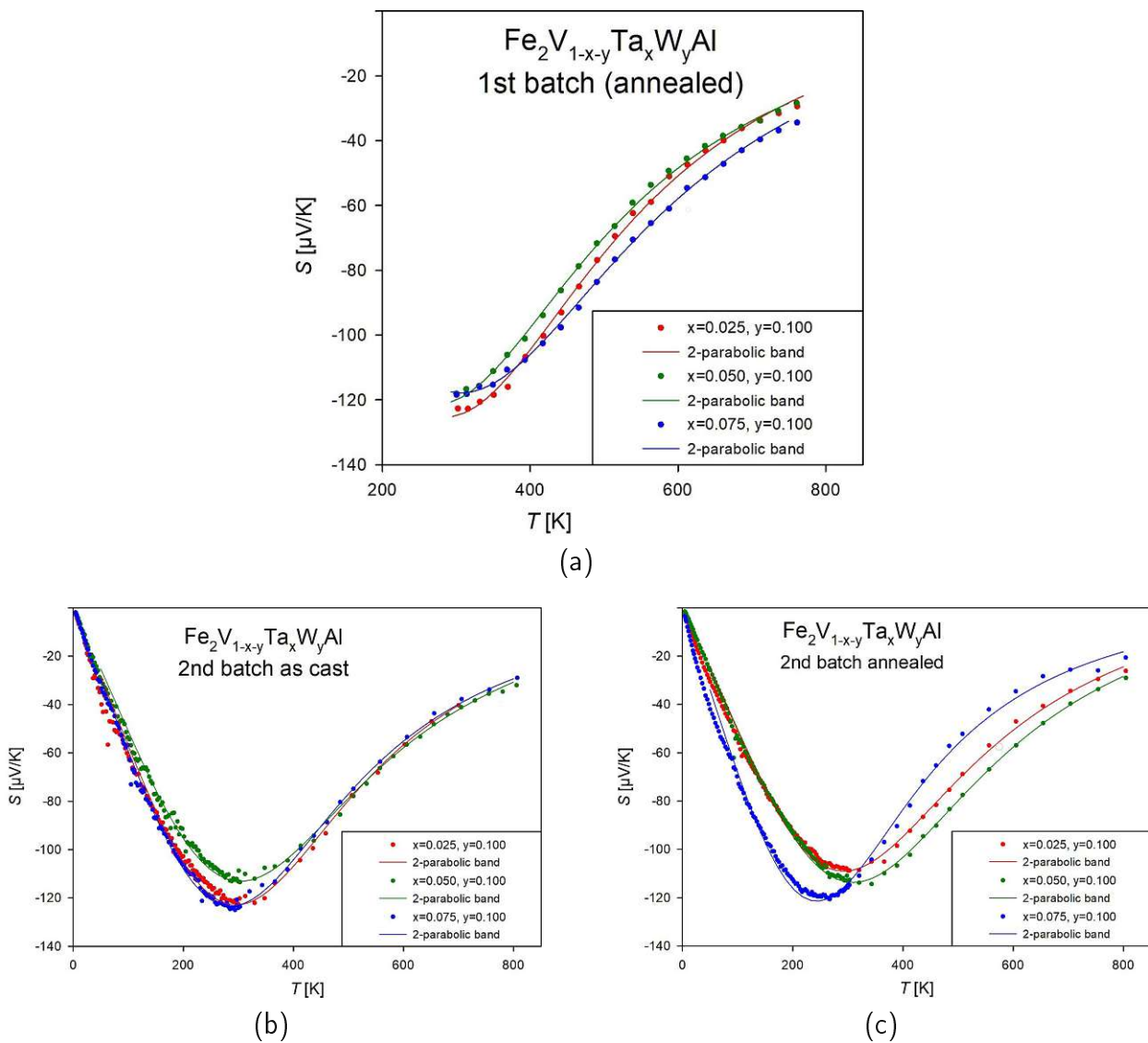


Figure 5.14: Comparison of the temperature dependent Seebeck coefficient  $S$  of (a) 1st and (b) 2nd batch samples as cast and (c) annealed. The solid lines are least squares fits employing the two-parabolic band model. Details are explained in the text.

The annealed  $\text{Fe}_2\text{V}_{0.825}\text{Ta}_{0.075}\text{W}_{0.1}\text{Al}$  sample (blue) from the 2nd batch (Figure 5.15c) is not showing the expected values, compared to the other samples, due to the formation of impurity phases.

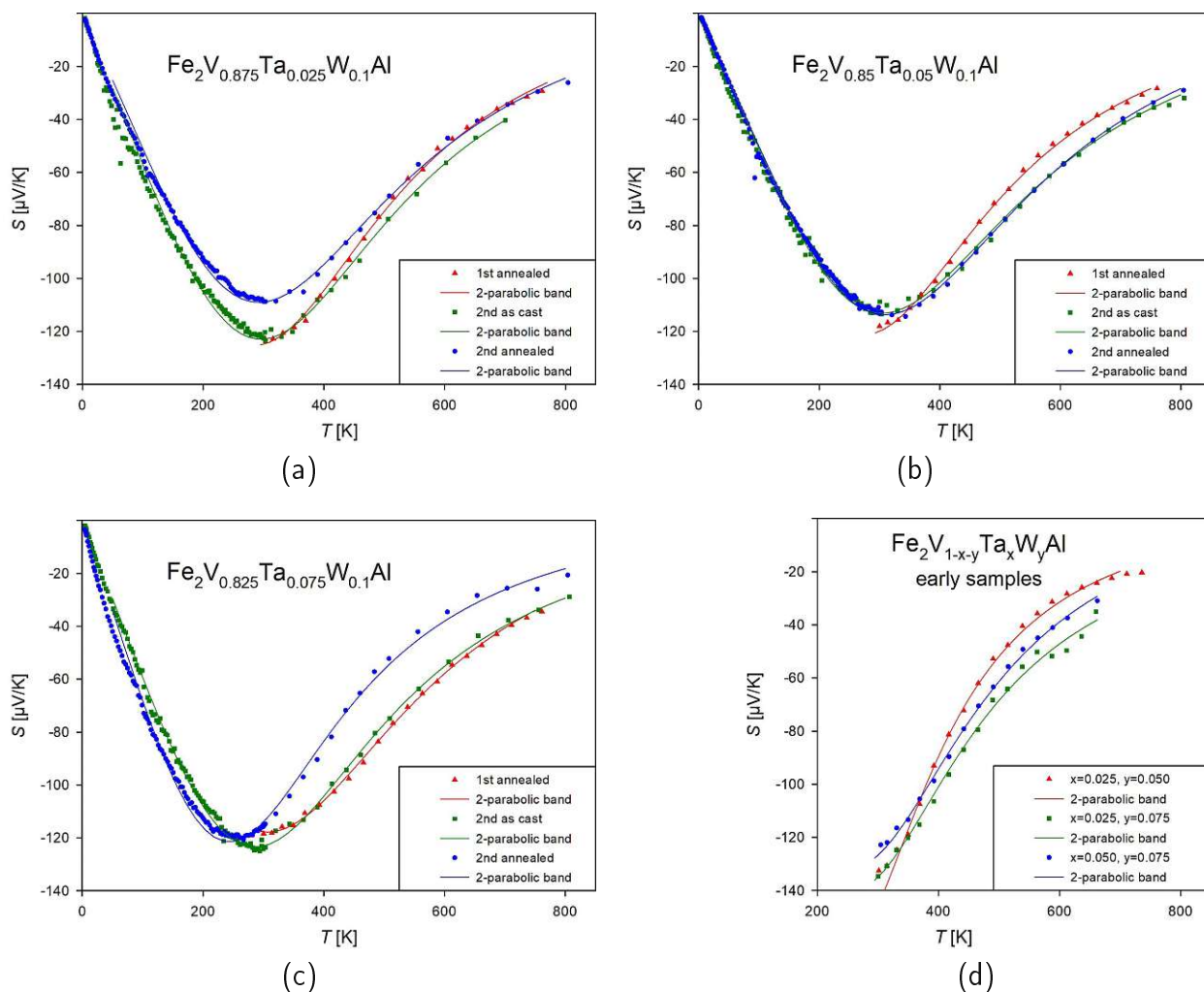


Figure 5.15: Comparison of the temperature dependent Seebeck coefficient  $S$  between (a)  $\text{Fe}_2\text{V}_{0.875}\text{Ta}_{0.025}\text{W}_{0.1}\text{Al}$ , (b)  $\text{Fe}_2\text{V}_{0.85}\text{Ta}_{0.05}\text{W}_{0.1}\text{Al}$ , (c)  $\text{Fe}_2\text{V}_{0.825}\text{Ta}_{0.075}\text{W}_{0.1}\text{Al}$  and (d) early samples. The solid lines are least squares fits employing the two-parabolic band model. Details are explained in the text.

The Goldsmid-Sharp formula Equation 5.1 [44] can be used to calculate the approximate band gap width  $E_{gap}$  in the density of states (DOS) of present materials. The extreme value of the temperature dependent Seebeck coefficient  $|S_{max}|$  and the temperature at that value  $T(S_{max})$  are required. The elemental charge  $e$  is a constant.

$$E_{gap} = 2 \cdot e \cdot |S_{max}| \cdot T(S_{max}) \quad (5.1)$$

As seen in section 2.4, the Seebeck coefficient  $S$  depends on the charge carrier density  $n$ , as well as their mobility. The temperature-dependent behavior of  $S$  can be simulated within a parabolic band model, where the relative effective mass, energy band gap and position of the chemical potential are the relevant parameters that determine the overall  $S(T)$  behavior. While in reality, band structures are usually complicated for most materials, near the band edges, the electron dispersion can be often well approximated as a parabola  $E \propto k^2$ . Since the

temperature-dependent Seebeck curves show distinct features arising from bipolar transport, we employed a two-parabolic band model (2PB) which was used to fit the data in a broad temperature range from 4 to 800 K. Least-squares fits are shown as solid lines in [Figure 5.14](#) & [Figure 5.15](#) and it can be seen that the rather simple 2PB model can accurately trace the temperature-dependent features of the experimental data in the whole temperature range.

$\text{Fe}_2\text{V}_{0.875}\text{Ta}_{0.025}\text{W}_{0.1}\text{Al}$	$S$ [ $\mu\text{V K}^{-1}$ ]	$T(S_{max})$ [K]	band gap width [meV]
2nd batch “as cast”	-123	302	74
2nd batch annealed	-109	295	64
$\text{Fe}_2\text{V}_{0.85}\text{Ta}_{0.05}\text{W}_{0.1}\text{Al}$	$S$ [ $\mu\text{V K}^{-1}$ ]	$T(S_{max})$ [K]	band gap width [meV]
2nd batch “as cast”	-113	310	70
2nd batch annealed	-114	310	71
$\text{Fe}_2\text{V}_{0.825}\text{Ta}_{0.075}\text{W}_{0.1}\text{Al}$	$S$ [ $\mu\text{V K}^{-1}$ ]	$T(S_{max})$ [K]	band gap width [meV]
2nd batch “as cast”	-123	280	69
2nd batch annealed	-121	249	60

Table 5.4: The calculated band gap width via Goldsmid-Sharp of 2nd batch samples  $\text{Fe}_2\text{V}_{0.9-x}\text{Ta}_x\text{W}_{0.1}\text{Al}$  for various  $x$  before and after annealing.

Results for the least square fits and then using Goldsmid-Sharp have been summarised in [Table 5.4](#). Similar results have been obtained from the application of the so called two-parabolic band model in [Table 5.5](#). Least square fits (solid lines in [Figure 5.14](#) and [Figure 5.15](#)) yield information about band gaps as well as about effective masses of the relevant charge carriers (see [Table 5.5](#)). The wider the temperature range of experimental data, the easier it is to fit the temperature dependent Seebeck coefficient with the two-parabolic band model.

$\text{Fe}_2\text{V}_{0.875}\text{Ta}_{0.025}\text{W}_{0.1}\text{Al}$	$\frac{m_{\text{conductionband}}}{m_{\text{valenceband}}}$ [ ]	band gap width [meV]	$E - E_{\text{valencebandmax}}$ [meV]
1st batch annealed	1.09	47	89
2nd batch “as cast”	1.07	46	89
2nd batch annealed	1.11	31	80
$\text{Fe}_2\text{V}_{0.85}\text{Ta}_{0.05}\text{W}_{0.1}\text{Al}$	$\frac{m_{\text{conductionband}}}{m_{\text{valenceband}}}$ [ ]	band gap width [meV]	$E - E_{\text{valencebandmax}}$ [meV]
1st batch annealed	1.07	41	82
2nd batch “as cast”	1.08	36	85
2nd batch annealed	1.11	39	88
$\text{Fe}_2\text{V}_{0.825}\text{Ta}_{0.075}\text{W}_{0.1}\text{Al}$	$\frac{m_{\text{conductionband}}}{m_{\text{valenceband}}}$ [ ]	band gap width [meV]	$E - E_{\text{valencebandmax}}$ [meV]
1st batch annealed	1.10	43	90
2nd batch “as cast”	1.05	44	86
2nd batch annealed	1.06	36	72

Table 5.5: The calculated band mass fraction, band gap width, and approximate Fermi energy via the two-parabolic band model fit of annealed 1st batch and 2nd batch samples  $\text{Fe}_2\text{V}_{0.9-x}\text{Ta}_x\text{W}_{0.1}\text{Al}$  for various  $x$  before and after annealing.

The two-parabolic band model reveals in [Table 5.5](#) that electrons of the conduction band are heavier than those of the valence band. The energy above the valence band  $E - E_{\text{valencebandmax}}$  is bigger than the band gap energy. This means, the Fermi energy is definitely in the conduction band. The reason for that are the additional electrons from tungsten. When calculating with the Goldsmid-Sharp formula ([Equation 5.1](#), [Table 5.4](#)), the expected band gap widening with increased tantalum was only observed in the 2nd batch annealed samples

$\text{Fe}_2\text{V}_{0.875}\text{Ta}_{0.025}\text{W}_{0.1}\text{Al}$  to  $\text{Fe}_2\text{V}_{0.85}\text{Ta}_{0.05}\text{W}_{0.1}\text{Al}$ . The band gap width also seems to be over-estimated. Calculating with the two-parabolic band model (Table 5.5), the results are also inconclusive. A band gap widening with increased tantalum concentration was observed for 1st batch and 2nd batch annealed  $\text{Fe}_2\text{V}_{0.85}\text{Ta}_{0.05}\text{W}_{0.1}\text{Al}$  to  $\text{Fe}_2\text{V}_{0.825}\text{Ta}_{0.075}\text{W}_{0.1}\text{Al}$  and 2nd batch “as cast”  $\text{Fe}_2\text{V}_{0.85}\text{Ta}_{0.05}\text{W}_{0.1}\text{Al}$  to  $\text{Fe}_2\text{V}_{0.825}\text{Ta}_{0.075}\text{W}_{0.1}\text{Al}$ .

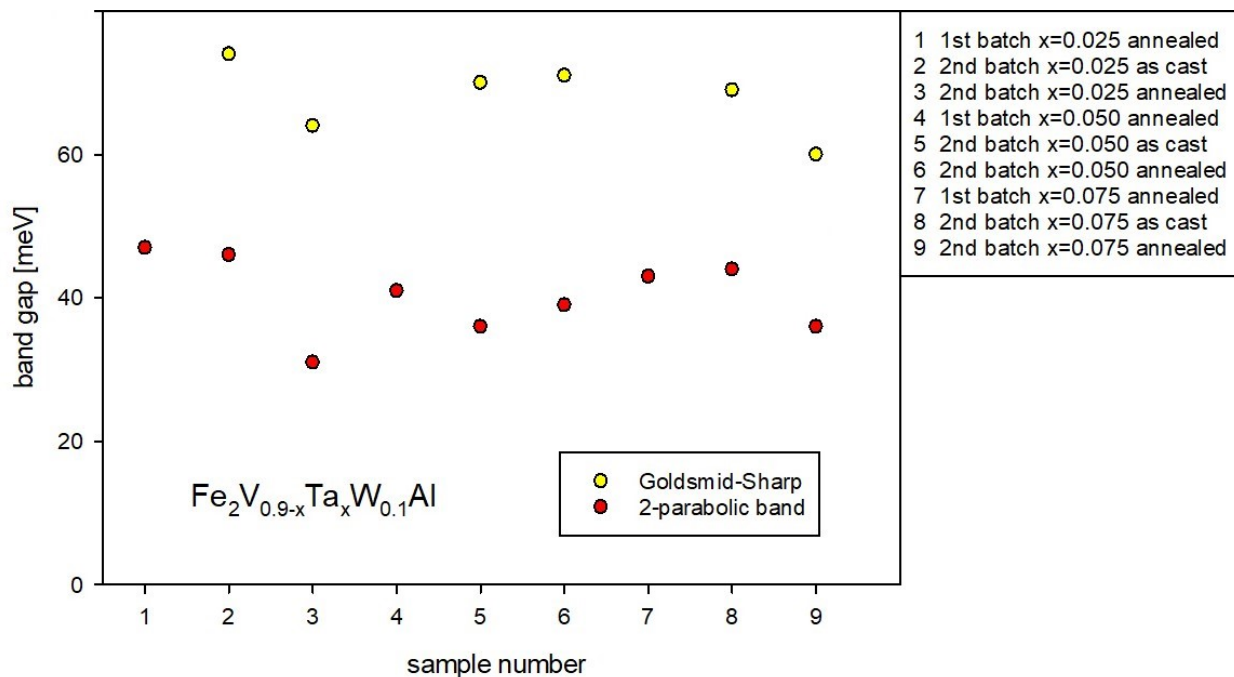


Figure 5.16: Band gap comparison of the Goldsmid-Sharp and the two-parabolic band model with samples of  $\text{Fe}_2\text{V}_{0.9-x}\text{Ta}_x\text{W}_{0.1}\text{Al}$  for various  $x$ , “as cast” and annealed.

The charge carrier density  $n$  can be calculated from the low-temperature dependent Seebeck coefficient using a formula for metals with a parabolic band [64], then rearrange to get

$$n = \frac{\left(\frac{\pi^2 \cdot k_B^2 \cdot 2 \cdot m_{\text{electron}}}{\epsilon \cdot \hbar^2 \cdot \frac{dS}{dT}}\right)^{3/2}}{3 \cdot \pi^2 \cdot 10^{-3}}. \quad (5.2)$$

For this, a tangent was created to the low-temperature Seebeck measurement between 4.5 K and 45 K. The slope of the tangent is  $\frac{dS}{dT}$ , the gradient of the temperature dependent Seebeck coefficient at the chosen temperature range. In Equation 5.2 the mass of the charge carrier is assumed to be the free electron mass.

2nd batch sample	charge carrier density [ $\text{cm}^{-3}$ ]
$\text{Fe}_2\text{V}_{0.875}\text{Ta}_{0.025}\text{W}_{0.1}\text{Al}$ “as cast”	$1.4 \cdot 10^{20}$
$\text{Fe}_2\text{V}_{0.875}\text{Ta}_{0.025}\text{W}_{0.1}\text{Al}$ annealed	$1.8 \cdot 10^{20}$
$\text{Fe}_2\text{V}_{0.85}\text{Ta}_{0.05}\text{W}_{0.1}\text{Al}$ “as cast”	$1.9 \cdot 10^{20}$
$\text{Fe}_2\text{V}_{0.85}\text{Ta}_{0.05}\text{W}_{0.1}\text{Al}$ annealed	$2.3 \cdot 10^{20}$
$\text{Fe}_2\text{V}_{0.825}\text{Ta}_{0.075}\text{W}_{0.1}\text{Al}$ “as cast”	$1.6 \cdot 10^{20}$
$\text{Fe}_2\text{V}_{0.825}\text{Ta}_{0.075}\text{W}_{0.1}\text{Al}$ annealed	$1.1 \cdot 10^{20}$

Table 5.6: The charge carrier density of the 2nd batch samples using low-temperature dependent Seebeck coefficient fits and Equation 5.2

As seen in Table 5.6,  $\text{Fe}_2\text{V}_{0.85}\text{Ta}_{0.05}\text{W}_{0.1}\text{Al}$  has the highest charge carrier density of the second batch samples, before and after annealing. Annealing increases the charge carrier density of the samples but  $\text{Fe}_2\text{V}_{0.825}\text{Ta}_{0.075}\text{W}_{0.1}\text{Al}$ , which not only has a lower charge carrier density than  $\text{Fe}_2\text{V}_{0.85}\text{Ta}_{0.05}\text{W}_{0.1}\text{Al}$  “as cast”, but also a reduced charge carrier density after annealing.

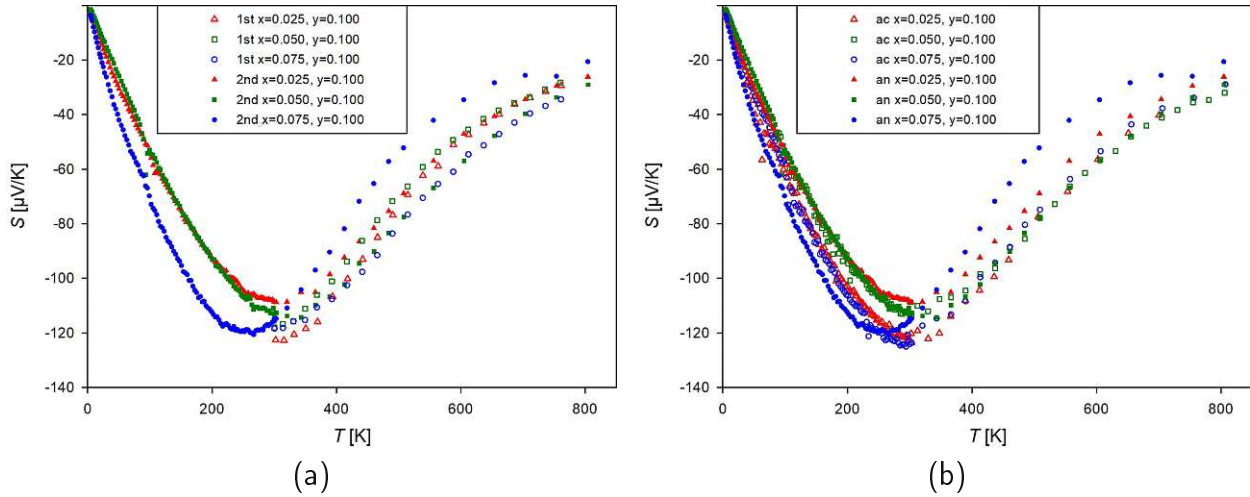


Figure 5.17: Comparison of the temperature dependent Seebeck coefficient  $S$  between (a) 1st and 2nd batch samples and (b) impact of annealing as seen in the 2nd batch.

Figure 5.17a shows that the first batch’s temperature dependent Seebeck coefficient had the higher absolute value. Interestingly enough, the second batch of samples had similar values before annealing, when comparing with Figure 5.17b.

## 5.5 Thermal conductivity

The low-temperature data was measured directly (section 3.6) and the high-temperature measurements were done with the flash method (section 3.7). The first batch of samples was not big enough to fit into the LFA-500<sup>TM</sup> (Figure 3.16). The second batch of samples was measured right after melting (Figure 5.20a) and then again after one week of annealing (Figure 5.20b). The following figures Figure 5.18, Figure 5.19 and Figure 5.20 show the temperature dependent thermal conductivity  $\kappa$  of 1st batch samples after annealing and 2nd batch samples before and after annealing. The thermal conductivity of Fe<sub>2</sub>VAl has a huge increase from about 4 K to 50 K with a maximum of about 45 W m<sup>-1</sup> K. Then it slopes off to about 25 W m<sup>-1</sup> K at room temperature. [44] As shown in Figure 5.19, the thermal conductivity of all the the measured samples (Fe<sub>2</sub>V<sub>1-x-y</sub>Ta<sub>x</sub>W<sub>y</sub>Al for varying  $x$  and  $y$ ) rises not as sharply, not even reaching 10 W m<sup>-1</sup> K, and then remain constant over a temperature of 100 K to room temperature. At temperatures above 300 K the thermal conductivity rises almost linearly with temperature. The exception here is Fe<sub>2</sub>V<sub>0.875</sub>Ta<sub>0.025</sub>W<sub>0.1</sub>Al, which behaves more like a root function, as seen in Figure 5.20. Due to contact and calibration errors all values of the following measurements can deviate from accurate figures. The graphs in Figure 5.18 shows the measured thermal conductivity  $\kappa_{measured}$  of the annealed 1st batch Fe<sub>2</sub>V<sub>0.875</sub>Ta<sub>0.025</sub>W<sub>0.1</sub>Al sample. Its constituents are determined with further calculations. Knowing the thermal conductivity and the electrical resistivity, the electronic part  $\kappa_{el}$  can be calculated using the Wiedemann-Franz law  $\kappa_{el} \cdot \rho = L \cdot T$  and subtracted to obtain the lattice contribution  $\kappa_{ph}$ .

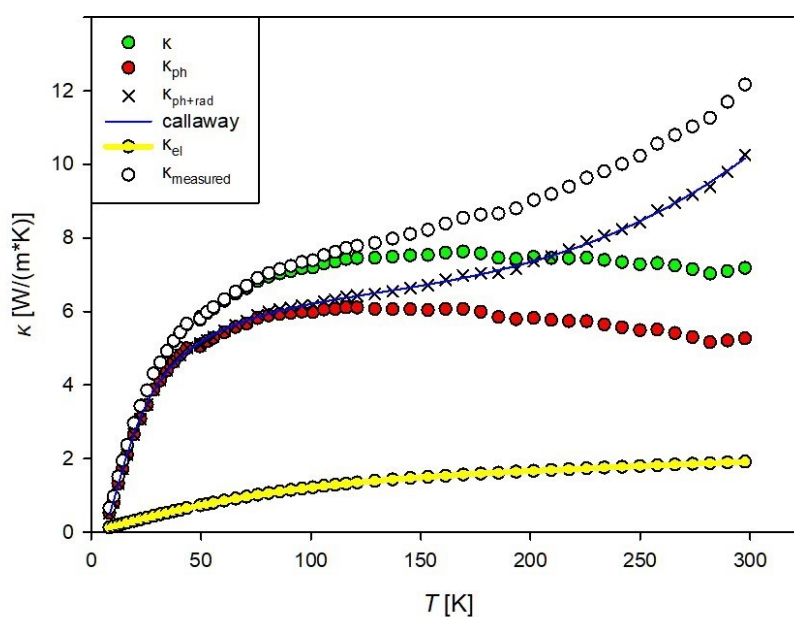


Figure 5.18: Temperature dependent thermal conductivity  $\kappa$  of Fe<sub>2</sub>V<sub>0.875</sub>Ta<sub>0.025</sub>W<sub>0.1</sub>Al.  $\kappa_{el}$  (yellow line) was calculated in terms of the Wiedemann-Franz law using the temperature dependent resistivity  $\rho$  of the sample.  $\kappa_{ph+rad}$  (X) is the phonon contribution. The radiation term was isolated via a  $T^3$  term added to the Callaway model. Details are explained in the text.

The Callaway model was employed to analyze the temperature dependent lattice thermal conductivity. Here, the specific heat is calculated within Debye's model and different phonon scattering mechanisms, each have their own frequency dependence and are accounted for via Mathiessen's rule.

$$\kappa_{ph+rad} = \frac{k_B}{2\pi \cdot v_S} \left( \frac{k_B \cdot T}{\hbar} \right)^3 \int_0^{\frac{T_D}{T}} \frac{\tau \cdot y^4 \cdot e^y}{(e^y - 1)^2} dy + f \cdot T^3 \quad (5.3)$$

$v_S$  is the average sound velocity of the material,  $T_D$  is the Debye temperature and  $y = \frac{\hbar \cdot \omega}{k_B \cdot T}$ . Additionally a  $f \cdot T^3$  term is added as correction due to radiation losses at high temperatures. The rest of the fit parameters, found in Equation 5.4 and Table 5.7, of the Callaway formula derive the scattering rate of the different mechanisms, point defect scattering, Umklapp scattering, interface scattering, phonon-electron scattering and the Debye temperature  $T_D$ :

$$\frac{1}{\tau_{point}} = a \cdot y^4 \cdot T^4 \quad (5.4)$$

$$\frac{1}{\tau_{umklapp}} = b \cdot y^2 \cdot T^3 \cdot e^{-\frac{T_D}{3 \cdot T}} \quad (5.5)$$

$$\frac{1}{\tau_{boundary}} = c \quad (5.6)$$

$$\frac{1}{\tau_{electron}} = d \cdot y \cdot T \quad (5.7)$$

$$\frac{1}{\tau_{total}} = \sum_i \tau_i \quad (5.8)$$

Other than easily obtaining a range of point defects, one could calculate an average grain size  $A$  with  $\frac{1}{\tau_{boundary}} \approx \frac{v_S}{A}$ .

1st batch sample	$a$ [ $s^{-1}K^{-4}$ ]	$b$ [ $s^{-1}K^{-3}$ ]	$c$ [ $s^{-1}$ ]
$Fe_2V_{0.875}Ta_{0.05}W_{0.075}Al$	111	$20.6 \cdot 10^3$	$38.8 \cdot 10^8$
$Fe_2V_{0.875}Ta_{0.025}W_{0.1}Al$	35.4	$0.329 \cdot 10^3$	$6.20 \cdot 10^8$
$Fe_2V_{0.85}Ta_{0.05}W_{0.1}Al$	47.5	$1.51 \cdot 10^3$	$10.9 \cdot 10^8$
$Fe_2V_{0.825}Ta_{0.075}W_{0.1}Al$	33.8	$0.093 \cdot 10^3$	$5.54 \cdot 10^8$
1st batch sample	$d$ [ $s^{-1}K^{-1}$ ]	$T_D$ [K]	$f$ [ $Wm^{-1}K^{-4}$ ]
$Fe_2V_{0.875}Ta_{0.05}W_{0.075}Al$	$-8.78 \cdot 10^7$	$2.98 \cdot 10^3$	$5.54 \cdot 10^{-7}$
$Fe_2V_{0.875}Ta_{0.025}W_{0.1}Al$	$-1.45 \cdot 10^7$	$1.03 \cdot 10^3$	$1.89 \cdot 10^{-7}$
$Fe_2V_{0.85}Ta_{0.05}W_{0.1}Al$	$-2.61 \cdot 10^7$	$1.14 \cdot 10^3$	$2.90 \cdot 10^{-7}$
$Fe_2V_{0.825}Ta_{0.075}W_{0.1}Al$	$-1.38 \cdot 10^7$	$0.26 \cdot 10^3$	$0.95 \cdot 10^{-7}$

Table 5.7: Parameter values were obtained via Callaway fit with “TableCurve 2D v5.01”. Parameters for point defect scattering  $a$ , Umklapp scattering  $b$ , interface scattering  $c$  and scattering rate with electrons  $d$ . There is the Debye temperature  $T_D$  and the thermal radiation parameter  $f$ . The complete function for the Callaway model can be found in appendix of J. W. Rehak’s diploma thesis. [46]

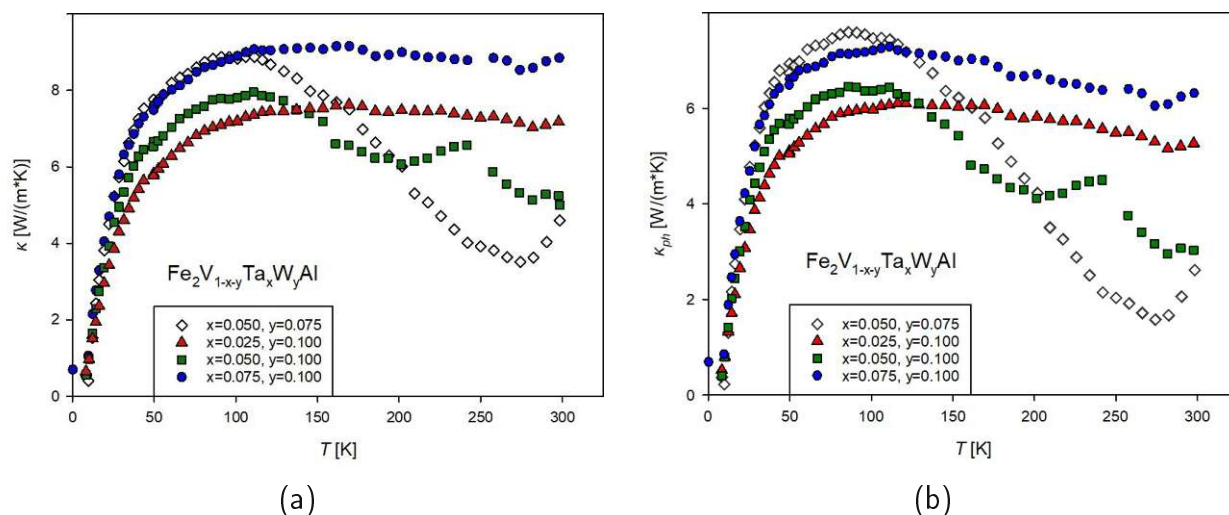


Figure 5.19: (a) Temperature dependent thermal conductivity  $\kappa = \kappa_{el} + \kappa_{ph}$ , and (b) temperature dependent lattice thermal conductivity  $\kappa_{ph}$  of  $\text{Fe}_2\text{V}_{1-x-y}\text{Ta}_x\text{W}_y\text{Al}$  for various values of  $x$  and  $y$  for temperatures below 300 K.

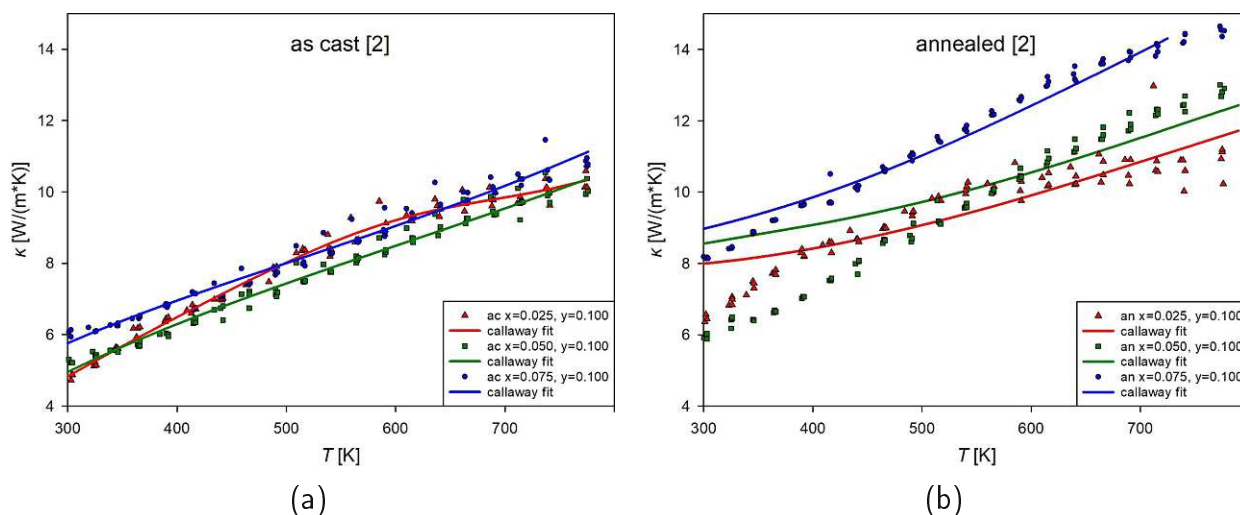


Figure 5.20: Comparing high-temperature dependent thermal conductivity  $\kappa$  of the 2nd sample batch (a) as cast and (b) annealed. Callaway fits (solid lines) were used to visualise the trend of the data.

The Callaway fits in Figure 5.20a behaves differently than in Figure 5.20b, since there wasn't any usable low-temperature data to use as baseline to continue from 300 K. One can see the impact that annealing has on the thermal conductivity out of all the examined properties. There is a noticeable increase in temperature dependent thermal conductivity at high temperatures after the annealing process, since the heat treatment decreases strain and disorder, and removes, at least partly, impurities and inhomogeneities.

## 5.6 Power factor

Figure 5.21 compares the power factor  $PF = \frac{S^2}{\rho}$  of the samples with the same stoichiometric composition. The first samples  $\text{Fe}_2\text{V}_{0.85}\text{Ta}_{0.05}\text{W}_{0.1}\text{Al}$  (green) and  $\text{Fe}_2\text{V}_{0.825}\text{Ta}_{0.075}\text{W}_{0.1}\text{Al}$  (blue) showed very promising results, as seen in Figure 5.21a. This prompted the exploration of higher doping concentrations, as well as interest in the impact of annealing. Both graphs of Figure 5.21 show that both of those samples from the 2nd batch with the same stoichiometric composition have a lower power factor at room temperature, before and after annealing. The second  $\text{Fe}_2\text{V}_{0.875}\text{Ta}_{0.025}\text{W}_{0.1}\text{Al}$  (red filled) sample had a higher power factor than the one from the first batch (red empty) (Figure 5.21a), which had an even higher power factor before annealing (Figure 5.21b). Samples with the same stoichiometric composition, which have been made under very similar (if not identical) conditions, exhibit very different power factors.

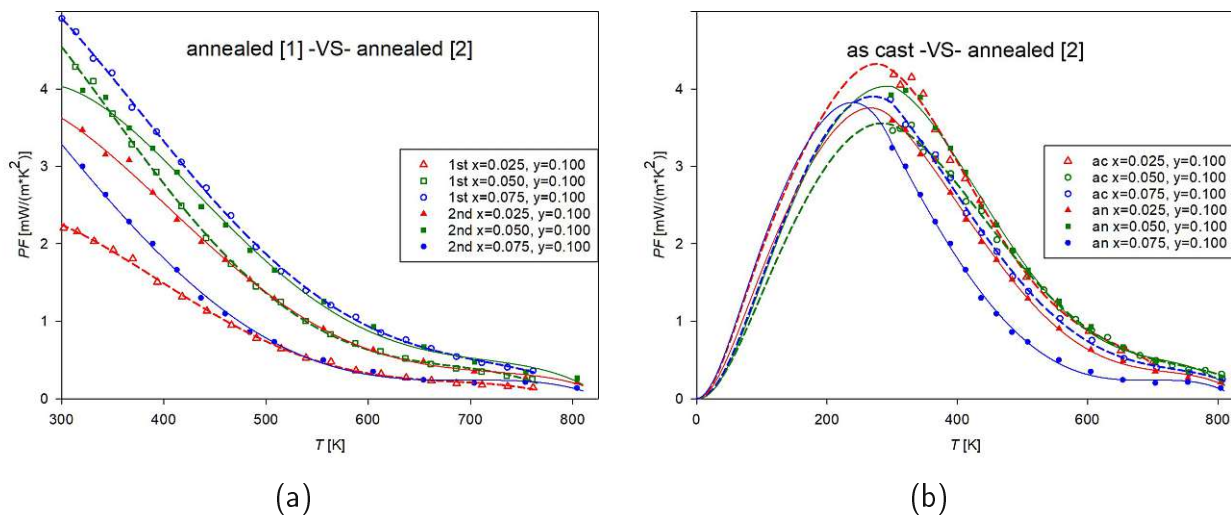


Figure 5.21: Comparison of the temperature dependent power factor  $PF$  between batches and impact of annealing of  $\text{Fe}_2\text{V}_{0.9-x}\text{Ta}_x\text{W}_{0.1}\text{Al}$  for various  $x$  of the (a) 1st and 2nd sample batch and (b) the 2nd batch as cast and annealed. Polynomial fits were used to visualise the power factor trend in Figure 5.21a (dashed line for 1st batch samples and solid lines for 2nd batch samples). Partially existing low-temperature data were used to create a trendline in Figure 5.21b (dashed line for “as cast” samples, and solid lines for annealed samples) as a visual aid.

One would suspect the maximum of the temperature dependent power factor to be slightly below room temperature. Since one could observe lots of local spots of unalloyed tungsten in Figure 5.9b, it is not a surprise, that the second batch  $\text{Fe}_2\text{V}_{0.825}\text{Ta}_{0.075}\text{W}_{0.1}\text{Al}$  sample after annealing shows the lowest power factor at room temperature, compared to the other samples. Its possible maximum is also shifted more towards 200 K. The  $\text{Fe}_2\text{V}_{0.875}\text{Ta}_{0.025}\text{W}_{0.1}\text{Al}$  “as cast” sample (red empty) had the highest power factor of the second batch at room temperature, and probably the highest maximum, too.

## 5.7 Figure of Merit

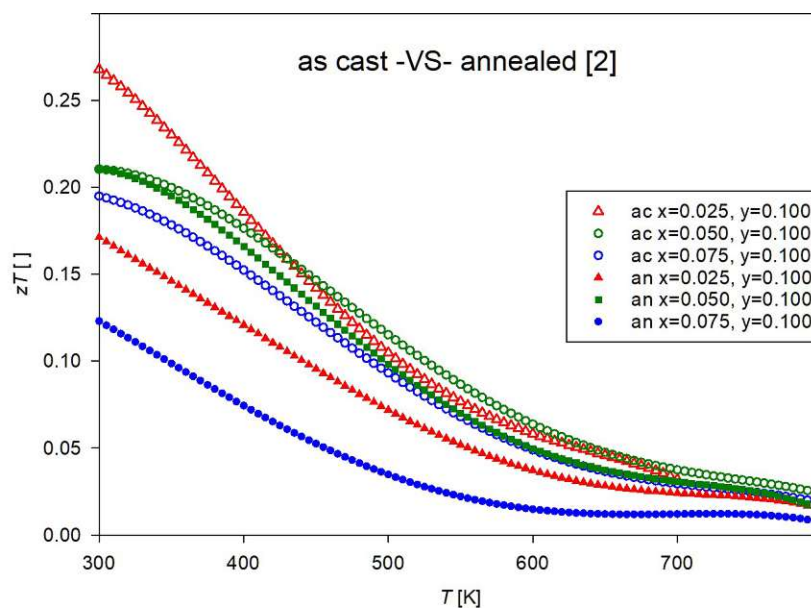


Figure 5.22: Comparing the temperature dependent figure of merit  $zT$  of “as cast” (empty) and annealed (filled) samples of  $\text{Fe}_2\text{V}_{0.9-x}\text{Ta}_x\text{W}_{0.1}\text{Al}$  for various  $x$  between 300 K to roughly 800 K.

One definitely notices the volatility of the samples in Figure 5.22. One would have expected  $zT$  to increase after annealing, but this wasn't the case. Tungsten precipitated, other phases formed after annealing and the figure of merit was reduced. Only the  $\text{Fe}_2\text{V}_{0.85}\text{Ta}_{0.05}\text{W}_{0.1}\text{Al}$  sample was stable during annealing. Like in the section before (section 5.6), the  $\text{Fe}_2\text{V}_{0.875}\text{Ta}_{0.025}\text{W}_{0.1}\text{Al}$  “as cast” sample had the highest figure of merit at room temperature and its maximum hasn't even been reached. Due to the lack of data, because of the sample geometry, the figure of merit of the first batch samples couldn't be calculated.



## 6 Conclusion

### 6.1 Discussion

The goal of this work was to improve the thermoelectric properties of  $\text{Fe}_2\text{VAl}$  by substituting vanadium with tungsten and tantalum. The results of the first samples looked promising, but then the second batch of samples, however, has not met the expectations. Tantalum substitution does decrease thermal conductivity and tungsten decreases electrical resistivity drastically. But consistency is the problem of  $\text{Fe}_2\text{V}_{1-x-y}\text{Ta}_x\text{W}_y\text{Al}$  samples at higher doping concentration above 12%. Miniscule, unnoticeable changes during synthesis, like heating or cooling times during the melting process, seem to have a huge impact on the final product. The seemingly random results stem from the volatile nature of the samples. Annealing the samples leads to precipitation of tungsten in the grain boundaries and can even be found finely dispersed inside the grains. Nevertheless one can use the findings and compare them to results from other research studies such as “Thermoelectric properties of tungsten-substituted Heusler  $\text{Fe}_2\text{VAl}$  alloy” [43] or “Stoichiometric and off-stoichiometric full Heusler  $\text{Fe}_2\text{V}_{1-x}\text{W}_x\text{Al}$  thermoelectric systems” [44]. Tantalum at 5% seems to move the maximum of  $zT$  to room temperature, when compared to only tungsten doped  $\text{Fe}_2\text{VAl}$ . But the slope of the graph at 400 K seems to be the same.

### 6.2 Outlook into the future

This work shows, co-substituting with 2 heavy elements on one lattice site at high concentrations might not lead to the desired results for  $\text{Fe}_2\text{VAl}$ . For that reason  $\text{Fe}_2\text{V}_{1-2x}\text{Ta}_x\text{W}_x\text{Al}_{1-y}\text{Si}_y$  with  $x=0.05$  as well as  $\text{Fe}_2\text{V}_{1-2x}\text{Ti}_x\text{W}_x\text{Al}_{1-y}\text{Si}_y$  are already being explored. Thermal conductivity and solubility are the two problems that haven't been solved simultaneously. Co-doping with chromium and molybdenum needs to be explored, too. High-pressure torsion employed to these samples can have a positive effect on the thermoelectric performance.



# List of Figures

1.1	zT of commonly used materials. . . . .	2
1.2	NaSi example for Zintl. . . . .	5
1.3	Fe <sub>2</sub> VAl unit cell. . . . .	7
2.1	Energy band and derivation. . . . .	10
2.2	Improvements with doping Fe <sub>2</sub> VAl. . . . .	20
3.1	Cutting and weighing of base materials. . . . .	21
3.2	Look into the induction melting tube. . . . .	22
3.3	Sample in quartz glass. . . . .	23
3.4	Cutting process and final sample piece. . . . .	24
3.5	Bragg's law. . . . .	25
3.6	Sample ULVAC-Riko ZEM-3. . . . .	26
3.7	Puck layout for low-temperature electrical resistivity measurement. . . . .	26
3.8	Low-T ele.res stick in cryo. . . . .	27
3.9	Sample preparation for Low-T Seebeck measurement. . . . .	28
3.10	Shielding of the sample and setup for Low-T Seebeck measurement. . . . .	29
3.11	Low-T thermal conductivity principle of measurement. . . . .	30
3.12	Low-T thermal conductivity vacuum. . . . .	30
3.13	Shielding of the sample and setup for Low-T thermal conductivity measurement. . . . .	31
3.14	Specific heat sample holder. . . . .	32
3.15	Different density measurements. . . . .	32
3.16	Linseis LFA 500 <sup>TM</sup> - Light Flash Analyzer . . . . .	33
3.17	Sample sanding and polishing for SEM. . . . .	34
3.18	FEI Quanta 250 FEG Sample chamber and electron interaction. . . . .	34
4.1	Calculated Fe <sub>2</sub> VAl & Fe <sub>2</sub> TaAl band structure . . . . .	35
4.2	Solubility of Ta and W . . . . .	36
5.1	XRD of 9 samples. . . . .	37
5.2	XRD of samples 14, 15 and 16. . . . .	38
5.3	First annealed samples at 3000 times magnification under SEM. . . . .	40
5.4	First Fe <sub>2</sub> V <sub>0.825</sub> Ta <sub>0.075</sub> W <sub>0.1</sub> Al sample at 6000x and 50000x magnification. . . . .	41
5.5	Samples before annealing under SEM. 3000x . . . . .	42
5.6	Samples before annealing under SEM. 16000x . . . . .	43
5.7	Samples after annealing under SEM. 800x . . . . .	44
5.8	Samples after annealing under SEM. 3000x . . . . .	45
5.9	Second Fe <sub>2</sub> V <sub>0.875</sub> Ta <sub>0.025</sub> W <sub>0.1</sub> Al and Fe <sub>2</sub> V <sub>0.825</sub> Ta <sub>0.075</sub> W <sub>0.1</sub> Al sample at 40000x magnification. . . . .	46
5.10	Comparing resistivity of 1st and 2nd batch samples before and after annealing. . . . .	47
5.11	Comparing temperature dependent electrical resistivity of samples with the same stoichiometric composition. . . . .	48
5.12	Electrical resistivity comparison between batches and impact of annealing. . . . .	49
5.13	Resistivity of the earlier samples for comparison. . . . .	49
5.14	Seebeck coefficient over temperature comparison. . . . .	50
5.15	Seebeck coefficient comparison between similar and older samples. . . . .	51
5.16	Goldsmid-Sharp VS 2-parabolic band . . . . .	53

5.17 Seebeck coefficient comparison between batches and impact of annealing. . .	54
5.18 Constituents of low-temp thermal conductivity measurement . . . . .	55
5.19 Low-temperature thermal conductivity and lattice thermal conductivity of the 1st batch samples. . . . .	57
5.20 Comparing high-temperature thermal conductivity of the 2nd sample batch.	57
5.21 Power factor comparison between batches and impact of annealing. . . . .	58
5.22 Comparing $zT$ of as cast and annealed . . . . .	59

# Bibliography

- [1] Wikipedia. Thermoelectric effect. [https://en.wikipedia.org/wiki/Thermoelectric\\_effect](https://en.wikipedia.org/wiki/Thermoelectric_effect), accessed 2021-09-22 17:32.
- [2] Saffa B Riffat and Xiaoli Ma. Thermoelectrics: a review of present and potential applications. *Applied thermal engineering*, 23(8):913–935, 2003.
- [3] Asahel Bañobre Aniket Maske N. M. Ravindra, Bhakti Jariwala. *Thermoelectrics: Fundamentals, Materials Selection, Properties, and Performance*. Springer, 2019.
- [4] Peter Wellmann. *Materialien der Elektronik und Energietechnik*. Springer, 2019.
- [5] Chhatrasal Gayner and Kamal K Kar. Recent advances in thermoelectric materials. *Progress in Materials Science*, 83:330–382, 2016.
- [6] Yuxin Sun, Haixu Qin, Chenglong Zhang, Hao Wu, Li Yin, Zihang Liu, Shengwu Guo, Qian Zhang, Wei Cai, Haijun Wu, Fengkai Guo, and Jiehe Sui. Sb<sub>2</sub>Te<sub>3</sub> based alloy with high thermoelectric and mechanical performance for low-temperature energy harvesting. *Nano Energy*, 107:108176, 2023.
- [7] Xiaoying Liu, Dongyang Wang, Haijun Wu, Jinfeng Wang, Yang Zhang, Guangtao Wang, Stephen J. Pennycook, and Li-Dong Zhao. Intrinsically low thermal conductivity in bisbse<sub>3</sub>: A promising thermoelectric material with multiple conduction bands. *Advanced Functional Materials*, 29(3):1806558, 2019.
- [8] Wikipedia. Bismuth. <https://en.wikipedia.org/wiki/Bismuth>, accessed 2021-09-23 16:00.
- [9] Wikipedia. Bismuth telluride. [https://en.wikipedia.org/wiki/Bismuth\\_telluride](https://en.wikipedia.org/wiki/Bismuth_telluride), accessed 2023-05-24-14:57.
- [10] Ting Zhang Jun Jiang. Bi<sub>2</sub>Te<sub>3</sub>-based te nanocomposites. [http://english.nimte.cas.cn/rh/rp/201103/t20110330\\_67000.html](http://english.nimte.cas.cn/rh/rp/201103/t20110330_67000.html), accessed 2023-03-08-15:14.
- [11] Daniel M. Flanagan. Tellurium. <https://pubs.usgs.gov/periodicals/mcs2023/mcs2023-tellurium.pdf>, accessed 2023-06-07-11:38.
- [12] ZH Dughaish. Lead telluride as a thermoelectric material for thermoelectric power generation. *Physica B: Condensed Matter*, 322(1-2):205–223, 2002.
- [13] Pradeep Kumar Sharma, TD Senguttuvan, Vijay Kumar Sharma, and Sujeet Chaudhary. Revisiting the thermoelectric properties of lead telluride. *Materials Today Energy*, 21:100713, 2021.
- [14] Anil Kumar, Paul A Vermeulen, Bart J Kooi, Jiancun Rao, Lambert Van Eijck, Stefan Schwarzmüller, Oliver Oeckler, and Graeme R Blake. Phase transitions of thermoelectric tags-85. *Inorganic chemistry*, 56(24):15091–15100, 2017.
- [15] EM Levin, BA Cook, JL Haringa, SL Bud’Ko, R Venkatasubramanian, and K Schmidt-Rohr. Analysis of ce-and yb-doped tags-85 materials with enhanced thermoelectric figure of merit. *Advanced Functional Materials*, 21(3):441–447, 2011.

- [16] EM Levin, SL Bud'Ko, and Klaus Schmidt-Rohr. Enhancement of thermopower of tags-85 high-performance thermoelectric material by doping with the rare earth dy. *Advanced Functional Materials*, 22(13):2766–2774, 2012.
- [17] Wikipedia. Zintl-phases. <https://de.wikipedia.org/wiki/Zintl-Phasen>, accessed 2023-05-30-14:10.
- [18] Shan Li Zongwei Zhang Xiaofang Li Xinyu Wang Yijie Liu Jiehe Sui Xingjun Liu Feng Cao Zhifeng Ren Ching-Wu Chu Yumei Wang Chen Chen, Wenhua Xue and Qian Zhang. Zintl-phase eu<sub>2</sub>zn<sub>2</sub>sb<sub>2</sub>: A promising thermoelectric material with ultralow thermal conductivity. *PNAS*, 116, 02 2019.
- [19] Hugo Strunz; Ernest Nickel. *Strunz Mineralogical Tables. Ninth Edition*. Schweizerbart Science Publishers, Stuttgart, Germany, 12 2001.
- [20] Zhi-Yuan Liu, Jiang-Long Zhu, Xin Tong, Shuo Niu, and Wen-Yu Zhao. A review of cosb 3-based skutterudite thermoelectric materials. *Journal of Advanced Ceramics*, 9:647–673, 2020.
- [21] Gerda Rogl, Sanyukta Ghosh, Oliver Renk, Kunio Yubuta, Andriy Grytsiv, Erhard Schaffler, Michael Zehetbauer, Ramesh C Mallik, Ernst Bauer, and Peter Rogl. Influence of shear strain on hpt-processed n-type skutterudites yielding  $z_t = 2.1$ . *Journal of Alloys and Compounds*, 855:157409, 2021.
- [22] Wikipedia. Clathrate compound. <https://de.wikipedia.org/wiki/Zintl-Phasen>, accessed 2023-06-07-13:21.
- [23] Jerry L. Atwood. *Inclusion Compounds*. John Wiley & Sons, Ltd, 2000.
- [24] Widya Rika Puspita, Hiroyuki Takeya, Takashi Mochiku, Yoshihisa Ishikawa, Sanghyun Lee, Shuki Torii, Masato Hagihala, and Takashi Kamiyama. Structural study of thermoelectric clathrate ba<sub>8</sub>al<sub>16-x</sub>ga<sub>x</sub>ge<sub>30</sub>. In *2019 2nd International Conference on Applied Engineering (ICAE)*, pages 1–5. IEEE, 2019.
- [25] Max Frenzel, Marina P. Ketris, Thomas Seifert, and Jens Gutzmer. On the current and future availability of gallium. *Resources Policy*, 47:38–50, 2016.
- [26] Lawrence R. Bernstein. Germanium geochemistry and mineralogy. *Geochimica et Cosmochimica Acta*, 49(11):2409–2422, 1985.
- [27] Amy C. Tolcin. Germanium. <https://pubs.usgs.gov/periodicals/mcs2023/mcs2023-germanium.pdf>, accessed 2023-06-07-12:32.
- [28] Ulrich K. Thiele. The current status of catalysis and catalyst development for the industrial process of poly(ethylene terephthalate) polycondensation. *International Journal of Polymeric Materials and Polymeric Biomaterials*, 50(3-4):387–394, 2001.
- [29] Wikipedia. Magnesium silicide. [https://en.wikipedia.org/wiki/Magnesium\\_silicide](https://en.wikipedia.org/wiki/Magnesium_silicide), accessed 2023-06-01-12:17.
- [30] Jiawei Zhang, Lirong Song, and Bo Brummerstedt Iversen. Insights into the design of thermoelectric mg<sub>3</sub>sb<sub>2</sub> and its analogs by combining theory and experiment. *npj Computational Materials*, 5(1):76, Jul 2019.

- [31] Kriti Tyagi, Bhasker Gahtori, Sivaiah Bathula, M. Jayasimhadri, Niraj Kumar Singh, Sakshi Sharma, D. Haranath, A.K. Srivastava, and Ajay Dhar. Enhanced thermoelectric performance of spark plasma sintered copper-deficient nanostructured copper selenide. *Journal of Physics and Chemistry of Solids*, 81:100–105, 2015.
- [32] Yao C Zhan Z Yu W Yu Z Guo C. Singh SC, Li H. Structural and compositional control in copper selenide nanocrystals for light-induced self-repairable electrodes. *Elsevier Sponsored Documents*, 2018.
- [33] Lanling Zhao, Sheik Md Kazi Nazrul Islam, Jun Wang, David.L. Cortie, Xungai Wang, Zhenxiang Cheng, Jiyang Wang, Ning Ye, Shixue Dou, Xun Shi, Lidong Chen, G. Jeffrey Snyder, and Xiaolin Wang. Significant enhancement of figure-of-merit in carbon-reinforced  $\text{Cu}_2\text{Se}$  nanocrystalline solids. *Nano Energy*, 41:164–171, 2017.
- [34] John D Cressler. Silicon-germanium heterojunction bipolar transistor. In *Device and Circuit Cryogenic Operation for Low Temperature Electronics*, pages 69–84. Springer, 2003.
- [35] Hamish Johnston. Silicon-based light emitter is ‘holy grail’ of microelectronics, say researchers. <https://physicsworld.com/a/silicon-based-light-emitter-is-holy-grail-of-microelectronics-say-researchers/>, accessed 2023-06-05-12:10.
- [36] Allon I. Hochbaum, Renkun Chen, Raul Diaz Delgado, Wenjie Liang, Erik C. Garnett, Mark Najarian, Arun Majumdar, and Peidong Yang. Enhanced thermoelectric performance of rough silicon nanowires. *Nature*, 451(7175):163–167, Jan 2008.
- [37] Jian He, Yufei Liu, and Ryoji Funahashi. Oxide thermoelectrics: The challenges, progress, and outlook. *Journal of Materials Research*, 26(15):1762–1772, 2011.
- [38] Hongchao Wang, Wenbin Su, Jian Liu, and Chunlei Wang. Recent development of n-type perovskite thermoelectrics. *Journal of Materiomics*, 2(3):225–236, 2016.
- [39] Jifeng Sun and David J. Singh. Thermoelectric properties of n-type  $\text{SrTiO}_3$ . *APL Materials*, 4(10), 05 2016. 104803.
- [40] Tanja Graf, Claudia Felser, and Stuart SP Parkin. Simple rules for the understanding of heusler compounds. *Progress in solid state chemistry*, 39(1):1–50, 2011.
- [41] Robert J. Quinn and Jan-Willem G. Bos. Advances in half-heusler alloys for thermoelectric power generation. *Mater. Adv.*, 2:6246–6266, 2021.
- [42] Shashwat Anand, Ramya Gurunathan, Thomas Soldi, Leah Borgsmiller, Rachel Orenstein, and G. Jeffrey Snyder. Thermoelectric transport of semiconductor full-heusler  $\text{VFe}_2\text{Al}$ . 8:10174–10184, 2020.
- [43] M. Mikami, Y. Kinemuchi, K. Ozaki, Y. Terazawa, and T. Takeuchi. Thermoelectric properties of tungsten-substituted Heusler  $\text{Fe}_2\text{VAl}$  alloy. *Journal of Applied Physics*, 111(9):093710, 05 2012.
- [44] B Hinterleitner, P Fuchs, J Rehak, F Garmroudi, M Parzer, M Waas, R Svagera, S Steiner, M Kishimoto, R Moser, et al. Stoichiometric and off-stoichiometric full heusler  $\text{Fe}_2\text{V}_{1-x}\text{W}_x\text{Al}$  thermoelectric systems. *Physical Review B*, 102(7):075117, 2020.

- [45] B. Hinterleitner, I. Knapp, M. Poneder, Y. Shi, H. Müller, G. Eguchi, C. Eisenmenger-Sittner, M. Stöger-Pollach, Y. Kakefuda, N. Kawamoto, Q. Guo, T. Baba, T. Mori, S. Ullah, X. . Chen, and E. Bauer. Thermoelectric performance of a metastable thin-film heusler alloy. *Nature*, 576(7785):85–90, 2019. Cited By :188.
- [46] Johannes Wolfgang Rehak. *Thermoelektrizität in off-stöchiometrischen Fe<sub>2</sub>V<sub>1-x</sub>W<sub>x</sub>Al Heusler Systemen*. Wien, 2017.
- [47] Y Nishino. Development of thermoelectric materials based on fe<sub>2</sub>val heusler compound for energy harvesting applications. In *IOP Conference Series: Materials Science and Engineering*, volume 18, page 142001, 2011.
- [48] Fabian Garmroudi, Michael Parzer, Alexander Riss, Andrei V Ruban, Sergii Khmelevskiy, Michele Reticioli, Matthias Knopf, Herwig Michor, Andrej Pustogow, Takao Mori, et al. Anderson transition in stoichiometric fe<sub>2</sub>val: high thermoelectric performance from impurity bands. *Nature Communications*, 13(1):3599, 2022.
- [49] Kodai Fukuta, Koichi Tsuchiya, Hidetoshi Miyazaki, and Yoichi Nishino. Improving thermoelectric performance of fe<sub>2</sub>val-based heusler compounds via high-pressure torsion. *Applied Physics A*, 128(3):184, 2022.
- [50] Alex Zevalkink, David M Smiadak, Jeff L Blackburn, Andrew J Ferguson, Michael L Chabinyk, Olivier Delaire, Jian Wang, Kirill Kovnir, Joshua Martin, Laura T Schelhas, Taylor D Sparks, Stephen D Kang, Maxwell T Dylla, G. Jeffrey Snyder, Brenden R Ortiz, and Eric S Toberer. A practical field guide to thermoelectrics: Fundamentals, synthesis, and characterization. *Applied physics reviews*, 5(2):21303, 2018.
- [51] Burkard Hillebrands Hartmut Hillmer Harald Ibach Rainer Kassing Hilbert v. Löhneysen Peter Luger Josef Salbeck Udo Scherz Werner Schilling-Ludwig K. Thomas Stefan Bügel, Margret Giesen. Bergmann, schäfer, lehrbuch der experimentalphysik—band 6: Festkörper, 2005.
- [52] Rudolf Gross, Achim Marx, Dietrich Einzel, and Stephan Geprägs. Festkörperphysik. In *Festkörperphysik*. de Gruyter, 2018.
- [53] S. Bühler-Paschen, H. Michor, and M. Reissner. *Festkörperphysik I*. Wien, 2016.
- [54] Harald Ibach and Hans Lüth. *Festkörperphysik: Einführung in die Grundlagen*. Springer-Lehrbuch. Springer Berlin / Heidelberg, Berlin/Heidelberg, 7 edition, 2009.
- [55] Franz Schwabl. *Statistische Mechanik*. Springer-Lehrbuch. Springer-Verlag Berlin Heidelberg, Berlin, Heidelberg, dritte, aktualisierte auflage edition, 2006.
- [56] what-when how. Electrons in a crystal (fundamentals of electron theory) part 2. <https://what-when-how.com/electronic-properties-of-materials/electrons-in-a-crystal-fundamentals-of-electron-theory-part-2/>, accessed 2023-02-16 16:56.
- [57] Fabian Garmroudi. *Microstructure and thermoelectric properties of full-Heusler compounds based on Fe<sub>2</sub>VAl co-doped with Ta and Si*. Wien, 2020.
- [58] Siegfried Hunklinger. *Festkörperphysik*. Oldenbourg, München Wien, 2007.
- [59] Monika Budnowski. *Search for new Zintl phases for thermoelectricity*. Wien, 2017.

- [60] Wikipedia. Debye model. [https://en.wikipedia.org/wiki/Debye\\_model](https://en.wikipedia.org/wiki/Debye_model), accessed 2023-10-14 13:39.
- [61] Rolf Pelster, Ingo Hüttel, and Reinhard Pieper. Thermospannungen-viel genutzt und fast immer falsch erklärt. *PhyDid A-Physik und Didaktik in Schule und Hochschule*, 1(4):10–22, 2005.
- [62] B Hinterleitner, F Garmroudi, N Reumann, T Mori, E Bauer, and R Podlucky. The electronic pseudo band gap states and electronic transport of the full-heusler compound fe 2 val. *Journal of Materials Chemistry C*, 9(6):2073–2085, 2021.
- [63] Wikipedia. Seebeck coefficient. [https://en.wikipedia.org/wiki/Seebeck\\_coefficient](https://en.wikipedia.org/wiki/Seebeck_coefficient), accessed 2023-10-14 19:22.
- [64] E. M. Levin. Charge carrier effective mass and concentration derived from combination of seebeck coefficient and  $^{125}\text{Te}$  nmr measurements in complex tellurides. *Phys. Rev. B*, 93:245202, Jun 2016.
- [65] Nick Mann Theodore Gray and Max Whitby. Periodic table of elemets. <https://periodictable.com/>, accessed 2022-06-28 17:00.
- [66] what-when how. Electrons in a crystal (fundamentals of electron theory) part 2. [https://www.researchgate.net/figure/Conditions-for-diffraction-and-derivation-of-Braggs-law\\_fig1\\_36368439](https://www.researchgate.net/figure/Conditions-for-diffraction-and-derivation-of-Braggs-law_fig1_36368439), accessed 2022-07-01 14:33.
- [67] ULVAC. Ulvac zem-3. <https://ulvac.eu/products/components/thermal-analysis/zem-3/>, accessed 2022-07-05 16:30.
- [68] Wikipedia. Laser flash analysis. [https://en.wikipedia.org/wiki/Laser\\_flash\\_analysis](https://en.wikipedia.org/wiki/Laser_flash_analysis), accessed 2022-07-18-15:51.
- [69] technical cell@bose. Scanning electron microscope (quanta 250 feg). [https://www.bose.res.in/facilities/Technical\\_Cell/sem.html](https://www.bose.res.in/facilities/Technical_Cell/sem.html), accessed 2023-03-08-14:44.
- [70] TU Wien. Ustem - the electron microscopy facility of tu wien. <https://www.tuwien.at/en/research/facilities/ustem>, accessed 2023-03-08-14:53.
- [71] Wikipedia. Scanning electron microscope. [https://en.wikipedia.org/wiki/Scanning\\_electron\\_microscope#/media/File:Electron-matter\\_interaction\\_volume\\_and\\_various\\_types\\_of\\_signal\\_generated\\_-\\_v2.svg](https://en.wikipedia.org/wiki/Scanning_electron_microscope#/media/File:Electron-matter_interaction_volume_and_various_types_of_signal_generated_-_v2.svg), accessed 2023-03-08-15:01.
- [72] Fabian Garmroudi, Alexander Riss, Michael Parzer, N. Reumann, H. Müller, Ernst Bauer, Sergii Khmelevskyi, Raimund Podlucky, Takao Mori, K. Tobita, Yukari Katsura, and Kaoru Kimura. Boosting the thermoelectric performance of fe2val-type heusler compounds by band engineering. *Physical Review B*, 103, 02 2021.